THE PHYSICOCHEMICAL PROPERTIES OF CARBON NANOTUBE-TITANIA NANOCOMPOSITE FOR LIGHT HARVESTING

By

Edwin Tonderai Mombeshora

Submitted in fulfilment of the academic requirements for the degree of Master of Science in the School of Chemistry and Physics, University of KwaZulu-Natal, Durban.

Supervisor: Dr V.O. Nyamori

Co-supervisor: Dr P.G. Ndungu

May 2014

Abstract

Nanocomposites for dye-sensitised solar cells (DSSCs) were synthesised from ultrasonic acid-treated multiwalled carbon nanotubes (MWCNTs) and titania precursors by means of sol-gel and chemical vapour deposition (CVD) processes. The wt.% of MWCNTs in nanocomposites were varied from 2 to 98. Physicochemical properties investigation forms the core of the study. Hence, nanocomposites were thoroughly characterised by means of thermogravimetric analysis (TGA), scanning electron microscopy (SEM), transmission electron microscopy (TEM), high resolution transmission electron microscopy (HRTEM), electron dispersive X-ray spectroscopy (EDX), Raman spectroscopy, Fourier transformation infra-red spectroscopy (FTIR), textural characteristics, inductively coupled plasma optical emission spectroscopy (ICP-OES), photoluminescence (PL) and powder X-ray diffraction (XRD) techniques. Nanocomposites were used as photoanode in assembled DSSCs. The gel electrolyte was polyvinyl acetate (PVAc) doped with LiI. Aluminium was the photocathode. The DSSCs were tested for their performance by illuminating them in a solar simulator device.

Characteristic hollow MWCNTs morphology with titania particulates was obtained. Both synthetic methods coated small diameter MWCNTs well. EDX spectra showed titania and carbon peaks. The ICP-OES data correlated with TGA in that residual wt.% values were within the expected ranges. Defects from acid treatment lowered thermal stability of pristine MWCNTs from 640 °C to 625 °C. Ti-O-C bond (ca. 1110 cm^{-1}) and anatase form of titania (ca. 669, 577 and 411 cm^{-1}) were observed. Raman spectroscopy showed E_g, A_{1g} + $B_{1g(2)}$ and $B_{1g(2)}$ modes of anatase titania at ca. 630, 514 and 396 cm^{-1} respectively. I_D/I_G trends indicate that titania reduced defects in MWCNTs. MWCNTs in nanocomposites from the CVD method had fewer defects, highly thermally stable and more uniformly coated, more crystalline, more porous and had smaller surface areas than sol-gel prepared nanocomposites.

Nanocomposites had lower e^-/h^+ recombination and band gap energy than titania. The optimum MWCNTs wt.% in DSSCs was 15% and CVD nanocomposites were 900% more efficient. From this work, ideal nanocomposites physicochemical properties for DSSCs

application include uniform morphology, a defect-free nature, crystallinity, large pore size and volume, and existence of chemical bonds between components. Other factors rather than band gap engineering such as absorption properties of DSSC components also affect DSSC capabilities. Also, the high e^- conductivity nature of MWCNTs interferes with e^- transport from the nanocomposites to the counter electrode at high MWCNTs wt.%.

Preface

The experimental work presented in this dissertation was carried out in the School of Chemistry and Physics, University of KwaZulu-Natal, Durban, from August 2012 to November 2013, under the supervision of Dr V.O. Nyamori and Dr P.G. Ndungu.

The studies represent original work by author and have not otherwise been submitted in any form for any degree or diploma to any tertiary institution. Where use has been made of the work of others, it is duly acknowledged in the text.

Declaration-Conference presentations based on the current work

Oral presentations

1. Edwin T. Mombeshora, Patrick G. Ndungu and Vincent O. Nyamori, "The physicochemical properties of carbon nanotube-titania nanocomposites materials for light harvesting", proposal presentation at the India, Brazil and South Africa (IBSA) workshop on materials for energy, Thaba Ya Batswana, South Africa, 14 October to 17 October 2012.
2. Edwin T. Mombeshora, Patrick G. Ndungu and Vincent O. Nyamori, "The physicochemical properties of carbon nanotube-titania nanocomposite materials for light harvesting", India, Brazil and South Africa (IBSA) workshop on nanomaterials, Saint George's Hotel and Convention centre, South Africa, 29 May to 31 May 2013.
3. Edwin T. Mombeshora, Patrick G. Ndungu and Vincent O. Nyamori, "Light harvesting nanomaterials", Howard campus, University of KwaZulu-Natal, South Africa, 1 November 2013.
4. Edwin T. Mombeshora, Patrick G. Ndungu and Vincent O. Nyamori, "Nanocomposites for light harvesting and Energy", Universidade Federal do Paraná Curitiba, Brazil, 27 November to 29 November 2013.

Poster presentations

1. Edwin T. Mombeshora, Patrick G. Ndungu and Vincent O. Nyamori, "The physicochemical properties of carbon nanotube-titania nanocomposite materials for light harvesting", at the 16th South African Chemical Institute Inorganic conference, South Sun Elangeni, University of KwaZulu-Natal, 30 June to 4 July 2013.
2. Edwin T. Mombeshora, Godfrey K. Keru, Patrick G. Ndungu and Vincent O. Nyamori, "Solar energy harnessing materials", at the Eskom exhibition, University of KwaZulu-Natal, 29 August 2013.

Publications based on the current work

1. Edwin T. Mombeshora, Reuben Simoyi, Vincent O. Nyamori and Patrick G. Ndungu, "Synthesis of multiwalled carbon nanotubes-titania nanocomposites: A comparison between sol-gel and chemical vapour deposition methods" (manuscript in preparation to be submitted in the future work).

Plagiarism

I, Edwin Tonderai Mombeshora declare that:

1. The research reported in this thesis, except where otherwise indicated is my original research work.
2. This work has not been submitted in any form to another university or institution.
3. This thesis does not contain other persons' data, pictures, graphs or other information, unless specifically acknowledged as being sourced from other persons.
4. This thesis does not contain other persons' writing, unless specifically acknowledged as being sourced from other researchers. Where other written sources have been quoted, then:
    a. Their words have been re-written but the general information attributed to them has been referenced.
    b. Where their exact words have been used, then their writing has been placed in italics inside quotation marks and referenced.
5. This thesis does not contain text, graphics or tables copied and pasted from the internet, unless specifically acknowledgements and the source being detailed in the thesis and in the references sections.

.....

E.T. Mombeshora

Table of Contents

List of Tables

List of Figures

Chapter Two

Chapter Three

Chapter Four

Acknowledgements

I would like to express my sincere gratitude and appreciate special contributions from;

- My supervisor, Dr V.O. Nyamori for his good supervision skills, advice, guidance and motivation throughout the course of this work.
- My co-supervisor, Dr P.G. Ndungu for his overwhelming ideas, guidance and assistance throughout the studies.
- Professor R. Simoyi for guidance, motivation and ideas.
- Professor G. Mola for advice and use of solar cell facilities.
- Professor B. Martincigh and Dr N. Mahdjoub for proofreading and guidance.
- Mr P. Christopher and Mr V. Bharuth for the assistance in the electron microscopy unit.
- Mr N. Bromhead and Mrs A. Pillay for assistance in the instrumental laboratory.
- My lab mates and friends, G. Keru, S. Zulu, E. Oseghe, K. Mugadza, N. Ramoraswi, B. Gumbi, L. Ombaka, E. Njogu, B. July, C. Ntokozo, T. Chigumbura and M. Pillay for support and encouragement.
- My family, Dr S. Mombeshora, Mrs F. Mombeshora (Nee Musonza), Mr T. Mombeshora and Mr E. Mombeshora for motivation and support throughout my project.
- India, Brazil and South Africa Nanotechnology Initiative for financial support.
- The School of Chemistry and Physics for infrastructure and facilities.

List of Abbreviations and Symbols

Full name	Abbreviation/symbol
Air mass	AM
Barret-Joyner-Halenda	BJH
Brunauer-Emmett-Teller	BET
Cadmium telluride	CdTe
Carbon	C
Carbon nanotubes(s)	CNT(s)
Charge-coupled device	CCD
Chemical vapour deposition	CVD
Cobalt	Co
Concentrated solar power	CSP
Conduction band	CB
Conversion efficiency	n
Copper-indium gallium selenide	CIGS
Degrees Celsius	°C
Double-walled carbon nanotube(s)	DWCNT(s)
Dye-sensitised solar cell(s)	DSSC(s)
Electromotive force	emf
Electron current conversion	ECE
Electron conversion efficiency	ECE
Electric field	E-field
Electrical impedance spectroscopy	EIS
Electron volt	eV

External quantum efficiency	EQE
Fermi level	E_f
Field emission electron microscopy	FE-SEM
Fill factor	FF
Fluorine	F
Fourier transform infra-red spectroscopy	FTIR
Giga	G
GigaPascal	GPa
Highest occupied molecular orbitals	HOMO
Hour	hr
Incident photo conversion efficiency	IPCE
Incident photon-to-current conversion efficiency	ICPE
India Brazil South Africa	IBSA
Indium tin oxide	ITO
Inductively coupled plasma-mass spectroscopy	ICP-MS
Inductively coupled plasma-optical emission spectroscopy	ICP-OES
International centre for diffraction data	ICDD
Iron	Fe
Kelvin	K
Kilovolt	Kv
Lowest occupied molecular orbitals	HOMO
Maximum current	I_{max}
Maximum voltage	V_{max}
Micro	μ
Millennium developmental goals	MDGs

Milliamperes	mA
Millibar	mbar
Millimetre	mm
Milliwatts	mW
Minute	min
Multiwalled carbon nanotube(s)	MWCNT(s)
Nano	10^{-9}
Nanometre	nm
Near infra-red	NIR
Nickel	Ni
Nitrogen	N
Ohms	Ω
Open circuit voltage	V_{OC}
Per centimetre	cm^{-1}
Photovoltaic	PV
poly(3, 4-ethylenedioxythiophene) poly(styrenesulfonate)	PEDOT-PSS
Polyvinyl acetate	PVAc
Power input	P_{IN}
Quantum dot(s)	QD(s)
Scanning electron microscopy	SEM
Second	s
Series resistance	R_s
Shaped carbon nanomaterials	SCNM
Shunt resistance	R_{SH}
Short circuit current density	J_{SC}

Single-walled carbon nanotube(s)	SWCNT(s)
1 sun	100 mW cm^{-2}
Sulfer-oxygen	S-O
TeraPascal	TPa
TeraWatt	TW
2, 2', 7, 7'-Tetrakis(diphenylamino)-9, 9'-spirobifluorene	Spiro-OMe TAD
Thermogravimetric analysis	TGA
Thermogravimetric curve	TG curve
Titanium(iv)isopropoxide	TIP
Titanium methoxide	TM
Titanium n-butoxide	TNB
Titanium propoxide	TPP
Transmission electron microscopy	TEM
Two-dimension	2D
Ultraviolet	UV
Valence band	VB
Velocity	v
Volts	V
Weight percentage	wt.%
Wavelength	λ
X-ray photon spectroscopy	XPS

Chapter One

Introduction

This chapter presents background information on energy, the problem statement, motivation and the research hypothesis, aim and objectives, questions, approach and scope, and an overview of the thesis.

1.1 Background

Energy is an essential requirement of a society which keeps life going and easy. It can be seen that energy demands are growing in every community and current energy sources are failing to cope. The global village is compelled to seek ways to solve this problem. Unfortunately, not all ways devised by mankind to date are feasible and environmentally friendly. This work presents the synthesis and characterisation of nanocomposites as a potential way of scaling up the current low electricity energy generation from sunlight.

1.2 Problem statement

Mankind's dependency on energy has not only reached alarming levels but also high consumption levels which are not being matched by current energy generation technologies (discussed in **Chapter Two**). Fossil fuels are currently the biggest source of energy globally.[1] Burning of some of these fuels produce CO, CO_2 and SO_x among other gases which have negative consequences. For example, SO_2 may be converted to H_2SO_4 and eventually to acid rain in a series of steps. Acid rain is harmful to the environment in so many ways such as soil leaching, acidification of aquatic systems, corrosion of buildings, deforestation and eutrophication. Mining of coal and crude oil is resulting in various negative effects such as loss of usable land, formation of sink holes, reduction of biodiversity and reduction in air quality. Also global climate change is increasing at an alarming rate due to greenhouse gas emissions such as CO_2.[1] Developing countries especially in Africa are disadvantaged by the high cost of fuel on the market and this retards development in these nations.

Furthermore, geo-political factors in certain parts of the world control oil pricing and availability of oil on the market.[2,3] In light of this it is imperative that alternative sources of energy are sought, not only to compete with, but also, to mitigate the negative impacts of mining and use of fossil fuels. The concern has been to develop greener energy resources such as light-harvesting devices.

1.3 Motivation

The world will be in a deep energy shortfall unless new efficient technologies and materials are developed for energy conversions into usable forms accessible to mankind. Sunlight seems to be a reliable alternative candidate over other sources of energy for a number of reasons. For example, solar energy is renewable, has no gas emissions or health-related hazards associated with its harvesting and use. It is reliable because sunlight shines all year round in most parts of Africa and promotes independence of nations. Although more research is required to reduce the high initial installation costs associated with device production, solar energy technologies provide tangible social and green economic benefits for communities, nations and the global village. Solar energy is currently being harvested by use of various solar panels such as cadmium telluride (CdTe), copper-indium-gallium selenide (CIGS), amorphous silicon on steel, silicon wafers, dye-sensitised solar cells (DSSCs) and organic solar cells. The solar panels that currently dominate the market are silicon-based and this contributes to high initial costs since silicon is an expensive element partly due to its high demand in the field of electronics. Silicon wafers require high quality materials, sophisticated technology and longer time to fabricate.[4] Silicon-wafer based solar panels need very competitive alternatives. One of the promising candidates as an alternative to silicon-based solar cells are DSSCs which can function at low light intensities, are simple to fabricate, are environmentally friendly and can function at any angle of orientation.[5] A DSSC is made up of a photoanode material stained with a dye which absorbs light from the sun, a photocathode material and a redox couple which acts as an electrolyte in the regeneration of the ground state dye (see **Chapter Two**). DSSCs require efficient working photoanode materials. Nanomaterial optical properties can be tailored to enhance their light-harvesting capability.[6] Titania as a photoanode nanomaterial in DSSCs containing

ruthenium based dyes is well reported in literature.[7-9] In recent years interest has shifted towards metal-free dyes from the well documented ruthenium-based DSSCs. Furthermore, some natural dyes have been intensively investigated for their potential and application as sensitizers.[5,10] The other concern has been the high band gap energy of anatase titania[11] which has a potential to absorb at most 5% of incident solar radiation.[12,13] This shows a gap for further studies in understanding and engineering ways of improving efficiency by using readily available materials and band gap reduction can be achieved by doping.[14]

Carbon nanotubes (CNTs) can play a role in altering the band gap and improving the efficiency of titania in DSSCs. Multiwalled carbon nanotubes (MWCNTs) were the particular choice in this research because unlike single-walled carbon nanotubes (SWCNTs) and double-walled carbon nanotubes (DWCNTs), they are conducting materials which are cheap, easy to synthesise and easy to scale-up in production. Although some authors argue that MWCNTs will compete for light absorption with titania,[15] their work has been mostly on low wt.% ratios of MWCNTs. A literature survey conducted on titania-MWCNT nanocomposites indicates that these nanocomposites have excellent photo-capability. Most applications that utilize these nanocomposites have been reported on photo-catalytic reactions for water purification.[13,16,17] A limited number are on DSSCs. The seemingly few reports on DSSCs acknowledges various advantages of such nanocomposites, for example, Li *et al.*[18] reported that an increase in the MWCNT content leads to an increase in conductivity of titania.[16]

Solar conversion efficiency may be enhanced by synthesising nanocomposites and tailoring the physical dimensions, composition and morphology of MWCNT-TiO_2. An investigation on the behaviour of such nanocomposites at higher wt.% loading, optimisation of the MWCNT wt.% in such nanocomposites and comparing nanocomposites obtained by different synthetic methods are potential and promising frontiers in solar energy harnessing techniques. The drive is to develop an architecture which allows a simultaneous efficient excitonic dissociation and electron transport.

1.4 Research questions

- Which is a better method for synthesising MWCNT-titania nanocomposites, CVD or sol-gel technique?
- Does the synthesis method and wt.% ratios in the MWCNT-titania nanocomposites influence the physicochemical properties and light-harvesting capabilities?
- What physicochemical properties are ideal for light harnessing?
- What is the optimum wt.% ratio of MWCNTs for light harnessing?

1.5 Research aim and objectives

The aim was to synthesise efficient solar-harvesting materials of MWCNTs and TiO_2.

The objectives of the project were to:

- Synthesise MWCNT-titania nanocomposites using chemical vapour deposition (CVD) and sol-gel methods.
- Synthesise anatase titania as the only phase in nanocomposites.
- Investigate the physical and chemical properties of the synthesised MWCNT-titania nanocomposites.
- Design an efficient photovoltaic solar cell containing the MWCNT-titania nanocomposites as an anode material.
- Synthesising an efficient redox electrolyte system for DSSCs designed.
- Investigate the photovoltaic (PV) efficiency at different wt.% ratios of MWCNTs in the MWCNT-titania nanocomposites constituents.
- Compare efficiency of CVD and sol-gel synthesized nanocomposites in solar cells.

1.6 Research hypotheses

- Since anatase titania absorbs in the UV region of the electromagnetic spectrum due to its large band gap then reducing band gap by engineering a mismatch of the dye conduction band (CB) and that of titania by the use of a dye that absorbs in the visible region is expected to extend light absorption into the visible region and thereby increase light-harvesting.

- If the work function of MWCNTs is more negative than that of anatase titania then MWCNTs will readily conducts the electron received by the titania CB from the excited dye and thereby reduce the electron-hole (e^-/h^+) recombination in titania.
- If the morphology of the nanocomposite plays a role in device performance then the MWCNT:titania ratio and the method of synthesis of the nanocomposites should influence the results obtained in light-harvesting.

1.7 Research approach

Commercial MWCNTs were acid-treated in an ultrasonic water bath in a mixture of acids to remove the residual iron catalyst and to add oxygen-containing functional groups onto the tubes. These were combined with titania to form the nanocomposites by means of two methods, namely, sol-gel and chemical vapour deposition (CVD) methods.

Titania exist in three phases, i.e. rutile, brookite and anatase. Of three phases, the anatase form of titania has been reported to perform better in light-harvesting applications.[19] The rutile phase of titania is more thermodynamically stable than anatase. In this work the target titania phase was anatase. Therefore, the heating programme in the CVD method was chosen to be below 500 °C to avoid the anatase phase of titania transforming to rutile. A further consideration taken into account was that thermal decomposition of the MWCNTs occurs above 400 °C. Therefore, calcining of nanocomposites to decompose organic components from the titania precursor was carried out at temperatures below 400 °C. A number of nanocomposites were prepared with different loadings of titania onto MWCNTs (0-50 wt.%) and MWCNTs onto titania (0-50 wt.%). All the characterisation techniques were thoroughly performed on each nanocomposite.

After synthesising the nanocomposites, scanning electron microscopy (SEM) analysis was performed to check the characteristic morphology of the titania and MWCNTs in the nanocomposites. After confirming the morphology, energy dispersive X-ray (EDX) analysis was used as a qualitative technique to confirm the components of the nanocomposites as Ti and C. Transmission electron microscopy (TEM) was used to determine the dimensions of the MWCNTs in the MWCNT-titania nanocomposites, topography and morphology of the MWCNT-titania nanocomposites. A closer view of the morphology was carried out by using

high resolution transmission electron microscopy (HRTEM) and also to determine the lattice fringes. After confirming the presence of titania on the MWCNT walls, an investigation of whether the type of link between the former and the latter was chemical (covalent bonding) or physical (no chemical bond) was important. This was done by means of FTIR spectroscopy. A chemical link implies stronger intimacy between the MWCNTs and titania, which is favourable in electron transport. At this stage it was necessary to determine whether the weight percentage was within the expected ranges. Inductively coupled plasma-optical emission spectroscopy (ICP-OES) was used to determine the concentration of titanium in an accurately weighed sample of nanocomposites subsequently digested with a mixture of nitric acid and sulfuric acid. Thermogravimetric analysis was used to further determine the composition and thermal stability of the MWCNTs in the MWCNT-titania nanocomposites. The crystal line quality of the MWCNTs in the MWCNT-titania nanocomposites was investigated at different weight percentage loadings by means of the Raman spectroscopy. This technique was also used to check if the target titania phase, anatase, was the only phase synthesised from both methods. The crystalline quality for the nanocomposites was also determined by Powder X-ray Diffraction (XRD). XRD was also used to identify the lattice types and to confirm the observations from Raman spectroscopy in terms of the phase of titania in the MWCNT-titania nanocomposites. More crystalline nanocomposites would imply a reduced number of boundaries and hence a reduction in the possible number of recombination centres. Textural characteristics such as surface area and pore volume are vital aspects of our light-harvesting goals. They influence the dye adsorption capabilities of a MWCNT-titania nanocomposite. The isotherms were fitted into the Brunauer-Emmett-Teller (BET) equation.[21]

Furthermore, an investigation of the electron-hole (e^-/h^+) recombination dynamics of the titania-MWCNT nanocomposites with composition were done by means of photoluminescence (PL). Electron-hole recombination dynamics were matched with different band gap energies arising from the different MWCNTs loadings. Diffuse reflectance spectroscopy was employed to estimate the band gap energies.

The next step was fabrication of solar devices and application of MWCNT-titania nanocomposites as photo-anode nanomaterials in DSSCs. The iodine concentration was

optimised in terms of conductivity prior to synthesis of a gel-state electrolyte.[20] However, an electrolyte was not all that was required to make a working device at this stage. A dye was required to capture the solar irradiance but not all dyes are suitable. Consequently, ultraviolet-visible (UV-Vis) spectroscopy was used to check if eosin B dye chosen in this work absorbs light in the visible region of the spectrum. Thereafter, the MWCNT-titania nanocomposites were dispersed in ethanol in an ultrasonic water bath prior to fabrication of a photoanode. The doctor blade method was used to deposit the nanocomposite material onto indium tin oxide (ITO) coated glass.[12] Sintering and dye staining followed. A solar device was subsequently constructed in a sandwich fashion by using aluminium-coated glass as a counter electrode (photocathode). A gel-state electrolyte was inserted between the photo-electrodes. A four quadrant Keithley source measure unit equipped with a solar simulator was used for photo-electrochemical measurements.

1.8 Research scope

This section describes the limitations and delimitations involved in this work.

1.8.1 Limitations

- The two synthetic methods of nanocomposite preparation used different precursors of titania. This was necessary because the CVD method, which involved a solid, was done under vacuum conditions and hence may not have been suitable with a liquid precursor. If the nature of the precursors affects the morphology and other physicochemical properties, then this is a variable.
- The light-harvesting experiments were done in an uncontrolled environment since a glove box was not available. However, the MWCNT-titania nanocomposites were compared with laboratory synthesised titania under the same conditions and at the same time. The main objectives were to investigate the effects of method of synthesis and loadings relative to titania. Furthermore, the environmental factors not monitored in this work actually reduce performance and that means the devices have potential to perform better in a controlled environment.

- The e^-/h^+ recombination dynamics at the interfaces of the solar cell devices were not measured by the conventional impedance spectroscopy due to unavailability of the instrument.

1.8.2 Delimitations

- A surfactant was not used to disperse the components of the nanocomposites prior to synthesis. Acid-treating MWCNTs reduces agglomeration by introducing hydrophilic groups on the MWCNTs. Also proper dispersion of MWCNTs and introduction of the titanium precursor with the MWCNTs/ethanol mixture in an ultrasonic water bath produces comparable titania coatings.
- Anatase was the target titania phase because it is reported to have the best electron conductivity capabilities compared with rutile and brookite.
- The synthesis temperature in the CVD method and the sol-gel method calcining temperature was 400 °C at most to avoid the formation of the rutile isomorph and the loss of MWCNTs *via* thermal decomposition.
- A binder was not used in depositing the nanocomposites onto ITO coated glass in order to eliminate any possible effects of the binder in electron transport.
- Light-harvesting experiments for nanocomposites with MWCNTs wt.% ratios above 50 were not presented because the devices did not work.

1.9 Structure of thesis

Chapter One

In this chapter the motivation of the study, and methodology, and the aim and objectives of the research are given. The problem statement, research scope and the thesis structure are also stated in this chapter.

Chapter Two

A background to MWCNTs, titania and composites of MWCNT-titania is given. A brief review of parameters involved in DSSCs is also presented. Some findings from similar work carried out elsewhere are also presented.

Chapter Three

This chapter focuses on the synthesis MWCNT-titania nanocomposites and provides details on the reagents, instrumentation and experimental procedures.

Chapter Four

The characterisation of the nanocomposites and a discussion of the results obtained is presented in this chapter. This constitutes the core of the study. The physicochemical properties of the nanocomposites are thoroughly discussed.

Chapter Five

This chapter presents the application of the multiwalled carbon nanotube-titania nanocomposites in DSSCs, and links the properties investigated in Chapter Three with the performance in DSSCs.

Chapter Six

Finally, a summary of the findings and overall conclusion of the research are given as well as suggestions for future endeavours.

References

1. M. J. Rybak-Smith, R. B. Sim, *Advanced Drug Delivery Reviews,* 2011, **63**, 1031-1041.
2. H. Khatib, *Energy Policy*, 2014, **64**,71-74.
3. B. Fattouh, L. El-Katiri, *Energy Strategy Reviews,* 2013, **2**, 108-115.
4. C. Becker, D. Amkreutz, T. Sontheimer, V. Preidel, D. Lockau, J. Haschke, L. Jogschies, C. Klimm, J. J. Merkel, P. Plocica, S. Steffens, B. Rech, *Solar Energy Materials and Solar Cells,* 2013, **119**, 112-123.
5. H. Hug, M. Bader, P. Mair, T. Glatzel, *Applied Energy,* 2014, **115**, 216-225.
6. J. D. Qiu, M. Q. Deng, R. P. Liang, M. Xiong, *Sensors and Actuators B: Chemical,* 2008, **135**, 181-187.
7. S. R. Jang, M. J. Choi, R. Vittal, K. J. Kim, *Solar Energy Materials and Solar Cells,* 2007, **91**, 1209-1214.
8. S. Yang, H. Kou, S. Song, H. Wang, W. Fu, *Colloids and Surfaces A: Physicochemical and Engineering Aspects,* 2009, **340**, 182-186.
9. G. Wu, F. Kong, J. Li, W. Chen, X. Fang, C. Zhang, Q. Chen, X. Zhang, S. Dai, *Dyes and Pigments,* 2013, **99**, 653-660.
10. M. Fitra, I. Daut, M. Irwanto, N. Gomesh, Y. M. Irwan, *Energy Procedia,* 2013, **36**, 333-340.
11. N. Selvakumar, H. C. Barshilia, *Solar Energy Materials and Solar Cells,* 2012, **98**, 1-23.
12. I. K. Ding, J. Melas-Kyriazi, N. L. Cevey-Ha, K. G. Chittibabu, S. M. Zakeeruddin, M. Grätzel, M. D. McGehee, *Organic Electronics,* 2010, **11**, 1217-1222.
13. N. Aman, P. K. Satapathy, T. Mishra, M. Mahato, N. N. Das, *Materials Research Bulletin,* 2012, **47**, 179-183.
14. G. An, W. Ma, Z. Sun, Z. Liu, B. Han, S. Miao, Z. Miao, K. Ding, *Carbon,* 2007, **45**, 1795-1801.

15. A. de Morais, L. M. D. Loiola, J. E. Benedetti, A. S. Gonçalves, C. A. O. Avellaneda, J. H. Clerici, M. A. Cotta, A. F. Nogueira, *Journal of Photochemistry and Photobiology A: Chemistry,* 2013, **251**, 78-84.

16. Y. Cong, X. Li, Y. Qin, Z. Dong, G. Yuan, Z. Cui, X. Lai, *Applied Catalysis B: Environmental,* 2011, **107**, 128-134.

17. H. Bing-Shun , C. Feng-Yim, M. Y. Wey, *International Journal of Hydrogen Energy,* 2010, **12**, 2503-2510.

18. W. J. Lin, C. T. Hsu, Y. C. Tsai, *Journal of Colloid and Interface Science,* 2011, **358**, 562-566.

19. Y. Zhao, K. Jiang, W. Xu, D. Zhu, *Tetrahedron,* 2012, **68**, 9113-9118.

20. P. Bellaby, *Energy Policy,* 2010, **38**, 2624-2630.

21. K. S. W. Sing, D. H. Everett, R. A. W. Haul, L. Moscou, R. A. Pierotti, J. Rouquerol, T. Siemieniewska, *Pure and Applied Chemistry*, 1985, **57**, 603-619.

Chapter Two

Literature Review

This chapter reviews energy, nanotechnology, carbon nanotubes and titania as nanomaterials for light-harvesting. All the listed aspects are reviewed in the context of high efficiency electrical energy generation which will in turn reduce infrastructure investments, eliminate high energy bills, and improve health and consumer welfare.[1]

2.1 Introduction

Life on planet earth is dependent on energy. Plants require energy for photosynthesis. Humankind uses energy captured by chlorophyll indirectly when they consume food. However, part of the worries of humankind has always included energy to use on other things other than the human body. Modern life, as we know it, requires energy for several reasons such as cooking, entertainment, transport, lighting, industries and communication. Energy security at affordable prices is a core aspect.[1] Historic evidence found in Kenya (at Koobi Fora), suggest that the importance of energy was realized at an early stage with the discovery of fire by *Homo erectus* around 400 000 years ago.[2] Today the world faces a potential energy crisis, so there is need for developing ways to enhance energy transformations to usable forms.

2.2 Society and modern energy resources

Relevant environmental factors for a sustainable community are food, water, energy and natural resources. Energy is the most important factor.[3] The discovery of fire by primitive humankind impacted modern developments such as dietary variety and hygienic cooking practices.[2] Supply of reliable, clean and sustainable energy is the most important global scientific and technical challenge of the 21st century.[4] In an attempt to achieve health and poverty related Millennium Developmental Goals (MDGs) it is difficult to avoid the subject of energy in a society. This section discusses some extreme examples of the needs of

various developing countries within Africa, as well as a way of grasping a representative view of some African communities with regard to modern energy resources.

2.2.1 Energy policies

Developing countries consume 40-50% of the total amount of commercial energy as industrial energy. According to the East Africa Community energy policy, more than 81% of the East African population, as for 2009, were living with no access to modern energy services. In the two extreme developed scenarios of Africa, biomass provides 90% of the total energy consumption of the 18.3 million Mozambique population whereas in South Africa 34% use paraffin and wood.[2] Traditional biomass burnt in open three-legged stoves is insufficient and associated with indoor smoke related hazards. Less than 30% of the East African population uses liquefied petroleum gas (LPG). This is an indication that an alarming proportion of the African population may not be participating economically and socially in improving their living standards. Although the basis of this information is on a part of Africa or the world, this is a signal that providing affordable, clean and reliable modern energy is still a necessity particularly in the region discussed. **Table 2.1** gives the numbers of disease case related to indoor smoke in 2002 and it was reported that in the East African region more than 75000 deaths from diseases like pneumonia and chronic obstructive pulmonary disease due to indoor smoke inhalation occurred.[8]

Table 2.1: The 2002 WHO statistics for the indoor smoke related disease cases in East African region[8]

Country	Percentage of cases reported/%
Burundi	5.2
Rwanda	2.9
Kenya	5.8
Tanzania	4.4
Uganda	4.9

Abraham Pineo Gesner discovered the process of refining coal to kerosene.[2] This marked the world transformation from biomass fuel use to more efficient fossil fuels as the main sources of energy. Burning of coal generates more than 90% of South Africa's electricity. Eskom is the major producer and its capacity is 40.7 GW.[9] However, the forecasted peak demand is 36 GW even though independent producers and imports produce about 3.8 GW more. Electricity prices have increased from R0.33/kW h to R0.66/kW h from 2009 to 2013.[9] This is leading to alarming consequences such as environmental and health hazards with coal burning, increases in costs to business and industry, strain to ordinary citizens and negatively affects socio-economic development. A slow industrial growth rate implies that services will be unaffordable and loss of jobs will be the ultimate consequence.[10]

Bellaby, from the UK energy policy document, regarded the energy crisis as a present event and exacerbated by global imbalances.[11] Part of these policy goals were maintaining reliable energy supplies, promoting competitive markets in the UK and beyond, and ensuring that all UK homes are heated affordably and adequately.[11] The policy identifies the energy crisis as a global problem, which must be driven by co-operation from stakeholders, citizens, government and states. However, individual citizens and societies have different lifestyles and interests culminating in problems in the implementation of certain developmental laws in providing reliable modern energy resources.

Energy demand has increased exponentially in the twentieth century.[3] Currently, the demand for energy is increasing each year as the world advances technologically and economically. Postulation of energy demand is 1.7% increase per year. The estimated energy demand by 2030 is 31657 TW h.[12]

Energy efficiency can be defined in general as energy services per unit of energy input.[13] Energy conservation reduces total amount of energy consumption. Energy consumption may decrease without increase in efficiency and *vice-versa*.[3]

There is need to effectively utilise and efficiently manage available energy resources and create a supply reliability,[14] if the world is to avoid a potential fuel crisis. On the other hand, present methods for energy generation especially in the rural areas of developing countries, where primarily wood is the source of fuel, have negative effects to the environment like

deforestation.[14] Biomass in developing countries, often used in traditional technologies for heating purposes, typically involves less efficient technologies. Common forms of biomass are wood, charcoal and animal waste.[8] Despite problems associated with biomass use, temperature change, wind and hydrological cycles affect its sustainability. Brail success story on the production and use of bioethanol as a transport fuel reduces CO_2 emissions but has ethical and economic problems associated such as potential competition for limited resources with food crops.[15] Even alternative biomass sources such as biodiesel and ethanol gel have some positive attributes which include low amounts of smoke and no odour, but ethanol may be socially unacceptable to some sectors of the society because it contains alcohol.[2]

Chemical energy is energy stored in chemicals, released or absorbed during chemical reactions. Sources include compounds from the alkane homologous series, fossil fuels and batteries.[16] Relying on chemical energy is causing problems associated with greenhouse gas emissions. Fossil fuels are the most used form of chemical energy. Fossil fuels are derivatives of buried plants and animals formed over millions of years. In general, the three main classes of fossil fuels are natural gas, oil and coal.[17] These three account for 80% of the energy used worldwide.[3] Despite the depletion of fossils fuel such as coal and oil, dependence on fossil fuel keeps rising. For example, in the USA between 2005 and 2020 the estimated projection is a 30% increase in energy demand. Adverse effects of fossil fuels to the environment include landscape destruction, greenhouse gas emissions, health threats from air pollution from the release of NO_X, CO and SO_2, and water pollution such as crude oil leakage, which compromises aquatic life leading to death of organisms. Use of coal and natural gas is contributing to the decline of air quality and acid rain formation from large emissions of gases such as CO_2 into the atmosphere. The ultimate negative impact is global warming, water pollution and soil pollution.

The earth's energy resources of fossil fuels are approaching depletion. Based on 1998 consumption rates, proven conventional and unconventional global oil reserves will only last for 40 to 80 years but if the estimated resource base is included then they will be available for 50 to 150 years. Gas resources, with the exclusion of methane clathrates in continental shelves, are estimated to be available for 60 to 160 years whereas for coal, shales and tar

sands it is 1000 to 2000 years.[4] The faster limited reserves are exhausted the more expensive they are to exploit.[10] Fossil fuel reserves are estimated to be depleted by the year 2044 whereas coal and gas are expected to be depleted in 2116 and 2046 respectively.[15] This compels the world to look for alternatives that are compatible ecologically and are available in large quantities. In addition, oil pricing keeps rising.[15] Developing other highly efficient techniques, will reduce global problems associated with the fossil fuel supply.[1]

2.2.2 Renewable energy resources in the modern world

The drive towards renewable energy sources has led to the investigation of new sources energy. Hazardous effects associated with use of fossil fuels have led to a shift towards other greener sources of energy such as biomass, wind, geothermal, hydroelectric, wave, nuclear technologies and solar. *Wind energy* involves the use of turbines to convert kinetic energy to electricity. Typically a gearbox, which may be absent in the latest technologies, turns a slow turning turbine rotor into faster rotating gears which convert mechanical energy to electrical energy.[5] In *geothermal energy* technology, energy is extracted from hot water and steam below the earth's surface for various uses such as industrial processes, heating up buildings and electricity generation.[5] *Hydroelectric energy* involves the generation of electricity when water fall gravitationally driving turbines and generators.[5] Power devices are used in *wave* technologies to convert ocean surface wave energy to electricity.[5] In *nuclear* technologies, heavy elements such as Uranium (^{235}U) are split to produce smaller elements such as krypton (^{92}Kr) and gamma rays. The splitting products collide with water in a reactor releasing energy that heats up water to produce steam which is used to drive turbines.[5] *Coal-carbon capture and storage* involves harvesting CO_2 from point of release and transporting it to underground reserves such as depleted oil and coal reserves.[5,6] Some types of this technology eventually cause acidification of oceans. *Hybrid photovoltaic power generation plants* reduce renewable energy consumption by combining a photovoltaic source with other forms of energy such as conventional generators powered by diesel.[7] Examples of such technologies include hybrid photovoltaic-fuel cell generation,

wind turbines and solar photovoltaic arrays and metal hydride tanks-proton exchange membrane fuel cells.[7]

Renewable energy currently provides approximately 11% of the total energy needed worldwide.[3] Depending on slight variations in each country due to political priorities, geographical location and designs of energy systems, the growth, development and potential to reduce environmental hazards and energy security drive implementation of renewable energy technology. For example, the European Union (EU) roadmap was to reduce emissions of CO_2 and SO_X by 80% by 2050, while the United Kingdom (UK) Energy policy aims to reduce CO_2 emissions by 60% by the same year.[11,16] The South African renewable energy policy shares the same sentiments. The aim for South Africa is to increase electricity generation from renewable resources such as solar energy by at least 27% and to reduce greenhouse gases.[9] Renewable energy is readily available and from a practical point of view infinite, and hence this implies security of supply. Possible renewable energy sources are water, wind, geothermal and sunlight. In the current state of renewable energy, biomass is dominating followed by hydropower then wind. Hydropower currently dominates renewable electricity generation (see **Table 2.2**). Some nations have failed to meet their energy demand from using hydropower alone due to various reasons such as inadequate water resources and land-locked geographical locations. Furthermore, the electricity infrastructure is expensive and therefore unaffordable to some nations such as Zimbabwe.[2]

Table 2.2: Global and EU renewable electricity energy generation statistics[16]

Renewable energy source	Global production/TW h	EU production/TW h
Hydropower	3471	366
Biomass	331	142
Wind	342	149
Geothermal	68	6
Solar	34	23
Other	1	1

Large scale energy generation such as nuclear power plants in developed countries are causing adverse effects to the environment and aquatic life.[18] Geothermal energy is associated with emission of CO_2, NO, SO_2 and H_2S into the atmosphere.[5] Nuclear energy produces hazardous radioactive isotope waste that can cause soil and water contamination, especially when the correct and costly disposal methods are not adhered to. To date, there have been some devastating nuclear accidents such as Chernobyl and Fukushima. Nuclear energy as a source of energy is associated with high capital, operational, maintenance and disposal costs. High costs make it a challenge for developing countries to generate electricity from this source.

The amount of electrical energy generated from wind is directly proportional to the cube of the turbine velocity, v^3. Therefore, a double decrease in wind velocity gives an eight times decrease in output power. This is a significant point of concern when relying on wind as a source of energy because minor fluctuations imply large differences in available energy. From this perspective, wind energy is not very dependable. The challenge of predicting wind velocity is the major setback on wind as a source of energy although research is currently being done in this area.[16] Furthermore, wind power generation efficiency decreases with wind turbine height.[5]

Solar energy has been identified to be a key player, in terms of renewable energy technologies, but solar is still more costly in large-scale production than biomass, hydropower and wind.[19] However, sunlight which is readily and abundantly available especially in Africa and other tropical countries, is seen as the most promising alternative source of energy.[7,19]

2.2.3 Solar energy

Solar energy is one of the most underutilised energy resources which require little maintenance.[7] The sun radiates more energy than humans can use,[4] yet solar energy is still one of the most challenging but promising renewable energy sources. Solar energy has been used as a power source in various applications such as home systems (solar cookers, water heaters and cell phone chargers), remote buildings, reverse osmosis plants,

communication and space vehicles.[7] This compels the world to do more research on solar energy in order to counteract the high initial costs currently associated with solar energy.[4] One of the factors leading to high initial costs of solar energy is because concentrated solar power (CSPs) manufacturing technology is expensive and silicon, which is scarce and expensive, is currently dominating the markets. Silicon-based solar cell production technologies are energy-consuming.[7] Photovoltaics (PVs) are simpler and more widespread than CSPs.[6] The first solar cell was based on crystalline silicon.[15] Crystalline silicon solar cells are more efficient and uses less material than amorphous silicon.[7] Other types were developed such as amorphous silicon, micro crystalline silicon, thin films and luminescent solar concentrators.[15] *Amorphous silicon* based solar cells are photodegradable and therefore performance declines on exposure to light. However, thermal annealing reverses this effect.[7,15] *Micro crystalline silicon* solar cells combine crystalline- and amorphous-silicon attributes. Micro crystalline silicon solar cells are used in large areas and are cheaper than crystalline silicon solar cells.[15] *Thin film silicon* solar cells use less material and are made up of several thin layers of doped semiconducting material combined as charge separation junctions.[15] This technology is less expensive than silicon wafers because it uses less material.[7] Materials mostly used include TiO_2, gallium arsenide and copper telluride indium diselenide. In *CSPs,* mirrors or reflective lenses focus sunlight in order to raise the temperature of a fluid in a collector. The heated fluid flow heats an engine resulting in conversion of part of the heat to electricity. CSPs can provide energy at night but more collectors are required to provide energy for storage.[5] Other types of solar cells include hybrid inorganic/organic nanostructures, organic and hybrid PVs and multilayer junctions of semiconducting quantum dots (QDs).[4,7] Organic and polymer solar cells require a good choice of an active material and have a number of cell configurations such as bulk hetero-junction, two layered, spin coated thin films and double cable polymers.[7] Solar energy has a number of social and economic benefits. Social costs such as corporate taxes will go down if energy is cheaply available and industrial production is vibrant.[10] Solar energy production will also introduce new jobs[1] thereby reducing social costs on unemployment which ultimately mobilises industrial development. An increase in available domestic energy resources increases energy security and reduces international dependence. Developing countries will be free from large national debts from energy imports. Solar panel

installation on buildings means land recovery against the traditional land-consuming energy generation technologies. Furthermore, the life span of current solar panels on the market is about 30 years and they are capable of producing energy consumed in their production in two years.[10] Exploration of nanomaterials such as nanocomposites for their intrinsic properties, such as electronic, mechanical, adsorption and thermal properties and other co-operative properties,[20] as additional alternative materials for energy generation may contribute positively to cheap solar energy generation. Nanoscience and nanotechnology are promising in this regard. The background of nanoscience and nanotechnology is covered in the next section.

2.3 Nanoscience and nanotechnology

Nano-sized structural particles have unusual physicochemical properties.[22,23] Nanoscience comprises of distinct inter-disciplinary classes of science at the nano scale where basic science laws tend to fail whilst nanotechnology is an "aiding kit" of technologies that spread through multipurpose sectors of industry.[24,25] The basis of nanoscience is the effects of physical dimensions on material properties.[26] Historically, the original sense of nanotechnology was the ability to construct products by using the bottom-up approach *via* application of techniques and tools developed to make high performance products. Richard Feyman also known as the "father of nanotechnology" presented the theoretical capabilities of nanotechnology in 1959 and the concept was popularised by Eric Dexler in the 1980s.[25] The term nanotechnology originated from a Greek word that means dwarf.[27] Nanotechnology can be defined simply as engineering at a very small scale[27] whereas a more technical definition would be the engineering of functional systems at the molecular scale.[28] The US National Nanotechnology Initiative refers to particles with dimensions less than 100 nm as nanoparticles.[25] The definition with a size limit between 1 nm and 100 nm, where size-dependent quantum effects comes into play, excludes a large number of devices and materials.[29] Nanotechnology is a general-purpose technology classified by the size of materials developed for use. This is because it offers long lasting cleaner, safer and smarter products. This technology operates at atomic and molecular scale.[24,28] In this regard, properties change due to modifications of electronic structure between quantum and continuum domains.[26] As the dimensions of a material are reduced towards the nano-scale

the density of states (or band structure) changes from continuous to discrete energy levels. Currently, nanotechnology is paving the way to achieve smarter electronics, improved health systems and treatments, advances in agriculture and clean energy devices.[24] The drive of material science has been towards nano-sized materials. Nanotechnology has applications in a wide range of materials such as tennis balls,[30] drug delivery,[31] integrated circuits[32] and catalyst supports.[33] The attributes of small components include enhanced charge carrier capabilities and functionalities due to enhanced speeds from the inertia of mass law, consumption of less power and minimum problems in thermal distortion and vibration.[21]

Small changes in orbital structure/macroscopic structural forms of carbon leads to vast and interesting properties such as improved electron mobility.[36] The carbon nanotubes (CNTs)[37] have high potential industrial applications in the electronic, medical, chemical and composite fields.[35,36] CNTs are possible materials for the synthesis of composites for use in efficient PVs. The drive is to explore nanotechnology and come up with various applications into energy generation. CNTs play a key role in nanotechnology.[40] A discussion of CNTs is given in the sections **2.4** and **2.6**, respectively.

2.4. Carbon

Carbon was confused with charcoal in ancient times and the name is derived from a Latin word for burnt wood "carbo." Antoine Lavoisier showed that diamond was a form of carbon in 1772. In the modern world carbon is the first element in the group fourteen elements with four valence electrons. The narrow energy gap between the 2s and 2p orbitals allows electron promotion. Energy gained from covalent bonding with adjacent atoms compensates for the electronic configuration of higher energy states. Hybridisation has accounted for the diversity of carbon based structures found in nature and artificially synthesised.[41] Sp^3 hybrids of C are more thermodynamically stable than sp^2 hybrids.[41] Carbon, by the virtue of its unique hybridisation properties and sensitivity to perturbations in synthesis conditions, can be easily manipulated. The forms of carbon known today are listed in **Table 2.3**.

Table 2.3: Properties of some carbon allotropes[42]

Type	Hybridisation	Crystal structure	Band gap/ eV	Conduction type
graphite	sp^2	hexagonal	0.00	conductor
graphene	sp^2	-	0.03	semi-conductor
MWCNTs	sp^2	cylindrical	0.30-2.00	metallic
diamond	sp^3	cubic	5.50	insulator
Bucky-balls	sp^2	truncated icosahedron	0.5	insulator

Diamond is a three dimensional four-fold coordinated sp^3 rigid structure while graphite is a sp^2 three-fold coordinated planar structure. Fullerenes have found the most PV energy harvesting applications since they are thermally stable, non-toxic, bio-compatible, hydrophilic functionalised and have a high surface area.[43] Unfortunately, until 1779 graphite was confused to be a form of lead. Graphite has weak van der Waals forces between planes and stronger shorter covalent in-plane carbon bonds.[44] Graphite has delocalised electrons since C atoms only uses three of its valence electrons in bonding. Electrons can move along the layers and therefore it conducts electricity along the layers. CNTs consist of graphite-based structures. The next section presents some background information on CNTs.

2.4.1 Carbon nanotubes

CNTs can generally be visualised as rolled-up graphene sheets held together by van der Waals forces. Semi-fullerene-like caps may close the CNTs. Diameters are in the nanometre (nm) range.[21,23,35,37] The single dimensional geometry of a CNT tubule [21,35,45] induces quantum confinement in radial and circumferential directions.[18,46] CNTs are the stiffest and strongest nanomaterial with a Young's modulus of 1 TPa and a tensile strength of 50 GPa. The hybridisation of carbon strongly influences the physical, chemical and electronic

properties of CNTs. In terms of the electron transport properties of CNTs, defects and heteroatoms influence electronic conductivity and ballistic transport of electrons.[46,47] CNTs have high thermal and electrical conductivity, and good chemical stability. All these properties can be altered. The current research and development is focused on controlling parameters at the nano level such as porosity, purity, homogeneity, straightness, graphitic nature and CNT chemical state.

Classification of CNTs is according to the number of graphene sheets, chiral angle, and diameter.[48] The main classes of CNTs are single-walled (SWCNTs), double-walled (DWCNTs) and multi-walled carbon nanotubes (MWCNTs) (see **Figure 2.1**). SWCNTs exhibit metallic and semi-metallic behaviour depending on chirality.[23,35,49]

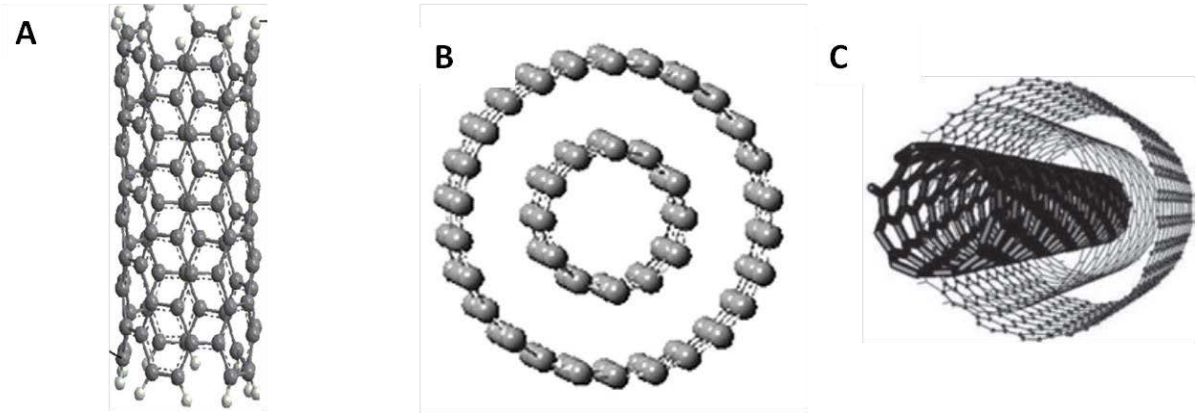

Figure 2.1: The structures of carbon nanotubes: (**A**) single-walled, (**B**) double-walled and (**C**) multiwalled carbon nanotubes[50-52]

2.4.2 Single-walled carbon nanotubes

Single-walled carbon nanotubes (SWCNTs, shown in **Figure 2.1A**) may be defined as a rolled up sp^2 bonded graphene sheet.[21] Position vectors of SWCNTs can be given by using the (n, m) integers for the c, $a_1$and a_2 direction vectors. Therefore, lattice vectors can be given by a general chiral vector (see **Figure 2.2**).

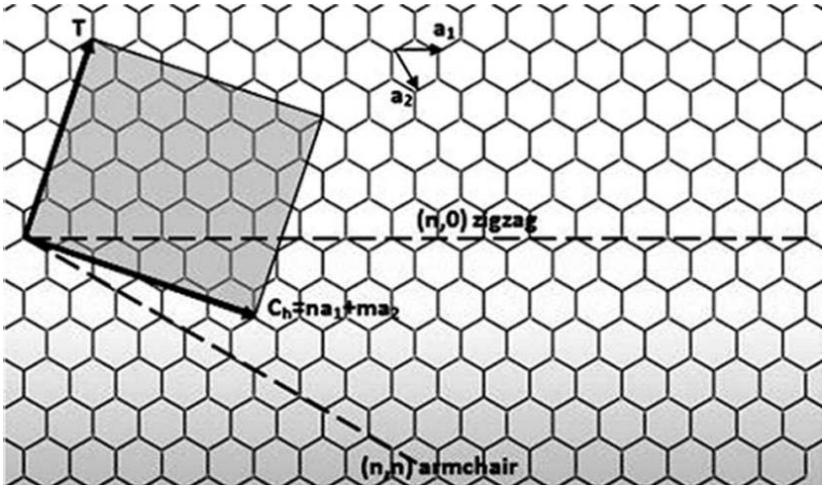

Figure 2.2: Position vector of SWCNTs[21]

$$\vec{C} = n\overrightarrow{a_1} + m\overrightarrow{a_2} \quad \textbf{(equation 2.1)}$$

$$\text{length of } \vec{C} = \left|\vec{C}\right| = a\sqrt{n^2 + nm + m^2} \quad \textbf{(equation 2.2)}$$

The "a" is related to carbon bond length. The chiral vector points from the first atom towards the second atom.[21] Varying integers (n, m) generate different diameters and helical arrangement of hexagons.[53] The chiral vector is perpendicular to the lattice vector. The length of the chiral vector is the circumference of the SWCNTs. The chiral vector and the corresponding chiral angle define the CNT type as chiral, armchair or zigzag. If n ≠ m and $0° < \theta < 30°$ then it is chiral or if n = m it implies armchair and the corresponding $\theta = 0°$, lastly if m = 0 it is zigzag and $\theta = 30°$.[21] Electronic properties are influenced by the structure of SWCNTs.[41,53,54] For example, if n = m then SWCNTs are metallic but if n - m is three times an integer then an extremely small band gap arises and the SWCNTs will be metallic. For other values of n - m SWCNTs are semi-conducting with an appreciable band gap.[53] Research effort in hybrid CNT conjugated molecule systems has largely focused on the use of SWCNTs.[49]

2.4.3 Double-walled carbon nanotubes

Double-walled carbon nanotubes (DWCNTs, shown in **Figure 2.1 B**) consist of two concentric graphene sheets.[53,55,56] The van der Waals forces hold graphene sheets in DWCNTs. The inter-shell distance varies between 0.33 nm to 0.42 nm depending on the geometrical orientation of either sheet.[57] Inter-layer spacing influences the stability of DWCNTs. DWCNTs are a one-dimensional material between SWCNTs and MWCNTs. They are more thermally stable and mechanically stronger than SWCNTs.[51,53] Properties are difficult to identify due to inter-shell interactions.[56] The two shells may have the same or different chirality.[51] Chirality affects the buckling load of DWCNTs and the effect increases with increase in index of translation.[55,57] Electronic properties can be determined in a similar way as with SWCNTs by using chiral indices (see **Figure 2.2**) and can be different on isolating the tube sheets.[51,56] There exists low potential for current leakage between sheets. The band gap structure is influenced by the superposition of the graphene sheets.[56] Covalent functionalization with groups such as NH_2 and COOH can be used to control the electronic properties and in band structure engineering. The outer sheet shields the inner one from external perturbations. Application of DWCNTs include sensors,[51] hydrogen storage,[58] nano-electronic devices,[56] in high strength materials and reinforcement in composites.[57]

2.4.4 Multiwalled carbon nanotubes

MWCNTs are generalised as structures comprising of a coaxial arrangement of graphene sheets. The graphene interlayer spacing in MWCNTs is 0.34 nm (see **Figure 2.1 C**).[59,60] Rolling of graphene sheets occurs at specific discrete angles.[61] MWCNT electron transport properties depend on structural effects such as imperfections. MWCNTs are metallic in nature.[62] In the nanometre range, physicochemical properties do not depend on chemical composition only but also on particle size and shape.[41,63,64] Some characteristics of MWCNTs reported in the literature are discussed in the next section.

2.4.4.1 Physicochemical properties of MWCNTs

The stiffness and axial strength of MWCNTs depends on the carbon-carbon sp^2 bonding[60] and is between 11 and 63 GPa. Radial compressibility from small forces is 10 GPa.[46] The elastic Young's modulus of MWCNTs can exceed 1 TPa.[59]

MWCNTs readily agglomerate due to van der Waals forces. MWCNTs have two regions of reactivity: carbon bonds at the tip are more reactive due to high strain from large curvature and the second reactive region is the cylindrical region. The low activation energy of the former confirms the difference in reactivity.[37,65] Although there is partial loss of electronic structure/optical properties and material loss, oxidative functionalization is applicable to both regions.[37] The combination of the rolling, radius and length of MWCNTs influences the nanotube properties.[45,66] MWCNTs absorb hydrophobic substances.[67] MWCNTs reduce catalytic activity and lower desorption of reaction products when applied as catalyst supports in hydrophilic reactions using a hydrophilic solvent.[68]

The numerous concentric graphite sheets in MWCNTs[37,45] render them more efficient electron carriers/acceptors.[37] MWCNTs can be viewed as long molecular wires which allow free electron movements.[69] The tubes act as wave guides with ballistic behaviour. Ballistic behaviour is one in which the mean free path of electrons is longer than the length of the tubes. Individual MWCNTs participate in quasi-ballistic conducting behaviour. MWCNT layers are a set of connected interacting layers though not completely close. This means multiple walls take part in electrical conductivity and a large external diameter implies a small band gap.[69,70] The overlap of graphene sheets in MWCNTs affects electronic properties in addition to chirality. Ellis and Ingham[71] reported that MWCNTs are semimetals with overlapping occupied and empty bands. The electrical conductivity of MWCNTs is $\sim 1.85 \times 10^3$ S cm^{-1} and the current density along the axis is $\sim 10^7$ A cm^{-2}.[70]

A combination of nanotubes with various electron donors led to a new generation of donor-acceptor nano-hybrids used for the development of photovoltaic cells.[37] Their good electron acceptance and storage capability makes them good charge trapping sites.[72] Semi-conducting CNTs are generally p-type.[42,73] Zhu *et al.* [42] reported the MWCNT resistivity, electron mobility and hole mobility at 300 K to be 0.1 Ω cm, 10^8 cm^2 V^{-1} s^{-1} and 10^3 cm^2 V^{-1} s^{-1} respectively. The thermal conductivity of MWCNTs can be as high as 3000 W m^{-1} K^{-1}.

MWCNTs are good candidates for DSSCs because they are chemically stable, have low resistivity,[48] and are stiff and strong.[45]

2.4.4.2 Synthesis of MWCNTs

The MWCNT market is expected to reach a value of US $ 1 billion by 2014 and finally US $ 9.4 billion by 2020.[47] MWCNTs have lower production costs (estimated production cost is $5/g) and are available in large quantities relative to SWCNTs.[42,65,73] MWCNTs are synthesized by three main methods, i.e. laser ablation, arc discharge[74] and chemical vapour deposition (CVD).[75] A catalyst is used to enhance the MWCNT yield.[40,66]

In the *laser ablation method*, a graphite piece is vaporised by laser irradiation under high temperature in an inert gas atmosphere. The product quality is dependant on the reaction temperature. In the *arc discharge method*, an electric arc vaporises a hollow graphite anode packed with graphite powder and a mixture of transition metals such Co and Fe. The yield is affected by gas flow rate, pressure and metal concentration.[76] The laser method is suitable for low yields of MWCNTs. The biggest problem with the arc discharge method is the removal of catalyst material and other graphitic contaminants. The *CVD method* is a thermal dehydrogenation reaction in which a transition metal catalyst such as Ni or Fe lowers the bond energy resulting in easier bond breaking in hydrocarbons forming carbon and hydrogen.[76] The basic CVD definition can be deposition of a solid on a heated surface from a chemical reaction. Chemical vapour catalytic grown MWCNTs have fewer impurities and more defect density than arc grown tubes.[77] CVD techniques tend to be the most popular method, perhaps due to their input cost advantages[61] and the ease of scale-up. Experimental parameters such as catalyst, nature of carbon source, flow rate, temperature and reactor design influence homogeneity, purity, morphology, structure and quality of MWCNTs.[47] MWCNTs are reported to occur as by-products of natural and industrial processes such as methane- and propane- based stoves.[78] Innovations in using those nanotubes will be an effective utilisation of organic fuels.

2.4.4.3 Modification of MWCNTs for applications

Applications of MWCNTs include electric field emitters, shielding agents, lithium batteries, electromagnetic wave absorbers, hydrogen storage materials, fillers in nanotube based conducting composites, super capacitors and nano-probes.[45] A survey on possible modifications towards energy generation goals follows. MWCNTs are added to functional materials to enhance key properties such as an increase in surface area, activity and conductivity.[73,79] Generally, nanoparticles or bio-molecules functionalise MWCNTs when used in nanoscale devices such as photo-electrochemical cells, molecular electronics and biosensors. This is because these applications require low resistance contacts and the organised assembly of MWCNTs onto other functional units.[80] In some instances controlled surface modifications, such as acid treatment, is a prerequisite. After synthesis of MWCNTs, the material may need to be purified to get rid of metallic catalysts and carbonaceous material.[81] One such method is vacuum annealing, which removes defects and amorphous material. However, the most common method is to treat MWCNTs with one or more acids.

Acid treatment with HNO_3 should be below its degradation temperature (130 °C) to prevent release of NO_2 as a by-product. Acid treatment might not remove metal catalyst particles completely due to inability to reach encapsulated iron.[42] Sonochemical treatment in a mixture of concentrated nitric and sulfuric acids cause opening of the tube cap, shortening of tubes, defect formation and introduction of functional groups on the sidewalls.[42] Acid strength and time of treatment have been the most varied parameters in this area. A milder treatment, using a single acid at moderate concentration (3-6 M), involving reflux minimises tube shortening.[82] Acid treatment influences the chemical properties, increases solubility and purifies MWCNTs.[45,65] This allows for the manipulation of MWCNTs for various functions by influencing the electronic structure and surface reactivity.[82] Organic stabilisers are used to prevent agglomeration by some researchers.[20]

MWCNT modifications are either on the side walls or the inside along the hollow core.[45] There exist two broad ways of modifying MWCNTs involving either the conjugated skeleton on the surface of MWCNTs in chemical reactions to introduce groups on the surface or adsorption of molecules through non-covalent interactions. Surface modification can be done either by boiling with oxidative acids or associating with pyrene derivatives.[80] Some of

the reported methods of MWCNT modification include plasma activation,[3] electrophilic addition,[83] ozonolysis,[53] addition of inorganic compounds,[26] radical addition,[84] sidewall halogenations,[9] mechano-chemical functionalisation,[54] cycloaddition,[17] polymer grafting,[8] and hydrogenation.[13] A combination of titania and MWCNTs produces excellent composite material but composition proportions ties into the idea of investigating optimum ratios. The next section presents some background information and attributes of titania.

2.5 Titania

Titania has been applied in solar-based devices such as photo-catalysts and DSSCs. TiO_2 has other applications in cosmetics, catalysts, ultra-thin capacitors, chemical sensors, anti-reflecting coatings, micro-electronics and as a white pigment because of its chemical and physical properties.[20,85,86] ZnO offers much competition to TiO_2 since it has a similar electronic structure, higher electronic mobility and can be synthesised by a variety of techniques which is a positive attribute to our low cost goals. However, it is difficult to determine the most suitable of the two since photo conversion efficiency (n) depends on a number of parameters and ZnO lacks reproducibility in synthesis.[87] A brief background of the intrinsic properties of titania is given in the subsequent sections.

2.5.1 Titanium dioxide attributes and setbacks

Titanium dioxide is a non-toxic, environmentally friendly and chemically stable abundant substance with reported excellent photo-catalytic properties by many scientists.[72,73,88,89] TiO_2 is mainly used due to its low cost, availability, chemical and physical properties as a thermoelectric material. Attributes of a good thermoelectric material include high electrical conductivity and low thermal conductivity.[81] However, since titanium is a transition metal, it has high surface free energy and this causes particle agglomeration problems.[42]

Titanium dioxide has a low quantum yield associated with recombination of photo-generated electrons and holes.[73] Titanium dioxide has a large refractive index and is transparent in the range 350 nm to 1100 nm.[85] It also has good transmittance in the visible region and is associated with large dielectric constant values.[86,90] Titania is an n-type

semiconductor due to oxygen vacancies.[91] Variations in titania properties are due to different synthesis methods and post-treatment conditions.[86,91]

2.5.2 Forms of titania

Available titanium oxides include titanium monoxide (TiO), titanium dioxide (TiO_2) and titanium sesquioxide (Ti_2O_3). Titanium dioxide exists in three phases, i.e. rutile, brookite and anatase. *Rutile* is tetragonal (a = 0.4593 nm and c = 0.2959 nm) with a band gap of 3.02 eV.[86,92] Rutile is the most dense and thermodynamically stable phase.[86,92,93] *Brookite* is orthorhombic (a = 0.9182 nm, b = 0.5456 nm and c = 5143 nm) with a band gap of 2.9 eV.[86,92] *Brookite* is the least thermodynamically stable and is obtained *via* complex preparation procedures but as a mixture with one of the other two polymorphs.[93] *Anatase* is tetragonal (a = 0.3785 nm and c = 0.9514 nm). In this phase, Ti^{4+} is octahedrally co-ordinated to six O^{2-} ions and has the widest band gap of 3.2 eV.[18,20,88,94,95] Phase transformation from anatase to rutile is observed at ca. 500 °C. The two polymorphs have distinct peaks in powder X-ray diffraction (XRD), Raman spectroscopy and Fourier transform infrared spectroscopy (FTIR). Anatase can only be excited by light with wavelengths shorter than 387.5 nm.[92] The anatase polymorph exhibits excellent conductivity and was therefore the target polymorph of this work for use in DSSC applications. Titania exists in various morphologies such as nanotube arrays,[96] nanotubes,[91] rod-like nanospheres,[97] nanofibres,[98] nanorods,[99] and snow-like nanostructures.[100] One dimensional TiO_2, such as nanotubes and nanowires, is preferred to other dimensions because of the enhanced surface area for dye absorption,[89] intrinsic electron mobility,[95] semi-directed charge transport and high red light scattering culminating in enhanced blue light-harnessing.[95]

2.5.3 Exciton behaviour in titania

Illumination of inorganic materials generates free charges directly but in organic materials it causes delocalisation of photo-excited states, or excitons. Excitons are bound electron-hole pairs which must dissociate into a free electron donor/acceptor for a photovoltaic system to deliver appreciable photocurrent.[101] This typically requires a smart material to happen

efficiently. Smart materials are materials that have the ability to respond to an induced external stimulus. The material must have inherited sensing and/or actuation capability.[43] Pure titania has high recombination rates.[80] Bing-shuan *et al*.[72] reported that recombination can be minimised by metal coating. Rice grain titania is better than titania Degussa P25 in PV.[95]

Work reported by various researchers indicates that TiO_2 is suitable for our work since it is stable against photo-corrosion and chemical corrosion amongst other advantages. **Table 2.4** shows some of the titania structures reported for applications in light-harvesting.

Table 2.4: Selected performance of TiO_2-based solar cells [87]

Structure	J_{SH} /mA cm^{-1}	V_{oc} /V	FF	n /%	Light intensity /mW cm^{-2}	Year
porous	4.71	0.87	0.68	2.81	100	2011
Nano-rod	4.33	0.78	0.65	2.20	100	2009
Nano-rod	2.73	0.64	0.56	0.98	100	2008
nanotube	1.80	0.62	0.58	0.50	100	2011

Illumination of a sensitizer attached to titania film causes absorption of the incident light. The electron (e^-) in the dye/sensitizer absorbs the incident radiation. The e^- in the dye becomes excited to a higher energy level than the CB of titania leaving behind a positive electron hole. The electron and hole (excitons) formed are bound by electrostatic forces of attraction.[18,94] The force required to break this Columbic attraction is provided by the energy level offset of the sensitizer LUMO and TiO_2 CB.[18] The electron moves *via* diffusion across the TiO_2 interface[95] and the stability must be maintained.[73] Excitons have a short diffusion length.[87] The disordered motion of the photo-injected electrons in the TiO_2 network increases the probability of recombination with the oxidised sensitizer or electrolyte. The e^- moves *via* the external circuit to the counter electrode. At the counter electrode, the e^- moves to the oxidised species of the redox couple electrolyte. The reduced species of the electrolyte then transfers the e^- to the dye and the ground state dye is regenerated.[95] **Figure 2.3** illustrates the mechanism involved in DSSCs.

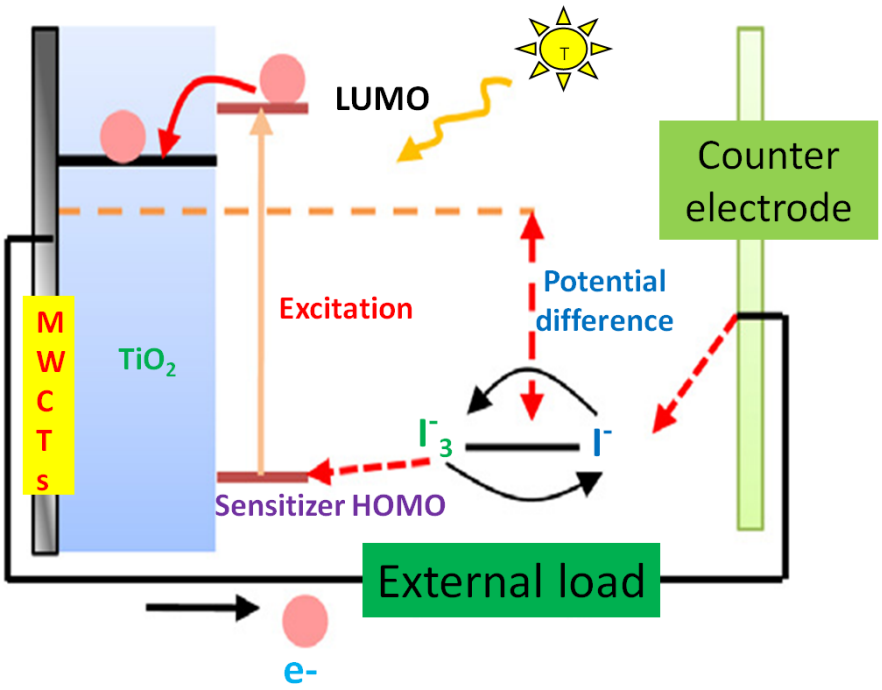

Figure 2.3: The mechanism involved in the electric generation during light-harnessing[95]

The generation of photocurrent on illuminating electrodes is a sign of charge collection efficiency. It has been reported that a system with graphite as counter electrode and a MWCNT/TiO_2 electrode increases the photocurrent five times than a system with no MWCNTs incorporated.[102] TiO_2 dominates the electron transfer processes. Holes from photon-induced e^-/h^+ pairs must move from the TiO_2 phase and a sensitizer, such as a dye, facilitates this event. The conductive structure of the MWCNT scaffold facilitates the separation of the photo-generated electron/hole pairs at the MWCNT interface. The local anodic potential across the TiO_2/MWCNT interface contributes to this event. An effective pathway culminating in high photocurrent values is subject to MWCNTs/TiO_2 interfacial area and electron conductivity.[66,79,102] MWCNTs have good electron capture capacity compared to TiO_2 due to a lower Fermi level, ground state energy (see **section 2.8.10**).[18,73] Jiang *et al.*[103] reported a decrease in transfer of charge and an increase in anodic potential on addition of MWCNTs on titania. Electron transfer is prompted from the titania CB towards the surface of the MWCNTs due to a lower Fermi level. The Schottky barrier forms an interface between the MWCNTs and TiO_2. Photo-generated electrons move towards the

MWCNTs freely while the holes move towards the VB of titania inhibiting recombination and creating a large specific surface area for dye adsorption.[73] A report by Ming-Liang[79] tends to present a contradictory mechanism to the mechanism mostly reported on electron movement in the composite, suggesting excited electrons move from valence band of the MWCNTs to the conduction band of TiO_2.

2.5.4 Titania band gap modification

The band gap is the energy range in a solid with electron state probability of zero. It is the energy required to free an electron from its orbit around the nucleus to become a mobile free electron. This gap influences electrical conductivity. Solids with large band gaps are insulators whereas conductors have overlapping valence and conduction bands. Band gap engineering is the process of altering/controlling the energy gap between the valence band (VB) and conduction band (CB) of a material by varying composition. The band gap effects on conductivity in solid-state solar cells can be minimised by the use of sensitizers such as quantum dots (QDs) and dyes.

A few attempts to modify the band gap in titania via doping have been reported. Absorption of electromagnetic radiation by anatase TiO_2 occurs in the UV region (below 385 nm).[72,95] The UV region accounts for 5% of the total solar energy that reaches the surface of the earth.[72,87,88] Attempts to shift the TiO_2 optical response by using cationic doping (Fe, Co, Ni, etc.) and anionic doping (N, C, F, etc.) [20,72,73,88] have been reported but this may create recombination centres for electrons and holes (see **Table 2.5**). Most of the articles reviewed that report on doping of titania for application in DSSCs application do not report the observed band gaps. Co-deposition of metals and mixing two semi-conductors are other ways of adjusting the band gap.[88]

Table 2.5: Some reported titania doping outcomes [104-108]

Dopant	General observations and band gap
2 wt.% V^{5+}	The V^{5+} species substituted Ti^{4+} by creating Ti^{4+} vacancies in the lattice. Particle sizes were reduced and had larger surface areas than undoped titania. Band gap was 3.8 eV
N	The e^-/h^+ recombination decreased and improved electron conductivity. P-N junctions formed with anatase at the P junction and rutile at the N junction. Band gap was 3.1 eV.
I^-, I^{7+} and Zr (co-doping)	Surface area was large due to I^- and I^{7+} species. Increase in electron capture due to Zr ions and reduced e^-/h^+ recombination than undoped titania. Band gap was 2.73 eV for iodine doping alone and 2.52 eV on co-doping.
Ca^{2+}	Ca^{2+} occupied the quadivalent Ti^{4+} and this increased net electron concentration and conductivity. Electron injection efficiency was also improved.
S^{6+} and S^{4+}	S^{4+} was incorporated into the lattice and S^{6+} due to SO^-_4 adsorbed on titania surface. Reduced particle surface, larger surface area and reduced e^-/h^+ recombination than undoped titania. Band gap was 2.78 eV.

2.6 Nanocomposites

According to the English Oxford dictionary, a nanocomposite is a solid material made up of more than one phase having dimensions less than 100 nm. General examples include gels, colloids, copolymers and organic-inorganic mixtures and some specific examples include N-doped ZnO-Ag,[109] SnS_2-graphene,[110] and MWCNT-titania.[95] Nanocomposites are synthesised

to improve various functional properties of components such as reduction of e^-/h^+ recombination,[111] enhancing mechanical and catalytic properties,[109] and enhancing flexibility, dielectric, ductility and processability.[112] Applications of nanocomposites include thin film capacitors and batteries,[110] electrolytes,[113] fuel cells,[97] solar cells[95] and photocatalysis.[111] The properties of nanocomposites depend on the parent materials, and the morphology and interfacial characteristics.

2.6.1 MWCNT-titania nanocomposites

In this section, the review is directed to nanocomposites consisting of MWCNTs and titania. The reasons for using MWCNTs in nanocomposites include their cost-effectiveness in mass production, high aspect ratio, nanosize and low density.[70] Carbon nanotubes are used to enhance carrier transport and achieve a light-trapping effect.[94] TiO_2 supported on MWCNTs to make a composite material have been reported to have excellent photocatalytic capability.[114]

2.6.1.1 Precursors

Most research articles reporting the synthesis of MWCNT-titania nanocomposites opted for metal organic precursors and the reasons for such choices were not made clear in the articles. Precursors of TiO_2 include titanium(IV) isopropoxide (TIP), titanium propoxide (TPP), titanium(IV) n-butoxide (TNB)and titanium methoxide (TM).[79] Various types of composites have been reported which include titania nanoparticles on MWCNTs, titania layer coating on an aligned MWCNT array, MWCNTs incorporated into a titania film and a titania layer coating MWCNTs.[73]

2.6.1.2 Preparation

The method used in composite preparation influences the physical properties. Composite materials have been fabricated by a number of ways such as sol-gel synthesis of TiO_2 in the presence of MWCNTs,[115] mechanical mixing,[39] electrospinning methods,[95,116] electrophoresis deposition,[117] novel surfactant sol-gel wrapping method,[102] blending,[118]

physical vapour deposition, sputtering deposition,[103] supercritical fluid deposition,[20] capillary action, hydrothermal[67] and chemical vapour deposition (CVD). Creation of a homogeneous surface layer on the MWCNT tube walls remains a challenge.[102] Reports are that CVD and electro-spinning methods produce uniform coated composites.

By means of the sol-gel method, Jitianu *et al.*[119] reported a 3-5 nm thick homogenous coating of titanium dioxide on MWCNTs. The authors also noted that the tube walls were partially damaged when using the hydrothermal method and suggested that the sol-gel method was a better method for tube coating. Ming-Liang *et al.* [79] stated that the sol-gel method gives a heterogeneous non-uniform coating of MWCNTs by TiO_2 with bare MWCNTs and random aggregation of TiO_2 on the MWCNT surface. A trial of this method by possibly employing surfactants to arrive at ideal composites with less sophisticated equipment might contribute positively.

2.6.1.3 Properties

MWCNTs are used in composites with titania due to their high chemical stability and low space charge recombination in resulting composites.[67] The high aspect ratio (length to radius ratio) and high conductivity of MWCNTs makes them preferred as a conducting composite material. Nanotube composites have preferred morphology.[21,42,61,120] Li *et al*.[66] reported that a high MWCNT ratio in MWCNT-titania nanocomposites resulted in higher photocurrent values. However, the insolubility of MWCNTs is a barrier to their applications. Instead, various solvents are used to disperse MWCNTs in composite synthesis. Organic solvents reported in literature for dispersion of MWCNTs include chloroform, toluene, water, carbon disulfide, ethanol, methanol and acetone.[78] Acid treatment, discussed in **section 2.4.4.3**, is vital for using MWCNTs in reactions/chemical processes since it causes de-bundling first, thereafter it introduces functional groups that help with the solvation and prevent unwanted agglomeration into bundles,[65] and it removes amorphous carbon which has low photoconductivity.[42]

2.6.1.4 Application in light-harvesting

Most reported nanocomposites of MWCNT-titania in literature were applied in photocatalysis for water purification. Other applications include hydrogen evolution, DSSCs, CO_2 photoreduction and sensor devices.[102] The combination of charge transfer abilities of MWCNTs and effective titania absorptivity in composites is one of the breakthroughs in photo-catalytic world. The electronic conductivity of titania-based nanocomposites increase with MWCNT composition.[66] Most reported light-harvesting related work is based on enhancing charge transfer and reducing e^-/h^+ recombination but MWCNTs can be used as sensitizers to enhance absorption.[72] MWCNTs provide spatial confinement of TiO_2 and a large supporting area contributing to fast observed redox reactions.[66] MWCNTs increase the conductivity of titania and minimise recombination.[73,95] Properties of CNTs and TiO_2 have been combined in various attempts to increase efficiency of solar cells. For instance, Wang *et al.*[79] reported a decrease in agglomeration and an increase in surface area of TiO_2 on making composites with MWCNTs. Sawatsuk *et al.*[48] reported a 50% energy conversion efficiency increase in a titania-based composite solar cell with 0.025% MWCNTs. MWCNTs resulted in high J_{sc} with a slight increase in V_{oc}. Energy conversion efficiency was observed to decrease at higher MWCNT content due to optical absorption of carbon material.[48] MWCNT-TiO_2 nanocomposites have achieved a 60% energy conversion efficiency increase.[95] A 0.2 wt.% CNT electro-spun titania composite was reported to achieve 35% enhancement.[95] TiO_2-based solar cells made by Weng *et al.*[114] had a two-fold increase in photocurrent on inclusion of MWCNTs.

There is need to investigate the physicochemical properties of nanocomposites for technological gain in solar cells.[23] Characterisation of nanocomposites and investigation of their physicochemical properties towards light-harvesting functionality is the key to this work and a discussion of relevant characterisation techniques follows in the subsequent sections. Peining *et al.*[95] reported that the ideal titania thickness on MWCNTs in DSSCs is 11 μm at 0.2 wt.% MWCNT on TiO_2. Beyond that, it is suspected that a decrease in optical transparency and dye-loading could be the reasons for a decrease in efficiency since the two factors depend on TiO_2 content in the nanocomposite. Cong *et al.*[73] used a molten salt method (TiC and MWCNTs) and the controlled oxidation process to coat TiO_2 on MWCNTs.

An investigation of the composites synthesised by the sol-gel and CVD methods in terms of efficiency in photovoltaic applications will contribute immensely to cheap DSSCs, and this is one of the key aims and objectives of this work. A review of the performance of DSSCs is discussed in detail in **section 2.8**.

2.7 Characterization methods for nanomaterials

MWCNTs have unique morphology and dimensions. This distinguishes them from other forms of carbon and there are several techniques that are used to characterise MWCNTs.[121] Titania forms three distinct phases and different morphologies as described in previous sections, thus there is a need to characterise it fully both physically and chemically. The next sections review various techniques fundamental to the elucidation of the properties of nanocomposites for light-harvesting applications. The techniques that can be used to characterise nanomaterials include scanning electron microscopy (SEM), transmission electron microscopy (TEM), Raman spectroscopy, thermogravimetric analysis (TGA), Fourier transform infrared spectroscopy (FTIR), textural characteristics, diffuse reflectance, inductively coupled plasma-optical emission spectroscopy (ICP-OES), photoluminescence (PL), X-ray photon electron spectroscopy and powder X-ray diffraction (XRD).

2.7.1 Thermogravimetric analysis

The technique is a thermal method that measures changes in weight with temperature under inert, reducing or oxidizing conditions.[114,115,122] **Figure 2.4** shows TGA instrument. TG curves of pure substances provide a fingerprint of that substance. Thermal stability is deduced from the oxidation temperatures of a sample.[115] Oxidation temperature is influenced by carbon-carbon bond-length, curvature and strains.[65] Functionalization of MWCNTs in composites introduces different effects on the overall structure, thereby affecting thermal stability. Furthermore, the purity of MWCNTs has an effect on oxidation temperature. Pure MWCNTs approach theoretical in-plane graphite defect-free carbon bond properties.[102]

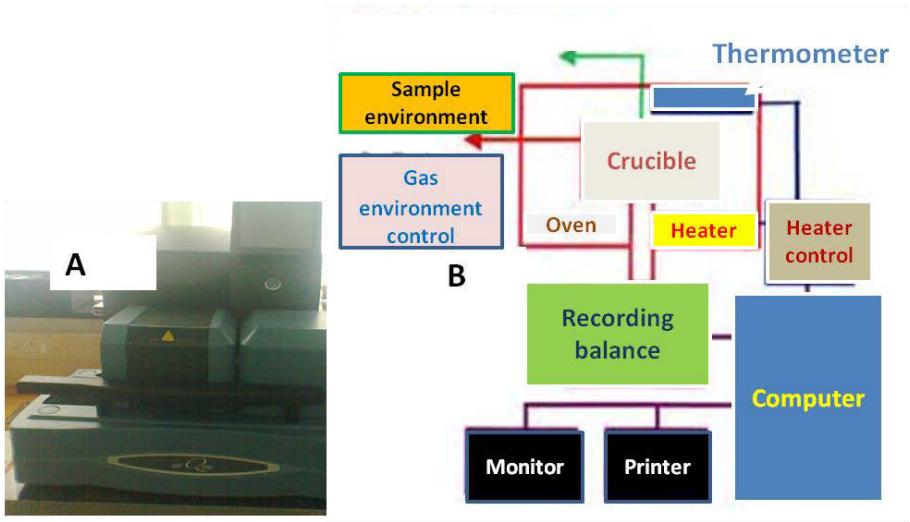

Figure 2.4: The thermogravimetric analysis instrument: (**A**) TA Instruments Q series™ Thermal Analyser TGA (Q600) model and (**B**) the various parts involved in the system

Defect-free graphite-like structures will be the most thermally stable structures of MWCNTs.[122] However, real MWCNT structures deviate from the ideal and hence characterisation is crucial prior to various applications. Defects in MWCNTs include dangling bonds, edges, vacancies, dislocations, and steps and these defects are reactive with oxygen at high temperatures. Other defects are five- and seven-member rings forming azulene unit substitutes to naphthalene in MWCNTs.[122] Using this technique, below 200 °C water and organic impurities are removed then oxidation follows.[65,123] Mun *et al.*[123] reported the temperature range for MWCNT of oxidation to be between 400 and 650 °C. Acid-treated MWCNTs have a broader temperature range.[123] MWCNT oxidation is reported to start between 440 °C and 450 °C. In TGA, sample mass is limited by the less dense nature of MWCNTs and the size of the pan. A 3-10 mg sample size was used by Lehman *et al.*[102] while Mun *et al.*[123] used 10-15 mg of MWCNT at a heating rate of 20 °C/min up to 400 °C. Both Lehman and Munn obtained good and reproducible thermograms. TGA can also be used qualitatively to confirm the presence of metals in composites without specific identification. Energy dispersive X-ray spectroscopy (EDX) can be used to identify specific metals.[79,122] Bom *et al.*[122] reported that the metal catalyst has little or no effect on oxidation stability of MWCNTs.

2.7.2 Raman spectroscopy

The basis of Raman spectroscopy is inelastic scattering of a monochromatic excitation source. A Raman instrument is shown in **Figure 2.5A**. In this technique, photons of known energy are irradiated on molecules or polyatomic ions. Photon absorption by the molecules causes transformation to high-energy states. The molecules use some of the energy in transformation to high vibrational and rotational states. Excess energy is emitted as photons. Raman spectroscopy is a result of change in polarizability. Raman spectroscopy is a quick non-destructive vibrational spectroscopy that provides some structural information on the graphitic nature of carbon-based materials. Illustration of laser during sample analysis in Raman spectroscopy is shown in **Figure 2.5B**.

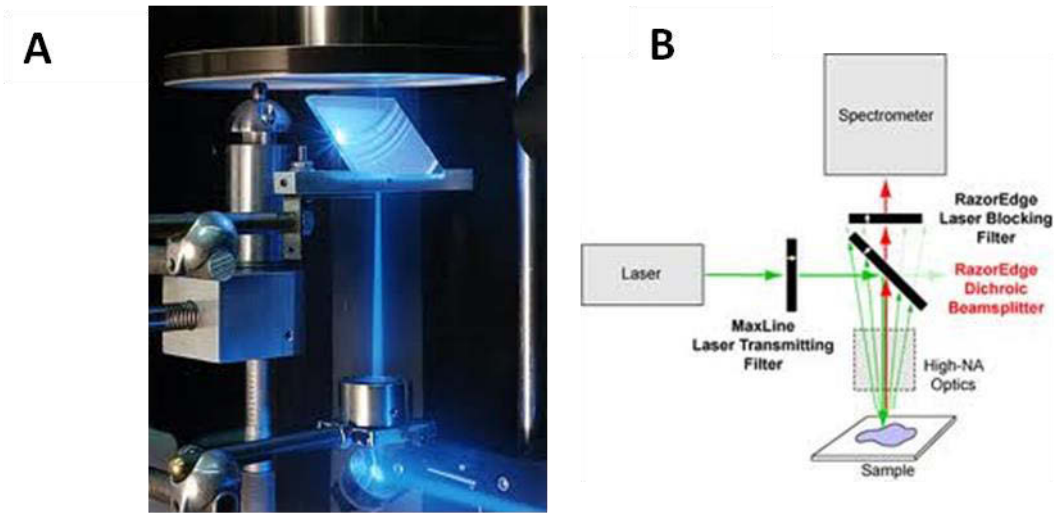

Figure 2.5: The (**A**) Raman instrument and (**B**) illustration of laser in sample analysis in Raman technique

2.7.2.1 Raman spectroscopy in carbon nanostructures

Raman spectroscopy can be used to analyse various forms of carbon, such as amorphous carbon, activated carbon, graphene sheets, and carbon platelets, SWCNTs, DWCNTs and MWCNTs. MWCNTs have a distinct Raman fingerprint.[40] For MWCNTs, several bands are observed depending on the laser used. For example, the D band is located at ca. 1350 cm^{-1} for MWCNTs,[124] the D' (or G') band may occur at ca. 1615 cm^{-1}, the radial breathing mode is mostly located between 100-500 cm^{-1} and the G band is close to that of graphite located at

ca. 1580 cm^{-1}. The basis of the technique is that the G band is the first order Raman scattering [82,102] from the tangential in-plane stretching vibrations of carbon bonds within graphene sheets, the Raman allowed phonon mode ($E_{2(g)}$).[125] The incident laser power influences the E_{2g} mode since an increase in temperature increases the carbon bond distance.[125] MWCNTs resemble graphite due to their large diameter and reduced strain. The origin of the D band is not yet fully understood.[65] The D band is thought to be the defect dependant second order Raman scattering, $A_{(g1)}$ mode.[126,82] This is due to disordered defects or ion interaction between graphitic walls.[65] The position of the D band is more defect dependant than curvature on SWCNTs.[82] The radial breathing mode is due to the innermost tube diameter of MWCNTs and D' is due to long range order in the sample.[127]

The I_D/I_G ratio is used by many researchers to estimate defect content [82] and inter-defect distance in MWCNTs. The ratio indicates the overall graphitic nature of the nanocomposite MWCNTs. In a way it gives a measure of how the given carbon bond structure would deviate from the ideal graphite sp^2 hybrid structure. Pristine MWCNTs are commonly found to have more amorphous carbon and sp^2 hybridised carbons. This explains why iron catalysts are encapsulated in the tubes leading to a compromised crystalline structure of graphite. The R (I_D/I_G) ratio increases due to an increase in curvature as the diameter becomes smaller and defect sites increase. Smaller diameter MWCNTs have high sp^2 to sp^3 ratio and therefore R is higher than expected.[66] The full width at half maxima of a Raman line vibration indicates that the interactions between vibrations and integral of the Raman line is proportional to the number of excited vibrations states.[128] Li *et al.*[66] reported that as the number of acid treatment cycles increases defect sites increase but vacuum annealing at 1800 °C improves crystallinity and decreases local defect intensity. The $I_{G'}/I_G$ ratio is used as an indicator of long range order and the overall crystalline quality is deduced by the $I_{G'}/I_D$ ratio.[40] Stobinski *et al*.[129] observed that the lower the $I_{G'}/I_G$ ratio the better was the structural order. Bom *et al.*[122] observed that defects on MWCNTs caused a decrease in oxidation stability and that smaller diameters resulted in a high degree of curvature consequently leading to high reactivity towards oxygen. Scalese *et al.*[127] observed the radial breathing mode at 328 cm^{-1}. They also observed a peak at 2920 cm^{-1} that they assigned to C-H stretching for oxidised samples and a large G band shift ($>$ 14 cm^{-1}) due to change in electrochemical structure. According to a report by Sawatsuk *et al.* the G- and D-bands

were located at 1624 cm^{-1} and 1348 cm^{-1} respectively. The absence of a radial breathing mode and G-G' splitting were due to a weak signal of the large inner diameter of the tubes and some wider distribution range of MWCNT diameter.[48]

2.7.2.2 Raman spectroscopy in titania

Raman spectroscopy in titania provides valuable information about the polymorph present. The existence of any of the titania polymorph crystalline forms is an indication of crystallinity. Sawatsuk *et al.*[48] reported that the anatase phase of TiO_2 has peaks at ca. 395, 518 and 642 cm^{-1}.

From this brief survey it is clear that Raman spectroscopy is a vital tool in the characterisation of MWCNT-titania composites since the constituent ratios of the composites introduce varying effects on carbon bond length, strain and curvature. The next section looks at techniques used mainly for determining the morphology of the composites.

2.7.3 Scanning electron microscopy

Historically, the technique dates as early as 1933 with the first attempt by Ruska, which only managed ten times magnification. The instrument developed over decades through the surface topography breakthrough by Marl in 1941.[131] Knoll invented scanning electron microscopy (SEM) in the 1930s and thereafter progress was much faster culminating to the Jeol model developed in Japan.[131] SEM is a technique that produces three-dimensional images of a sample. It involves scanning of the surface of a sample with a focused beam of highly energetic electrons that generate a variety of signals at the surface.[132] Surface topography, crystalline structure, textural and chemical composition details result from the interactions of electrons and sample. **Figure 2.6** shows a diagram of the SEM instrument.

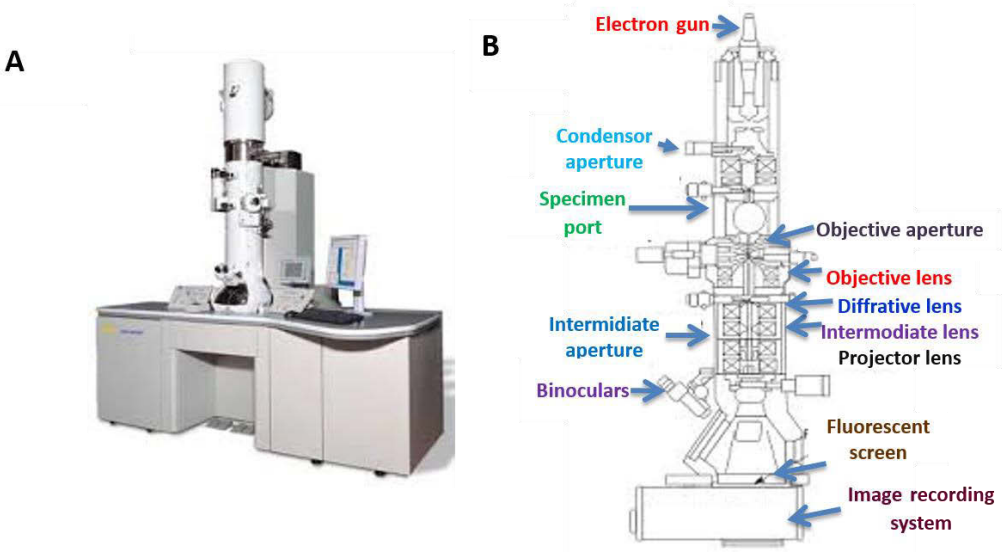

Figure 2.6: The scanning electron microscope: (**A**) instrument and (**B**) the enlarged parts

Accelerated electrons with high kinetic energy dissipate energy as variety signals during deceleration. Signals comprising of secondary electrons that give SEM images, back-scattered electrons, photons and continuum X-rays, visible light,[131] and diffracted back-scattered electrons are received by the detector and passed to the display. Photons play a role in elemental analysis and diffracted back-scattered electrons in determining mineral orientations. Field emission-scanning electron microscopy (FE-SEM) and SEM are used to study the morphology and dimensions of MWCNTs.[73,123]

In the works of Tessonnier *et al.*[133] varying magnifications in SEM were able to show both agglomeration of tubes and surface topography. The morphology of a nanotube is subject to the growth substrate.[133] For example, methane decomposition at 600 °C over nickel or aluminium catalysts produces bamboo shaped MWCNTs.[45] This means the source of MWCNTs used in nanocomposites ultimately has an effect on applications in light-harvesting. Both TiO_2 and TiO_2-MWCNT are reported to be spherical.[20] The oxide layer makes the MWCNT diameter appear larger than the actual.[82] Korbély *et al.*[134] observed that the majority of MWCNTs were covered with titania in their work using SEM. In their work, they were able to observe the variation in titania coat uniformity on changing solvents in the wet impregnation method. The information from SEM is vital because morphology and surface roughness can affect physical chemical properties. For example, thicker layers

can result in a larger band gap or longer distances for charge carriers to travel. Furthermore, new trap sites may form for carriers between the oxide and CNTs on coating MWCNTs. These effects are crucial in the ultimate electron transport in the MWCNT-titania nanocomposites. Maximum power conversion efficiency is a subject of nano-morphological arrangement and surface properties of the composite.[66,87,94] This is the reason why employing this technique in nanomaterials for light-harvesting is crucial. Furthermore, transmission electron microscopy (TEM) is important for almost the same reasons (see subsequent section).

2.7.4 Transmission electron microscopy

G.P. Thomson was the first to appreciate that if electrons are passed through a thin specimen, a transmission diffraction pattern forms.[135] Electrons are negatively charged and have a wave-like character. Therefore, electric magnetic fields deflect electrons. This was the foundation of TEM since transmitted electrons can be focused and have very short wavelength which allows imaging. Magnetic electron lenses are required for focusing the e^- beam onto the sample producing an enlarged image.[132] Modern TEMs use an accelerating voltage between 100 and 300 Kv because going beyond increases electron momentum, which decrease the de Broglie wavelength of electrons lowering the diffraction limit to spatial resolution. In TEM, an electron beam from the electron gun is passed into an ultra-thin sample.[135] The size and intensity of the beam are controlled. An image, which is magnified in the objective lens onto the CCD camera sensor, is produced. **Figure 2.7** shows a diagram of the TEM. The image is produced from the interaction of electrons and sample. In this technique, the side with nanoparticles should be facing down in the sample holder and high resolution images are possible due to the small de Broglie electron wavelength. The TiO_2 film thickness is a key factor that controls electron transfer.[66] TEM can be used to confirm the dispersion of dopants on the TiO_2 and microstructure.[20] TEM is used by many researchers to determine the structure and dimensions of MWCNT-based composites,[79] and hence the technique is crucial in the investigation of the structure and morphology of the proposed nanocomposites. Jitianu *et al*.[119] observed a homogeneous coverage of MWCNTs with a coat thickness of 3 to 5 nm (see **Figure 2.8**).

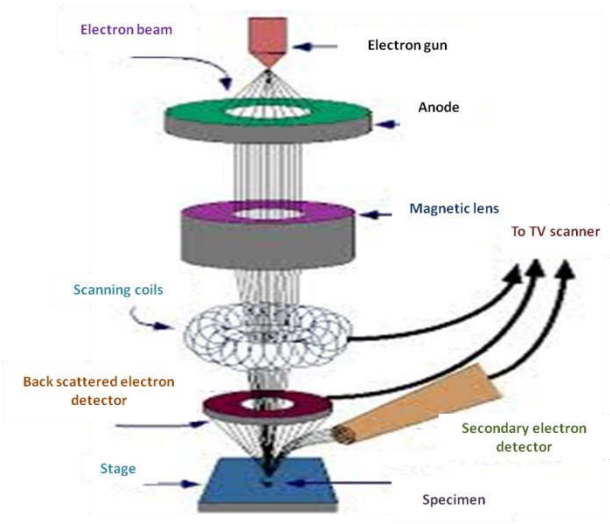

Figure 2.7: Diagram of a transmission electron microscopy instrument

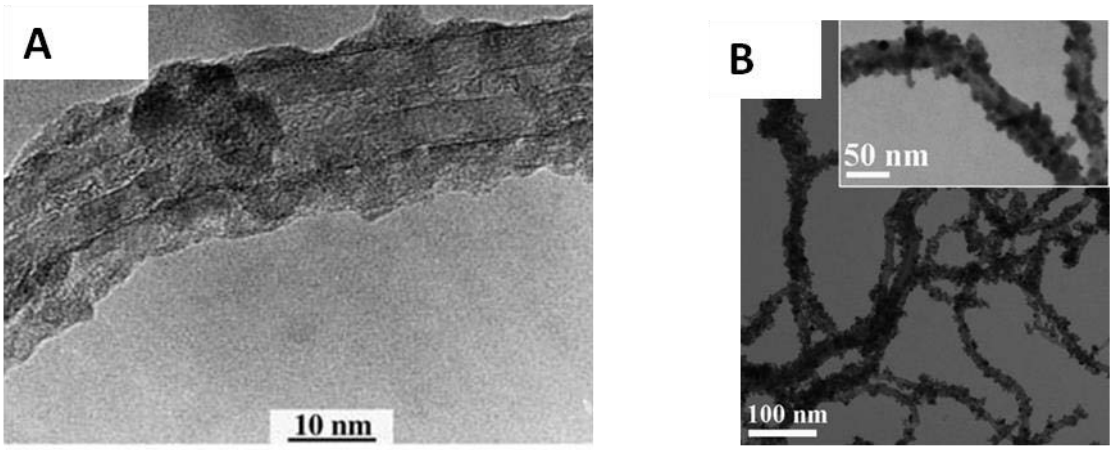

Figure 2.8: TEM images for MWCNT-titania nanocomposites reported by: (**A**) Jituanu *et al.*[119] and (**B**) Yan *et al.*[30]

In other similar work reported on MWCNT-titania nanocomposites Mokaya *et al.*[66] were able to determine the inner and outer diameters of the MWCNTs (10 - 30 nm) and that the titania film thickness on the MWCNTs was between 5 to 15 nm thick. This shows that their coat was thin since it was possible to see inside the tube by using TEM. Manchester *et al*.[136] in their works observed a uniform MWCNTs coverage of 5 nm to 10 nm in thickness. Titania particles were clearly attached on the MWCNTs but the film thickness was not reported by Boccaccini *et al.*[117] Casous *et al.*[118] observed agglomeration of titania in their

nanocomposites and they did not report film thickness. Amorphous titania agglomerates were not clearly observed by using TEM but the structure of the MWCNTs was roughened and most clusters were observed at open tube ends.[137] This could be explained by the fact that most carboxylic acid groups from acid treatment will be found at the tube ends.

2.7.5 Powder X-ray diffraction

This section presents some background details on X-ray diffraction (XRD) technique and linking it to materials for light-harvesting analysis.

Powder XRD (see **Figure 2.9A** and **B**) gives valuable information such as the dimensions of the elementary cell from the peak position, atom position, and crystal size from peak broadening, quantitative phase amount from the scaling factor, false order from diffuse background, and close order from modulated background.

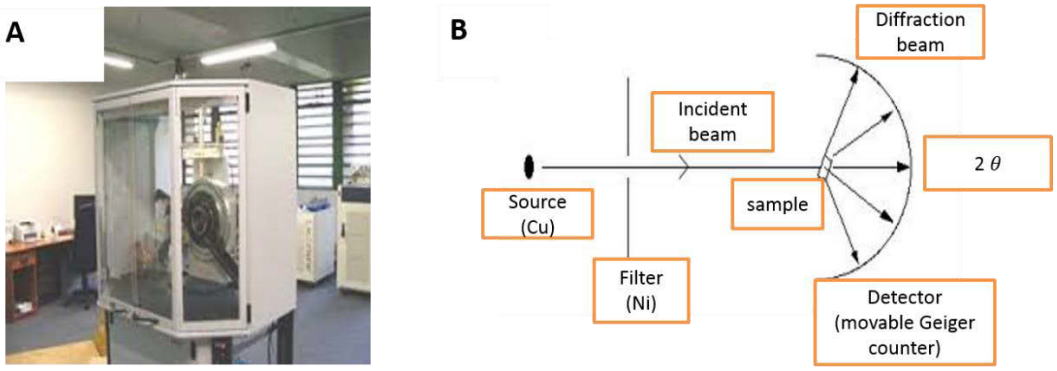

Figure 2.9: XRD instrument: (**A**) powder XRD instrument used in the current work and (**B**) schematic diagram of how the instrument operates

Figure 2.9B displays some important parts of the XRD instrument. An X-ray typically from a copper cathode ray tube passes through a nickel filter. The filter allows monochromatic radiation to pass through. It is thereafter, passed onto the sample in the sample holder. The detectors detect diffraction beams from the sample.[138]

Powder samples particularly nanocomposites give cones when high intensity scattered beam is used. Control of nano crystal shape is vital in solar cells[117] and hence XRD analysis is

helpful in this regard. Crystalline structures would imply large particle sizes and therefore a reduced number of boundaries, this minimises possible e^-/h^+ recombination centres at the nanoparticle boundaries. XRD identifies changes in the MWCNTs on purification and functionalization in terms of crystallinity. The subsequent paragraph highlights some literature cases that support the importance of this technique. Some experimental procedures such as calcining may introduce phase changes and XRD is vital in monitoring these changes. The coating of carbon with titania has been reported to prevent titania phase change.[79] Metals can catalyse the anatase-rutile transformation[72] which causes low efficiency in PV. For example, according to X-ray patterns by Mian-liang *et al.*[73] the anatase phase below 500 °C transforms to the rutile phase above 600 °C (700-900 °C) but on annealing both phases are present at 700 °C. This makes it necessary to investigate the titanium dioxide crystal phase by XRD[73,79,123] in solar cells. The technique allows one to estimate the titania phase ratios. However, most material scientists report that peaks due to MWCNTs in MWCNT-titania nanocomposites are difficult to locate due to overlap with TiO_2 peaks (see **Table 2.6**). Cong *et al.*[73] reported the graphite d-spacing to be similar to that of TiO_2 (0.34 nm and 0.35 nm respectively). **Table 2.6** gives some of the reported peaks of MWCNT-titania nanocomposites.

Table 2.6: Some reported peaks of TiO_2 and MWCNTs in MWCNT-titania nanocomposites

Peak:2θ	Miller indices (h k l)	Comments		Ref
25.28	(101)	Anatase phase of TiO_2		95
37.80	(004)			
48.18	(200)			
54.09	(105)			
26.40	-	MWCNT		20
26.3	(002)	Intense and sharp peak of MWCNTs		
42.8	(100)	MWCNTs reflection peaks		73
44.5	(101)			
54.2	(004)			
25.3	(101)	The peak is due to TiO_2 and MWCNTs		
37.8	(004)	TiO_2 anatase peaks are intensified when oxidation temperature is 300 °C		
48	(200)			
53.9	(211)			
62.7	(204)			
26	-	anatase	Peaks used to identify changes during purification and functionalization. Peaks are narrower and symmetrical on removal of amorphous carbon	115
33	-	brookite		
27	-	rutile		
25.28	(101)	Anatase phase of TiO_2. Peak at 25.2 overlaps with MWCNTs peak.		123
37.8	(004)			
47.9	(200)			
54	(105)			
62.6	(204)			
25.9	-	MWCNT peak overlaps with TiO_2		
43.2	-	MWCNTs		

2.7.6 Inductively coupled plasma-optical emission spectroscopy

ICP-OES is an analytical technique that determines the elemental composition and concentrations present in nanocomposites in a precise way. This method uses highly energised plasma from a noble gas such as He or Ar to excite an element. The emitted photons are characteristic of the metal present and the intensity of the spectral signal is subject to the amount present. The wavelength of light emitted is influenced by energy difference between the ground and excited state. This energy difference is characteristic of the element. Nanoparticles need to be digested, the ions atomised and vaporised in the plasma. Ideally, nano-pure water should be used as solvent since double deionised water has some metals. Elements with similar atomic structure will have emissions with similar wavelength causing interference.

Recent technological advances have led to the realisation that ICP-MS can be used for the determination of nanoparticle sizes, in this manipulation, very dilute solutions are used and one particle per droplet is delivered in the nebuliser. However, this could not be done in this work because the ICP was not of the correct configuration required.

The technique determines the titanium content of the TiO_2/MWCNT composites, by using a suitable digestion method. Similar approaches are reported for metal determination in food samples, this is briefly discussed below. The analytical technique requires digestion followed by dissolution in aqueous media before analysis. Anatase and rutile phases of titania are insoluble at ambient pH.[140] Methods available for metal digestion are hot plate, microwave and alkaline fusion. Microwave-assisted digestion and hot plate methods have been reported by some researchers mainly for solid samples.[139] Microwave digestion usually gives better reproducibility. Various acid combinations have been used for metal digestion. However, our survey on titania digestion points out that HF[141] or concentrated H_2SO_4 are typically used to dissolve TiO_2. Sulfuric acid is most preferred due to its relatively satisfactory recoveries, health and safety attributes. HF aids in the solubilisation of titania, but has several health and safety risks associated with its use. Nitric and sulfuric acids combinations were used in food samples for ICP-OES.

2.7.7 Textural characteristics

Lastly, other important parameters in nanocomposites are the pore volume and surface area since surface area and porosity are linked to physicochemical properties (see **Table 2.7**). Surface area is the total sum of the surface areas of individual particulates constituting the material.[142] Surface area is important for adsorption of the dye and a general expectation will be an increase in chemical reactions in nanomaterials with an increase in surface area. Therefore, investigating the available surface area in synthesised nanocomposites is vital. Furthermore, pore volume defined as the size of empty spaces in a material is equally important. Heat treatments may influence surface area. Textural characteristics have a role in light-harvesting since they influence the amount of dye adsorbed on the nanocomposite. In this technique, samples were out-gassed and nitrogen gas adsorption was used for the study. Jitianu *et al.*[119] out-gassed samples at 150 °C for 12 hours and the final pressure was 10^{-6} mbars. They deduced that the amount of titania deposited on MWCNTs is subject to the precursor and deposition method. An increase in the titania layer causes a decrease in the specific and micro pore volume due to blockage of the micro pores of MWCNTs. Type IV isotherm mesoporous character was preserved in their work.[102,119] Such reports from literature implies that textural characteristics cannot be ignored for mesoporous composites particularly MWCNT support materials.

Table 2.7: Surface areas and pore volumes of some MWCNT-titania nanocomposites

Sample	S_{BET} (m^2/g)	V^a (cm^3/g)	References
MWCNTs	300	0.13	119
MWCNTs	187	0.07	
CNTs	264.08	2.419	102
Pure titania	196.72	0.136	
CNTs/titania (10% Ti)	230.23	0.337	

Characterisation of nanomaterials is vital because their properties influence their performance in various applications. For example, in DSSC applications, surface area and porosity play a key role in dye adsorption. The subsequent section reviews the concept of PVs and some key parameters important in this field.

2.8 Dye-sensitised solar cells

Alexandra-Edmond Becquerel first observed the photovoltaic effect in 1839. The photovoltaic effect states that when a photon is directed on a region close to a p-n junction built barrier, an electric potential is generated.[143] The photovoltaic effect involves a self-generated electromotive force (emf), generation of electron hole pairs under optical excitation, collection of charge at a counter electrode and finally the ability to deliver power to an external load.

Other well-known energy technologies such as wind offer competition to PV technology. Various researchers in the India Brazil South Africa (IBSA) energy initiation project are working towards that goal. Silicon solar cells currently dominate the PV market due to high power conversion efficiencies of up to 25%. Titanium-based solar cells have the potential to challenge silicon-based solar cells in terms of cost. Methods of depositing titania on ITO glass substrates include low temperature heating, microwave irradiation, hydrothermal crystallisation and CVD. The easiest method for depositing titania on ITO coated glass is doctor blading. The doctor blading method is a compatible technique used to coat a material on a substrate involving roll to roll active layer deposition.[144] Glass solar cells are rigid and annealing is usually in the range between 400 and 450 °C. Such PV cells have achieved conversion efficiencies of $\pm$4 %.[145] Titanium nanocomposite-based solar cells have the potential to bring about a competitive product since silicon solar cells are expensive.[18,145,146] However, applications of titania towards this goal have been limited by the band gap of titania in utilising the visible region of the solar spectrum as discussed in **section 2.5.4**. Some of the approaches to counteract this effect are to use quantum dots (QDs) and dyes as sensitizers**.**

QDs employ the multi-exciton generation phenomenon.[94] An investigation of QD integration in PVs might possibly contribute something positive to the efficiency of titania-based solar cells. Integration of QDs nanocrystaline material opens the possibility to develop low cost solid-state solar cells. The absorption of QDs depends on composition and this offers an advantage of being able to fine tune the absorption properties of the sensitizer. QDs allow energy level matching between donor and acceptor and this contributes greatly to efficiency of a PV. QDs have three-dimensional quantum confinements, which induce discretization of electronic states. QDs containing a nanocomposites coating are an alternative for the fabrication of planar QDs concentrators. The advantage of quantum dots over dye molecules includes the tunability of the optical properties with size and better hetero-junction formation with solid hole conduction.[63] However, new generation solar cells also include dye-sensitized semi-conductors and organic hetero-junction films organic-inorganic hybrid structure based PV materials.

Gerischer and co-workers were one of the pioneers of DSSCs in the 1960s and they used semi-conductors and organic sensitizers. Gratzel invented efficient and low fabrication cost DSSCs in 1991. Initial conversion efficiency was 11.1%.[48,95] The highest recorded efficiency is 12%.[95] A major area of study since then is still on the efficient transfer of electrons across a nanometre particle interface. The drive is to couple high efficiency and low cost in addition to easy scalability to vast areas. Electron conversion efficiency (ECE) is important for commercialisation of DSSCs[147] and this phenomenon is influenced by the semi-conductor oxide layer. ECE is discussed in detail in **section 2.8.7**. Several semi-conductor oxide layers tried in DSSCs include SnO_2, WO_3, $SrTiO_3$, CeO_2, $ZnSnO_4$ and FeS. Oxygen deficiency induces visible light absorption.[146] Efficiencies of greater than 8% have been reported in recent reports.[148] Plastic-based DSSCs have achieved power conversion efficiencies of 6.4%.[145] DSSCs-based on composites from a simple direct mixing method are reported to have achieved a conversion two times efficiency improvement.[48,95] A longer electron diffusion length might promote recombination.[147] A 2 μm thickness of 0.2 wt.% CNTs on TiO_2 achieved an increase in energy conversion of 1.51%, J_{sc} increase of 3.58 mA cm^{-2} , V_{oc} increase of 0.05% and FF increase of 0.02.[37] DSSCs from MWCNT-TiO_2 via sol-gel synthesis achieved a conversion efficiency of 4.97%.[149]

A redox mediator such as I^-_3 redox couple diffuses to the counter electrode where it is reduced. The oxidized form of a sensitizer accepts an e^- from the reduced mediator. The counter electrode controls the regeneration of oxide mediator into the reduced form and must have low charge resistance. A Pt counter electrode and I^-/I_3^- system may be used since Pt is stable and able to catalyse I_3^- reduction.[36,94] However, the iodine concentration has been reported to have an influence on the performance of PVs because it absorbs strongly at 430 nm (see **Table 2.8**).[150] The iodine concentration needs optimisation since a decrease in concentration leads to a high transmittance but values that are too low might fail to regenerate the ground state of the sensitizer (see **Table 2.8**). Electrolyte leakage remains a set-back in DSSCs and expensive conductive material. Although we focus more on the active area, ionic, quasi-solid and solid electrolytes such as CuI and CuSCN have been reported in literature but the efficiency is still very low.[150]

Table 2.8: Effect of iodine concentration on PV performance

Iodine concentration /M	V_{oc} /V	J_{SH} /mA cm^{-1}	FF	n /%
0.01	0.720	4.12	0.709	2.11
0.02	0.692	6.01	0.720	3.00
0.05	0.687	5.41	0.738	2.75
0.08	0.692	3.08	0.774	1.01

Advantages of polymer gel electrolytes, such as polyvinyl acetate as gelator, include lower leakage, lower volatilisation, excellent interfacial contact, higher ionic conductivity and high long term stability. Recombination of photo-injected electrons with electrolyte (I_3^-) decreases V_{OC} and several ways for inhibition include blocking with metal oxide layers or composite oxide films, attaching hydrophobic chains to the pyridine rings and treating dye coated TiO_2 films with pyridine derivatives.[151] Pyridine rings are able to form bonds with the metal oxides. Fu *et al.*[36] suggested fibber (pear) shaped DSSCs to prevent present electrolyte problems. Pt is expensive and using it will lead to expensive PVs, so we will propose trying other cheap counter electrodes.[42,87] Wright and Uddin used aluminium as a

counter electrode. Zhu *et al.*[42] reported that MWCNTs are better than other carbon counter electrodes. We also propose that CNTs be used as counter electrodes since they might also enhance efficiency by nanoscale conduction, light weight and high flexibility.[42] The power gained is due to the photons gained by the sensitizer. TiO_2/MWCNTs inhibit recombination of photo-induced carriers.[66,73]

Many researchers reported ruthenium complex dye-sensitized semiconductor solar cells using mainly TiO_2 as semiconductor.[19,79,89,151-155] These well researched dyes can be used as standards for new dye trials. A photo-excited dye transfers electrons to the nanotube to generate a positively charged dye and negatively charged nanotube.[101] In summary, electrons move from the HOMO into the LUMO of the sensitizer (dye) on excitation, then to the conduction band of MWCNT-TiO_2[152] and *via* the external circuit through the load to the counter electrode before being picked by the redox mediator and finally back to the sensitizer (see **Figure 2.3** in **section 2.5.3**).

2.8.1 Indium tin oxide

Indium tin oxide (ITO) coated glass allows light to pass through and collects holes from the device. The ITO glass is part of the photoanode side in a DSSC. A conductive polymer mixture (PEDOT-PSS) may be applied between the anode and the photoactive layer to block excitons, transport holes, to make ITO glass smooth, and prevent oxidation and allows the cathode to protrude into the active layer.[87]

2.8.2 N3 dye standard

Dyes are sensitizers in DSSCs and properties of an ideal dye are given in **Chapter Five**. Reports of a number of different dyes in DSSCs applications exist and most of them are ruthenium-based complexes (see **Table 2.9**). In this section a brief insight of the N3 dye application as a standard in DSSCs is given. The N3 dye can be used in trials of some natural dyes in solar cells[89] since the dye is amongst well documented dyes in literature.

Table 2.9: Some reported dyes applied in DSSCs

Dye	References
ruthenium 535-bis-tetrabutylammonium	99
cis-bis(2,2'-bipyridyl-4.4'-dicarboxylato)-ruthenium(II)-bis-tetrabutylammonium	82
N3	153
eosin Y	89
ruthenium (bipyridyl-4,4'-dicarboxylic acid)$_2$(NCS)$_2$.2H$_2$O	95
ruthenium (II) (2,2'-bipyridyl-4,4'-dicarboxylate)(NCS):2 tetrabutylammonium	48
cis-dithiocynate-N,N-bis(4-carboxylate-4-tetrabutylammonium carboxylate-2.2'-bipyridine) ruthenium(II)	39

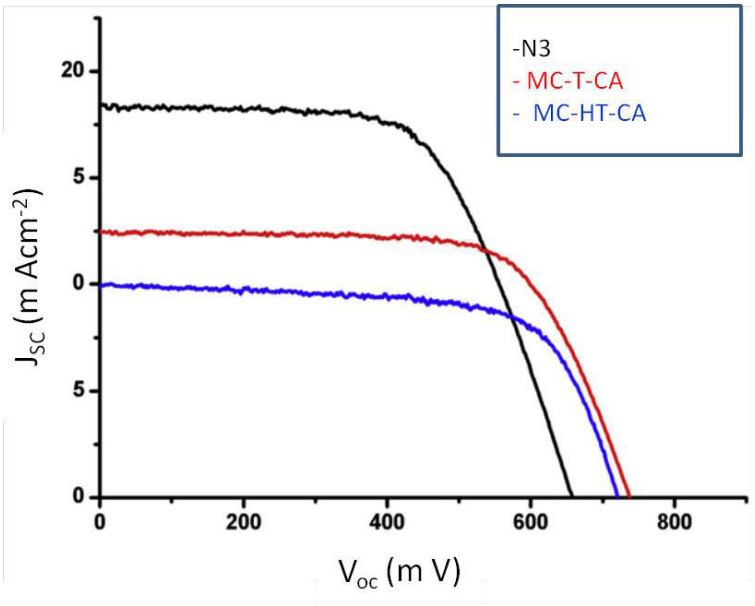

Figure 2.10: Typical current density-voltage curve for N3 dye in TiO_2-based solar cell[155]

The **Table 2.10** and **Figure 2.10** show some of reported performance characteristics of N3 dye.[151] The last section of the review discusses important parameters that characterise PV quality.

Table 2.10: Performances of some reported N3 dye-sensitised titania-based solar cells

V_{OC} /V	J_{SC} /m Acm^{-2}	n /%	FF	References
0.690	14.60	5.70	0.570	[151]
0.688	1.53	2.37	0.670	[89]
0.680	10.55	4.00	0.560	[152]
0.656	18.33	7.49	0.620	[155]
0.639	17.86	6.12	0.537	[153]
0.653	12.00	4.80	0.610	[154]

2.8.3 Performance characteristics

Current-voltage graphs are important tools for measuring performance (see **Figure 2.10**). Defects and dipoles at the interface, energy barriers and a low surface recombination rate at the photocathode can cause an S-kink in current-voltage graphs, i.e. S-shaped current-voltage graphs. An S-kink in a DSSC is mainly caused by two effects: a mobility imbalance between e^-/h^+ causing the creation of an additional E-field thereby reducing efficiency and Fill factor (FF is discussed in **section 2.8.10**) and secondly, an adverse barrier as contact resistance.[156] Air mass (AM) is the standard terrestrial solar spectral irradiance distribution.[72] AM is important in standardising DSSCs because the temperature and water vapour in the atmosphere will affect the performances of devices differently depending on location. This means V_{oc}, J_{sc}, FF and efficiency are subject to AM. Valid international standards are AM = 1.5 G, light intensity 1000 W cm^{-1} or 100 m W cm^{-1} and cell temperature at 25 °C.[87,89,152-155]

2.8.4 External quantum efficiency

External quantum efficiency (EQE) is the ratio of photo-generated electrons collected to the number of incident photons at a specific wavelength. Incident photon-to-current efficiency (IPCE) is the same as EQE. ICPE is calculated from the short circuit photocurrent, intensity of incident light and wavelength. It is defined by the number of generated electrons per number of incident photons.[145]

$$\text{EQE} = \frac{\text{number of e}^- \text{ hole pairs generated/area}}{\text{number of photons striking device/area}} \quad \textbf{(equation 2.3)}^{143}$$

2.8.5 Fermi level

Fermi level (E_f) is the average energy of the charge carriers i.e. energy of the p- and n-junctions in a device. Thus, V_{OC} is the energy required to add an electron into the p-junction from the n-junction (see **Figure 2.11** and **section 2.8.6**). The high the V_{OC} between interfaces of DSSCs the greater the ability to transport an e^- across the interfaces.

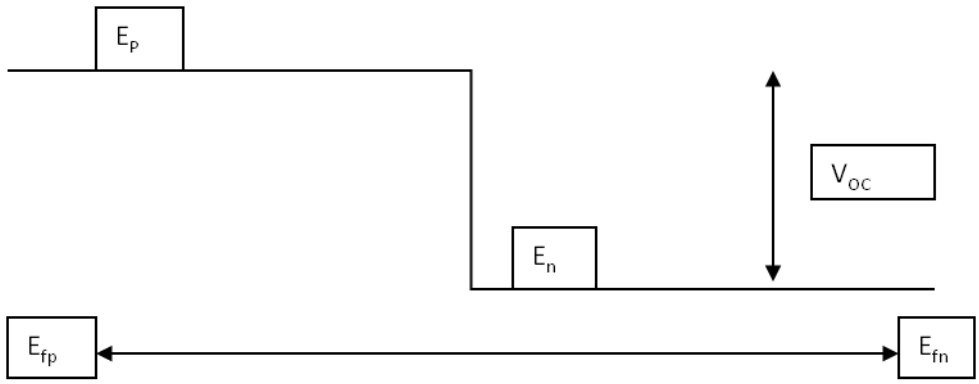

Figure 2.11: A schematic diagram showing the relationship between potential energy (voltage) and Fermi level[143]

2.8.6 Open circuit voltage

Open circuit voltage (V_{OC}) is the difference of electrical potential between two terminals of an illuminated PV with no external load connected. Brabec *et al.*[87] reported that V_{OC} is weakly influenced by type of metal counter electrode used.[87,89,94,152-155]

From **Figure 2.11**, $V_{OC} = E_{fp} - E_{fn}$ (**equation 2.4**)

where E_{fp} and E_{fn} are Fermi energy levels for the p and n junction respectively.[143]

Major limitations of efficiency are in two main groups:

1. Recombination due to diffusion time through TiO_2
    - ✓ dye recaptures an electron
    - ✓ electrolyte (I_3^-) recaptures an electron
2. Rate of ion transport from counter electrode to dye and this more pronounced at high electrolyte concentrations causing V_{OC}, J_{SH} and FF to decrease.[147,154]

2.8.7 Short circuit current

A short circuit is an electrical circuit (I_{SC}) that allows current to pass through an unintended path. I_{SC} is the highest current passing through an illuminated PV with no external load under short circuit conditions.[87,94] I_{SC} is proportional to the light intensity and device area.[143] High electron mobility is good for exciton dissociation and carrier transport but recombination is enhanced.[156]

2.8.8 Short circuit current density

Short circuit current density (J_{SC}) is the maximum photocurrent density which can be extracted from the device under short circuit conditions. Generation of photocurrent is in the near infrared (NIR) and this reduces the heating effect while increasing shunt resistance (R_{SH}).[87]

2.8.9 Resistance

Series resistance (R_S) is influenced by poor conductivity and the charge carrier imperfection. R_S is derived from bulk resistances between the active layer and electrodes, while R_{SH} is from current leakage from the edge of the cell. R_S determines the current flow direction between diode and external load. The ideal R_s is 0 and the ideal shunt resistance, R_{SH} is infinity. If R_{SH} is infinity then there is no current leakage in the device by the traps. R_{SH} and J_{sc} decreases if transit time is larger than lifetime of carriers. Annealing improve interfacial morphology and decrease surface recombination and leakage.[156] However, imperfections within photoactive film or current leakage reduce R_s.[87,89,143,152-155]

2.8.10 Fill factor

The shape of a device's I-V curve is a true indication of the device performance efficiency. This is the largest rectangle under the J-V curve. Fill factor (FF) is the ratio of the maximum obtainable power i.e. P_{max} to the product of V_{OC} and J_{SC}.[143] It measures the squareness of the J-V curve.[157] The more rectangular the J-V curve the better the FF and the higher the efficiency. The quality of the diode is affected by physical constraints when $FF < 1$ and varies mostly between 0.3 and 0.8 in real diodes. Real diodes deviate from the ideal due to recombination.

$$FF = \frac{V_{max} \times J_{max}}{J_{sc} \times V_{oc}} \qquad \textbf{(equation 2.5)}$$

For an ideal diode PV, $J_{sc} = J_{max}$ and $V_{oc} = V_{max}$. This implies that $FF = 1$ and shape J-V is a perfect rectangle (see **Figure 2.12**). Theoretical FF is given by

$$FF = \frac{dP_{max}}{dV} = \frac{dIV}{dV} = 0 \qquad \textbf{(equation 2.6)}$$

$$V_{max} = V_{oc} - \frac{nKT}{q} In\left(\frac{V_{mp}}{nKT \backslash q} + 1\right) \qquad \textbf{(equation 2.7)}$$

$$FF = \frac{V_{OC} - In(V_{OC} + 0.72)}{V_{OC} + 1} \qquad \textbf{(equation 2.8)}$$

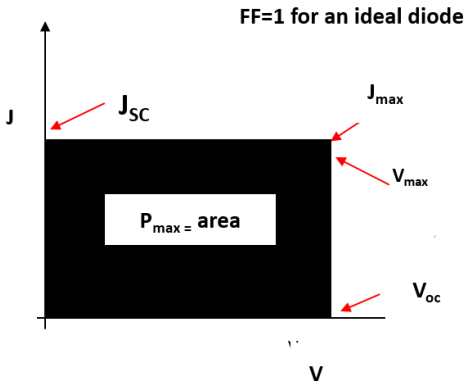

Figure 2.12: The J-V curve for an ideal diode.[87,89,152-155,157]

2.8.11 Power conversion efficiency

Power conversion efficiency (n) is the ratio between the maximum electrical power and incident electrical power (P_{IN})

$$n = \frac{\text{Maximum power output}}{\text{Incident intensity} \times \text{Area of device}} \qquad \textbf{(equation 2.9)}$$

$$= \frac{V_{max} I_{max}}{\text{Insolation} \times \text{Area}}$$

$$= \frac{V_{max} I_{max}}{P_{IN}}$$

$$= \frac{FF \times I_{SC} \times V_{OC}}{\text{Total insolation}} \quad [94,143]$$

Also total efficiency can be expressed in a different way according interface processes from light absorption to charge collection,

$$n_T = n_A \, n_{ED} n_{CT} n_{CC} \qquad \textbf{(equation 2.10)}$$

where n_A, n_{ED}, n_{CT} and n_{CC} are absorption efficiency, exciton dissociation efficiency, charge transfer efficiency and charge carrier collection efficiency respectively.[156]

Effects of J-V characteristics in PV are:

- Sunlight intensity
- Cell operating temperature

- Prevailing wind velocity of site[143]

The ideality factor (n) is the measure of the junction quality and type of recombination in solar cells. Ideality factor is one - only if the diffusion current flows into the junction and two - if recombination is predominantly occurring. Interaction of R_S, R_{SH} and diode influences current flow in a device.[156] In practice, FF is lowered by parasitic resistive losses. Resistive effects in solar cells decrease efficiency by dissipating power in the resistances.[157]

References

1. J. P. Tricoire and V. Denner, *International Energy*, 2013, **4**, 1-48.
2. R. Albertyn, H. Rode, A. J. W. Millar and M. D. Peck, *Burns*, 2012, **38**, 790-795.
3. L. Suganthia and A. A. Samuel, *Renewable and Sustainable Energy Reviews,* 2012, **16**, 1223-1240.
4. N. S. Lewis and D. G. Nocera, *Proceedings of the National Academy of Sciences of the United States of America,* 2006, **103**, 15729-15735.
5. M. Z. Jacobson, *Energy & Environmental Science*, 2009, **2**, 148-173.
6. N. Y. Mansouri, R. J. Crookes and T. Korakianitis, *Energy Policy*, 2013, **63**, 681-695.
7. B. Parida, S. Iniyan and R. Goic, *Renewable and Sustainable Energy Reviews*, 2011, **15**, 1625-1636.
8. P. Kirai and M. Hankins, *East African Community (EAC)*, Arusha, Tanzania, 2009, pp. 1-44.
9. A. Marquard and H. Winkler, *Energy Research Centre*, 2010, **10**, 5818-5828.
10. H. Scheer, *Solar Energy Materials and Solar Cells*, 1995, **38**, 555-568.
11. P. Bellaby, *Energy Policy*, 2010, **38**, 2624-2630.
12. R. Saidur, M. R. Islam, N. A. Rahim and K. H. Solangi, *Renewable and Sustainable Energy Reviews*, 2010, **14**, 1744-1762.
13. K. Gillingham, R. G. Newell and K. Palmer, *Nber*, 2009, **1**, 597-620.
14. S. Jebaraj and S. Iniyan, *Renewable and Sustainable Energy Reviews*, 2006, **10**, 281-311.
15. N. R. Moheimani and D. Parlevliet, *Renewable and Sustainable Energy Reviews*, 2013, **27**, 494-504.
16. C. L. Kwaan and A. Hoffman, *Butterworth-Heineman*, 2010, pp. 181-215.
17. B. Johansson, *Energy,* 2013, **56**, 5987-608.

18. N. Selvakumar and H. C. Barshilia, *Solar Energy Materials and Solar Cells*, 2012, **98**, 1-23.

19. J. Schabauer, C. P. Morley, J. Baker, N. Dartnell, P. Douglas and C. Winscom, *Taylor and Francis*, 2007, **37**, 347-351.

20. G. An, W. Ma, Z. Sun, Z. Liu, B. Han, S. Miao, Z. Miao and K. Ding, *Carbon*, 2007, **45**, 1795-1801.

21. A. Aqel, K. M. M. A. El-Nour, R. A. A. Ammar and A. Al-Warthan, *Arabian Journal of Chemistry*, 2012, **5**, 1-23.

22. D. N. Arul, H. Cohen and A. Gedoken, *Physical Chemistry:B*, 1997, **101**, 6834-6838.

23. M. Terrones, A. Jorio, M. Endo, A. M. Rao, Y. A. Kim, T. Hayashi, H. Terrones, J. C. Charlier, G. Dresselhaus and M. S. Dresselhaus, *Materials Today*, 2004, **7**, 30-45.

24. N. Islam and K. Miyazaki, *Technological Forecasting and Social Change*, 2009, **76**, 128-140.

25. http://www.nano.gov/nanotech-101/what/definition, Accessed 5 December, 2013.

26. M. F. Hochella, *Earth and Planetary Science Letters*, 2002, **203**, 593-605.

27. http://www.nano.org.uk/what-is-nanotechnology, Accessed 5 December, 2013.

28. http://www.crnano.org/whatis.htm, Accessed 5 December, 2013.

29. http://www.nanowerk.com/nanotechnology/introduction/ introduction to nanotechnology 1.php, Accessed 5 December, 2013.

30. Y. Yan, J. Lu, C. Deng and X. Zhang, *Talanta*, 2013, **107**, 30-35.

31. C. Brough and R. O. Williams, *International Journal of Pharmaceutics*, 2013, **453**, 157-166.

32. O. Moldovan, A. Lázaro, F. Danneville, R. Picos, B. Nae, B. Iniguez and M. J. Deen, *Advances in Imaging and Electron Physics*, 2012, **174**, pp. 261-347.

33. E. Rafiee and S. Shahebrahimi, *Chinese Journal of Catalysis*, 2012, **33**, 1326-1333.

34. N. A. Dhas, H. Cohen and A. Gedanken, *Physical Chemistry: B*, 1997, **101**, 6834-6838.

35. X. Ma, X. Li, N. Lun and S. Wen, *Materials Chemistry and Physics*, 2006, **97**, 351-356.

36. Y. Fu, Z. Lv, H. Wu, S. Hou, X. Cai, D. Wang and D. Zou, *Solar Energy Materials and Solar Cells*, 2012, **102**, 212-219.

37. S. Campidelli, C. Klamp, A. Bianco, P. M. Guldi and M. Prato, *Physical Organic Chemistry*, 2006, **8-9**, 531-539.

38. A. Saraiya, P. Powal, A. W. Bajpai, N. K. Tripath and K. Ram, *Taylor and Francis*, 2006, **36**, 163-164.

39. A. de Morais, L. M. D. Loiola, J. E. Benedetti, A. S. Gonçalves, C. A. O. Avellaneda, J. H. Clerici, M. A. Cotta and A. F. Nogueira, *Photochemistry and Photobiology A: Chemistry*, 2013, **251**, 78-84.

40. S. Santangelo, M. Dhanagopal, G. Faggio, G. Messina, A. Pistone, M. Lanza and C. Milone, *Diamond and Related Materials*, 2010, **19**, 599-603.

41. S. Meagan, M. Elimelech and M. Elimelech, *Environmental Science and Technology*, 2008, **42**, 5843-5859.

42. H. Zhu, J. Wei, K. Wang and D. Wu, *Solar Energy Materials and Solar Cells*, 2009, **93**, 1461-1470.

43. J. H. Jung, S. Vadahanambi and I. K. Oh, *Composites Science and Technology*, 2010, **70**, 584-592.

44. M. L. Cohen, *Materials Science and Engineering: C*, 2001, **15**, 1-11.

45. N. Roy, R. Sengupta and A. K. Bhowmick, *Progress in Polymer Science*, 2012, **37**, 781-819.

46. J.-P. Salvetat-Delmotte and A. Rubio, *Carbon*, 2002, **40**, 1729-1734.

47. J.-P. Tessonnier, D. Rosenthal, T. W. Hansen, C. Hess, M. E. Schuster, R. Blume, F. Girgsdies, N. Pfänder, O. Timpe, D. S. Su and R. Schlögl, *Carbon*, 2009, **47**, 1779-1798.

48. T. Sawatsuk, A. Chindaduang, C. Sae-kung, S. Pratontep and G. Tumcharern, *Diamond and Related Materials*, 2009, **18**, 524-527.

49. R. A. Hatton , P. N. Blanchard , V. Stolajan , A. T. Miller and S. R. P. Silva, *Langmuir*, 2007, **23**, 6424-6430.

50. D. He, Y. Peng, H. Yang, D. Ma, Y. Wang, K. Chen, P. Chen and J. Shi, *Dyes and Pigments*, 2013, **99**, 395-401.

51. S. Jalili and M. Jamali, *Chemical Physics*, 2012, **402**, 91-95.

52. P. A. Jelliss, S. S. Graham, A. Josipovic, S. Boyko, S. D. Minteer and V. Svoboda, *Polyhedron*, 2013, **50**, 36-44.

53. M. Salerno, P. Landoni and R. Verganti, *Technological Forecasting and Social Change*, 2008, **75**, 1202-1223.

54. H. Ding, T. Feng, Z. Zhang, K. Wang, M. Qian, Y. Chen and Z. Sun, *Applied Surface Science*, 2010, **256**, 6596-6600.

55. S. Benguediab, A. Tounsi, M. Zidour and A. Semmah, *Composites Part B: Engineering*, 2014, **57**, 21-24.

56. M. Abdali and S. Mirzakuchaki, *Materials Science in Semiconductor Processing*, 2014, **17**, 222-227.

57. Y. Li, K. Wang, J. Wei, Z. Gu, Z. Wang, J. Luo and D. Wu, *Carbon*, 2005, **43**, 31-35.

58. H. Wu, D. Wexler, A. R. Ranjbartoreh, H. Liu and G. Wang, *International Journal of Hydrogen Energy*, 2010, **35**, 6345-6349.

59. W. Tang, M. H. Santare and S. G. Advani, *Carbon*, 2003, **41**, 2779-2785.

60. V. N. Popov, *Materials Science and Engineering: R: Reports*, 2004, **43**, 61-102.

61. J. Robertson, *Materials Today*, 2004, **7**, 46-52.

62. R. Enomoto, K. Horiuchi, K. Miyamoto, Y. Matsunaga, N. Aoki and Y. Ochiai, *Physica B: Condensed Matter*, 2002, **323**, 249-251.

63. A. Schüler, M. Python, M. V. del Olmo and E. de Chambrier, *Solar Energy*, 2007, **81**, 1159-1165.

64. L. Fan, C. Wang and B. Zhu, *Nano Energy*, 2012, **1**, 631-639.

65. S. Osswald, M. Havel and Y. Gogotsi, *Raman spectroscopy*, 2007, **38**, 728-736.

66. Z. Li, B. Gao, G. Z. Chen, R. Mokaya, S. Sotiropoulos and G. Li Puma, *Applied Catalysis B: Environmental*, 2011, **110**, 50-57.

67. G. Fang, W. Gao, Q. Deng, K. Qian, H. Han and S. Wang, *Analytical Biochemistry*, 2012, **423**, 210-217.

68. A. Villa, M. Plebani, M. Schiavoni, C. Milone, E. Piperopoulos, S. Galvagno and L. Prati, *Catalysis Today*, 2012, **186**, 76-82.

69. M. A. Grado-Caffaro and M. Grado-Caffaro, *Physica A: Statistical Mechanics and its Applications*, 2008, **387**, 445-448.

70. K. Ahmad and W. Pan, *Composites Science and Technology*, 2009, **69**, 1016-1021.

71. A. V. Ellis and B. Ingham, *Magnetism and Magnetic Materials*, 2006, **302**, 378-381.

72. H. Bing-shun , C. Feng-yim and M. Y. Wey, *International Journal of Hydrogen Energy,* 2010, **12**, 2503-2510.

73. Y. Cong, X. Li, Y. Qin, Z. Dong, G. Yuan, Z. Cui and X. Lai, *Applied Catalysis B: Environmental*, 2011, **107**, 128-134.

74. Y. Su, Z. Yang, H. Wei, E. S. W. Kong and Y. Zhang, *Applied Surface Science*, 2011, **257**, 3123-3127.

75. S. Santangelo, M. Lanza, E. Piperopoulos, S. Galvagno and C. Milone, *Materials Research Bulletin*, 2012, **47**, 595-601.

76. N. M. Mubarak, E. C. Abdullah, N. S. Jayakumar and J. N. Sahu, *Industrial and Engineering Chemistry,* 2013.

77. B. Fiedler, F. H. Gojny, M. H. G. Wichmann, M. C. M. Nolte and K. Schulte, *Composites Science and Technology*, 2006, **66**, 3115-3125.

78. J. H. Lehman, M. Terrones, E. Mansfield, K. E. Hurst and V. Meunier, *Carbon*, 2011, **49**, 2581-2602.

79. M. l. Chen, F. J. Zhang and W. C. Oh, *New Carbon Materials*, 2009, **24**, 159-166.

80. B. Fei , L. Haifeng, Z. Hu and J. H. Xim, *Nanotechnology*, 2006, **17**, 1589-1593.

81. L. Chan, Y. Zhai , H. Ding , G. Zhou, Y. Zhu and D. Hui, *Composites: Part B*, 2012.

82. S. Lee and J. W. Peng, *Physics and Chemistry of Solids*, 2011, **72**, 1133-1139.

83. Y. Sun, Y. Wang and I. Zhitomirsky, *Colloids and Surfaces A: Physicochemical and Engineering Aspects*, 2013, **418**, 131-138.

84. Q. H. Li, Q. H. Zhou, D. Deng, Q. Z. Yu, L. Gu, K. D. Gong and K. H. Xu, *Transactions of Nonferrous Metals Society of China*, 2013, **23**, 1421-1427.

85. Y. Ju, L. Li, Z. Wu and Y. Jiang, *Energy Procedia*, 2011, **12**, 450-455.

86. H. Kangarlou and S. Rafizadeh, *Optik - International Journal for Light and Electron Optics*, 2013, **124**, 2787-2790.

87. M. Wright and A. Uddin, *Solar Energy Materials and Solar Cells*, 2012, **107**, 87-111.

88. N. Aman, P. K. Satapathy, T. Mishra, M. Mahato and N. N. Das, *Materials Research Bulletin*, 2012, **47**, 179-183.

89. S. S. Mali, C. A. Betty, P. N. Bhosale and P. S. Patil, *Electrochimica Acta*, 2012, **59**, 113-120.

90. A. Sobczyk-Guzenda, B. Pietrzyk, W. Jakubowski, H. Szymanowski, W. Szymański, J. Kowalski, K. Oleśko and M. Gazicki-Lipman, *Materials Research Bulletin*, 2013, **48**, 4022-4031.

91. J. Yu and B. Wang, *Applied Catalysis B: Environmental*, 2010, **94**, 295-302.

92. R. Dastjerdi and M. A. Montazer, *Colloids and Surfaces B: Biointerfaces*, 2010, **79**, 5-18.

93. P. S. Shinde, S. B. Sadale, P. S. Patil, P. N. Bhosale, A. Brüger, M. Neumann-Spallart and C. H. Bhosale, *Solar Energy Materials and Solar Cells*, 2008, **92**, 283-290.

94. S. Emin, S. P. Singh, L. Han, N. Satoh and A. Islam, *Solar Energy*, 2011, **85**, 1264-1282.

95. Z. Peining, A. S. Nair, Y. Shengyuan, P. Shengjie, N. K. Elumalai and S. Ramakrishna, *Photochemistry and Photobiology A: Chemistry*, 2012, **231**, 9-18.

96. M. Guo, J. Zhao, X. Xu, G. Liu and X. Wang, *Ceramics International*, 2014, **40**, 5825-5830.

97. J. Guo, X. Cai, Y. Li, R. Zhai, S. Zhou and P. Na, *Chemical Engineering*, 2013, **221**, 342-352.

98. N. Sarlak, M. A. F. Nejad, S. Shakhesi and K. Shabani, *Chemical Engineering*, 2012, **210**, 410-416.

99. M. R. Mohammadi, F. Ordikhani, D. J. Fray and F. Khomamizadeh, *Particuology*, 2011, **9**, 161-169.

100. M. Kobayashi, V. Petrykin, K. Tomita and M. Kakihana, *Crystal Growth*, 2011, **337**, 30-37.

101. S. Bhattacharyya, S. Kymakis and G. A. Amaratung, *Synthetic Metals*, 2004, **16**, 4819-4823.

102. B. Gao, C. Peng, G. Z. Chen and G. L. Puma, *Applied Catalysis B: Environmental*, 2008, **85**, 17-23.

103. G. Jiang, Z. Lin, L. Zhu, Y. Ding and H. Tang, *Carbon*, 2010, **48**, 3369-3375.

104. L. T. Anh, A. K. Rai, T. V. Thi, J. Gim, S. Kim, E. C. Shin, J. S. Lee and J. Kim, *Power Sources*, 2013, **243**, 891-898.

105. M. L. Kääriäinen and D. C. Cameron, *Thin Solid Films*, 2012, **526**, 212-217.

106. S. Song, F. Hong, Z. He, H. Wang, X. Xu and J. Chen, *Applied Surface Science*, 2011, **257**, 10101-10108.

107. Q. Liu, Y. Zhou, Y. Duan, M. Wang, X. Zhao and Y. Lin, *Alloys and Compounds*, 2013, **548**, 161-165.

108. Y. Niu, M. Xing, B. Tian and J. Zhang, *Applied Catalysis B: Environmental*, 2012, **115-116**, 253-260.

109. J. Lu, J. Zhu, Z. Wang, J. Cao and X. Zhou, *Ceramics International*, 2014, **40**, 1489-1494.

110. N. Du, X. Wu, C. Zhai, H. Zhang and D. Yang, *Alloys and Compounds*, 2013, **580**, 457-464.

111. S. Yan, B. Wang, Y. Shi, F. Yang, D. Hu, X. Xu and J. Wu, *Applied Surface Science*, 2013, **285**, 840-845.

112. Y. Haldorai, J.-J. Shim and K. T. Lim, *Supercritical Fluids*, 2012, **71**, 45-63.

113. A. K. Arof, H. K. Jun, L. N. Sim, M. Z. Kufian and B. Sahraoui, *Optical Materials*, 2013, **36**, 135-139.

114. S. Wang, Q. Gong and J. Liang, *Ultrasonics Sonochemistry*, 2009, **16**, 205-208.

115. M. Sánchez and M. E. Rincón, *Sensors and Actuators B: Chemical*, 2009, **140**, 17-23.

116. P. Du, L. Song, J. Xiong, N. Li, L. Wang, Z. Xi, N. Wang, L. Gao and H. Zhu, *Electrochimica Acta*, 2013, **87**, 651-656.

117. A. R. Boccaccini, J. Cho, T. Subhani, C. Kaya and F. Kaya, *European Ceramic Society*, 2010, **30**, 1115-1129.

118. A. Ansón-Casaos, I. Tacchini, A. Unzue and M. T. Martínez, *Applied Surface Science*, 2013, **270**, 675-684.

119. A. Jitianu, T. Cacciaguerra, R. Benoit, S. Delpeux, F. Béguin and S. Bonnamy, *Carbon*, 2004, **42**, 1147-1151.

120. M. Yasutake, Y. Shirakawabe, T. Okawa, S. Mizooka and Y. Nakayama, *Ultramicroscopy*, 2002, **91**, 57-62.

121. M. Endo, M. S. Strano and P. M. Ajaya, *Applied Physics*, 2008, **111**, 13-61.

122. D. Bom, R. Andrews, D. Jacques, J. Anthony, B. Chen, M. S. Meier and J. P. Selegue, *Nano Letters,* 2002, **2**, 615-619.

123. S. Mun, Y. Chen and J. Kim, *Sensors and Actuators B: Chemical*, 2012, **171-172**, 1186-1191.

124. H. W. Chang, Y. C. Tsai, C. W. Cheng, C. Y. Lin and P. H. Wu, *Sensors and Actuators B: Chemical*, 2013, **183**, 34-39.

125. Y. Ando, X. Zhao and H. Shimoyama, *Carbon*, 2001, **39**, 569-574.

126. T. Belin and F. Epron, *Materials Science and Engineering: B*, 2005, **119**, 105-118.

127. S. Scalese, V. Scuderi, S. Bagiante, I. Deretzis, A. L. Magna, C. Bongiorno, G. Compagnini, S. Gibilisco, N. Pilusob and V. Privitera, *Raman Spectroscopy*, 2012, **43**, 1018-1023.

128. D. M. Chipara, J. Macossay, A. V. R. Ybarra, A. C. Chipara, T. M. Eubanks and M. Chipara, *Applied Surface Science,*2103, **275**, 23-27.

129. L. Stobinskia, B. Lesiaka, L. Kövérc, J. Tóthc, S. Biniakd, G. Trykowskid and J. Judeke, *Alloys and Compounds*, 2010, **501**, 77-84.

130. Z. Németh, C. Dieker, Á. Kukovecz, D. Alexander, L. Forró, J. W. Seo and K. Hernadi, *Composites Science and Technology*, 2011, **71**, 87-94.

131. http://www2.eng.cam.ac.uk/~bcb/semhist.htm, Accessed 4 December, 2013.

132. D. J. Smith, *Nanocharacterisation*, 2007, pp. 27.

133. J. P. Tessonnier, D. Rosenthal, T. W. Hansen, C. Hess, M. E. Schuster, R. Blume, F. Girgsdies, N. P. Nder, O. Timpe, D. S. Su and R. S. Gl, *Carbon,* **4,** 2009, 1779-1798.

134. B. Korbély, Z. Németh, B. Réti, J. W. Seo, A. Magrez, L. Forró and K. Hernadi, *Materials Research Bulletin*, 2011, **46**, 1991-1996.

135. R. F. Egerton, *Springer Science and Business Media*, Canada, 2005, vol. 9.

136. S. Manchester, X. Wang, I. Kulaots, Y. Gao and R. H. Hurt, *Carbon*, 2008, **46**, 518-524.

137. B. Gao, G. Z. Chen and G. Li Puma, *Applied Catalysis B: Environmental*, 2009, **89**, 503-509.

138. www.smcr.fisica.unam.mx/8temasutiles/articulosutiles/Bas-XRD.pdf, accessed 24 May, 2013.

139. K. Khosravi , M. E. Hoque , B. Dimock, H. Hintelmann and C. D. Metcalfe, *Analytica Chimica Acta*, 2012, **713**, 86-91.

140. A. Weir, P. Westerhoff , L. Fabricious, K. Hristovski and N. Goetz, *Environmental Science and Technology*, 2012, **46**, 2242-2280.

141. A. P. Packer, D. Larivière, C. Li, M. Chen, A. Fawcett, K. Nielsen, K. Mattson, A. Chatt, C. Scriver and L. S. Erhardt, *Analytica Chimica Acta*, 2007, **588**, 166-172.

142. W. G. Kreyling, M. Semmler-Behnke and Q. Chaudhry, *Nano Today*, 2010, **5**, 165-168.

143. D. Mukheree and S. Chakrabarti, *New Age International Publishers*, India, 2007, pp. 86.

144. I. K. Ding, J. Melas-Kyriazi, N. L. Cevey-Ha, K. G. Chittibabu, S. M. Zakeeruddin, M. Grätzel and M. D. McGehee, *Organic Electronics*, 2010, **11**, 1217-1222.

145. H. C. Weerasisinghe, P. M. Sirimanne, G. P. Simon and X. B. Cheng, *Photochemistry and Photobiology*, 2009, **206**, 64-70.

146. W. Guo, L. Wu, Z. Chen, G. Boschloo, A. Hagfeldt and T. Ma, *Photochemistry and Photobiology A: Chemistry*, 2011, **219**, 180-187.

147. W. J. Lin, C. T. Hsu and Y. C. Tsai, *Colloid and Interface Science*, 2011, **358**, 562-566.

148. E. L. Ratcliffe, B. Zacher and N. R. Armstrong, *Physical Chemistry Letters*, 2013, **11**, 1337-1350.

149. L. Cheng , J. Wu , Y. Xiao , Y. Chen , H. Yu , Z. Tang , J. Lin and M. Huang, 2012, **2**, 224-230.

150. Q. J. Yu , Y. H. Zhang , Y. Yi , N. N. Zu , J. Zhang and P. Wang, *American Chemical Society Nano*, 2010, **4**, 6032-6038.

151. S. R. Jang, M. J. Choi, R. Vittal and K. J. Kim, *Solar Energy Materials and Solar Cells*, 2007, **91**, 1209-1214.

152. M. K. Lim, S. R. Jang, R. Vittal, J. Lee and K. J. Kim, *Photochemistry and Photobiology A: Chemistry*, 2007, **190**, 128-134.

153. S. Yang, H. Kou, S. Song, H. Wang and W. Fu, *Colloids and Surfaces A: Physicochemical and Engineering Aspects*, 2009, **340**, 182-186.

154. J. Spivack, O. Siclovan, S. Gasaway, E. Williams, A. Yakimov and J. Gui, *Solar Energy Materials and Solar Cells*, 2006, **90**, 1296-1307.

155. Y. Zhao, K. Jiang, W. Xu and D. Zhu, *Tetrahedron*, 2012, **68**, 9113-9118.

156. B. Qi and J. Wang, *Physical Chemistry,* 2013, **2**, 8972-8982.

157. M. A. Green, *Solid-State Electronics*, 1981, **24**, pp. 788-789.

Chapter Three

Experimental details

This chapter presents details on the reagents, equipment, and various experimental conditions involved in the synthesis of the MWCNT-titania nanocomposites and dye sensitised solar cells (DSSCs).

3.1 Reagents and solvents for nanocomposite synthesis

- Ethanol (Analar, BDH, 99.7% to 100%)
- Concentrated sulfuric acid (SSM Instruments, South Africa, AR, 98% to 100%)
- Nitric acid (Sigma Aldrich, Germany, ISO, $\geq$ 69%)
- Hydrochloric acid (SMM Instruments, South Africa, $\geq$ 32%)
- Titanium(IV) isopropoxide (Sigma Aldrich, India, 97%)
- Titanium(IV) methoxide (Sigma Aldrich, USA, 95%)
- Titanium(IV) dioxide (Sigma Aldrich, Germany, 99-100%)
- Titanium standard (Industrial Analytical, South Africa, 1.002±5 µg/mL, 2%)
- Double distilled water (Biby sterlin ltd, England, Aquatron model A4000Dl)
- MWCNTs (8-15 nm OD, length 10 – 50 μm , ash $<$ 1.5 wt%, SSA $>$ 233 m^2/g, EC $>10^{-2}$ S/cm, SKU number 030102,95 wt%) – Purchased from Cheaptubes.com (www.cheaptubes.com)

3.2 Reagents and solvents for DSSCs

- Acetonitrile (Merck Schuchardt, Germany HPLC grade, 99.9%)
- Iodine-resublimed (Analysed Analytical Reagent, AAR, SMM instruments)
- Ethanol (Analar, BDH, 99.7% to 100%)
- 1-Methyl-3-propylimazolium iodide (Sigma Aldrich, Germany, HPLC grade, $\geq$ 98%)
- Lithium iodide (Sigma Aldrich, Germany, Trace metal basis, 99.9%)
- Eosin B (Sigma Aldrich, USA, 90%)

- Guanidinium thiocynate for synthesis (Merck Shuchardt, OHG, Germany, IR passed test, Assay $\geq$ 98%)
- 4 Tert-butylpyridine (Sigma Aldrich, USA, 96%)
- Polyvinyl acetate (PVAc) (Sigma Aldrich, USA, MW = 100 000 $gmol^{-1}$)
- Nanocomposites (synthesised in this work)
- ITO glass (Lumtec, Taiwan, 15 Ω, 30 × 30 × 0.7 mm)

3.3 Equipment and apparatus

The subsequent sections present details of the equipment that was used for the synthesis of the MWCNT-titania nanocomposites.

- Stirring and digestion of nanocomposites for ICP-OES was done on a Lab Smart MS-H-Pro^{+} model hot plate. Sintering of DSSCs was also done on a hot plate.
- Ultrasonic water bath treatment was done with a digital ultrasonic heater supplied by Shalom lab, South Africa.
- Calcining and chemical vapour deposition synthesis was done in an Elite thermal system TSH12/50/610 model tube furnace.

3.3.1 Metal-organic chemical vapour deposition reactor

The metal-organic chemical vapour deposition (MOCVD) apparatus was constructed with commercially available stainless steel parts, which were purchased from Swagelok (Swagelock, Durban, South Africa). The bottom of the reactor was made of Swagelock 316 SS VCR face seal fitting, 1/2 in. cap. The reactor consisted of a cylindrical stainless steel (Sandvick 3R60 ASTME/ASME, Canada) reaction chamber body made from 316/316L SS seamless tubing (1/2 in. OD x 0.035 in. wall x 6 meters) sealed at one end (top) with a Swagelock face seal fitting with a blind gasket (see **Figure 3.1**). The top consisted of a Swagelock 316 2DA and PSIG SS-42GS4-A. A 316 SS VCR face seal fitting, 1/2 in. silver-plated filter gasket, non-retained style, 0.5 micron was fitted at the bottom to minimise loss of sample and contamination of the whole system connected to a vacuum pump.

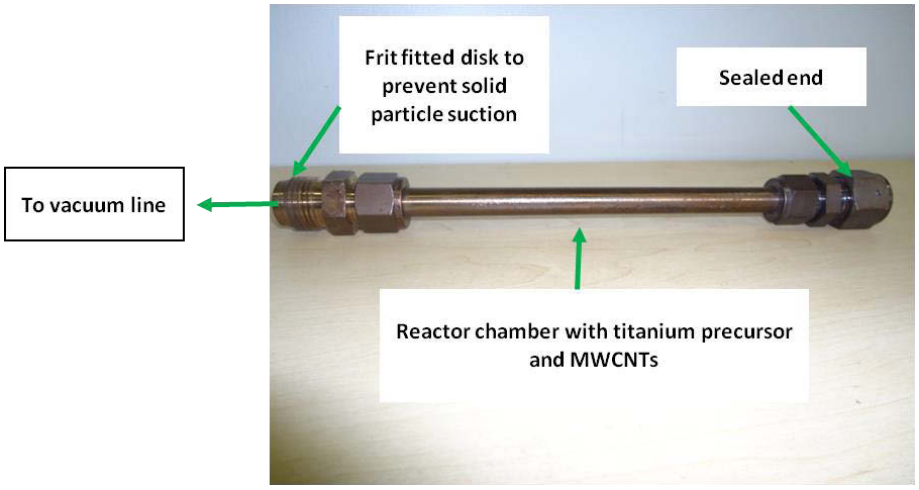

Figure 3.1: A photograph of the MOCVD reactor used in the CVD synthesis of MWCNT-titania nanocomposites

The vacuum line was constructed from 316/316L SS seamless tubing, (1/4 in. OD x 0.035 in. wall x 6 meters). Valves were included in the system by use of SS 1-piece 40 series angle pattern ball valves, (0.35 cv, 1/4 in). A 316 SS VCR face seal fitting, 1/2 in. female nut was used to seal the VCR fittings and SS Swagelok tube fitting, 1/2 in. x 1/4 in. tube OD was used to connect 1/4 Swagelok fitting to the tubing coming from the valve. A thyracont VD84/1 Pirani vacuum gauge was used to measure absolute pressure.

3.3.2 Nanocomposite synthesis experiments

This section outlines the stages involved in nanocomposite synthesis from acid treatment of pristine MWCNTs. Two synthetic methods which were sol-gel and CVD were used in this work and are presented in **sections 3.3.2.1** and **3.3.2.2**. The as prepared nanocomposites had varying wt.% of MWCNTs in the range 2-98 wt.%.

Acid treatment was first carried out to introduce oxygen containing functional groups onto the MWCNTs tube walls and to remove iron. Iron was introduced in MWCNTs as a catalyst in pyrolysis (during the SCNM synthesis).

The acid treatment of the MWCNTs was carried out in an ultrasonic water bath for 4 hrs. The general mixing ratio consisted of about 1 g of MWCNTs (accurately weighed) in an acid

mixture made up of 30 mL of HNO_3 and 10 mL HCl. The water bath temperature was generally kept at 60 °C for 4 hrs while the application of the ultrasound energy was set to go off for 15 min for every 30 min of 'on-time' to prevent tube shortening (total of 6 hrs under treatment). Initially a Buchner funnel was used for vacuum filtration ensuring that there were no MWCNTs passing through the filter paper but gravity filtration was later used instead for convenience since drainage did not require close monitoring as in vacuum filtration. The residue was washed with distilled water until the water draining through was neutral. Neutrality was checked by using a blue litmus paper. The MWCNTs were left to dry in open air overnight, then dried at 120 °C in a Scientific Economy 220 model oven and stored in a desiccator. At this stage the MWCNTs were ready for nanocomposite synthesis.

3.3.2.1 Sol-gel method

During loading of TiO_2 onto MWCNTs, high ratios of MWCNTs and small ratios of titania, was done by accurately weighing MWCNTs. The MWCNTs were thereafter dispersed in 30 mL ethanol and treated with an ultrasonic water bath for 10 min to reduce agglomeration. A predetermined volume of titanium(IV) isopropoxide (TIP) was added with a micro-pipette to 10 mL of ethanol. For large titania wt.%, a measuring cylinder was used to measure the volume of TIP.

The volume of TIP required was calculated as follows:

For 1:1 wt.% ratio using 0.5 g of MWCNTs, if x is mass of titania required then

$$\frac{x}{x + 0.25} = 0.5$$

$$x - 0.5x = 0.25 \times 0.5$$

$$x = 0.25\ g$$

$$\text{Number of moles of titania in 0.25 g} = \frac{0.25}{79.866} = 0.00313 \text{ mol}$$

$$\text{Mass of titanium(IV) isopropoxide} = \frac{0.25}{79.866} \times 284.22\ g = 0.8897 g$$

$$\text{Volume of titanium(IV) isopropoxide} = \frac{0.8897g}{0.96\,\frac{g}{mL}} = 0.9268\,mL$$

The TIP dispersed in 10 mL of ethanol was added to MWCNTs. The mixture was treated in an ultrasonic water bath for 30 min, followed by stirring for 30 min at 1000 rpm to improve homogeneity and contact. The reaction mixture was then left for about 16 hrs in air with no stirring. The nanocomposites were filtered using vacuum until dry and left exposed to air overnight. Thereafter, calcining was carried out at 4 °C/min linearly up to 400 °C and held there for 30 min in a furnace open to air. This step was meant to decompose the organic components of the titanium precursor. High titania wt.% ratio nanocomposites, i.e. loading MWCNTs onto TiO_2, were synthesised in a similar way. The nanocomposites with high titania wt.% were dried at 120 °C in an oven prior to calcining because they had more water adsorbed on the surface.

3.3.2.2 CVD method

In this section the loading of TiO_2 onto MWCNTs by the CVD method is described. The general procedure was to accurately weigh MWCNTs (0.5000 g or 1.000 g) then mixing them with a predetermined mass of titanium(IV) methoxide (TM) with the aid of a pestle and mortar.

Calculation example:

For 1:1 wt.% ratio using 0.5 g of MWCNTs, if x is the mass of titania required then

$$\text{Mass of titanium methoxide} = \frac{0.25mol}{79.866} \times 172\ g\ mol^{-1} = 0.5384\ \text{g}$$

The mixture was transferred into the MOCVD reactor (details discussed in **section 3.3.1.**) and the reactor inserted horizontally in a tube furnace connected to a vacuum pump (see **Figure 3.2**). The vacuum pump was turned on with valve one opened, valve two closed, and the furnace off. Valve two was only opened when a pressure of about 1.3×10^{-2} mbar had been achieved and the furnace was turned on when the whole system was at about the

same pressure. The furnace temperature programme was to reach 100 °C in 50 min from room temperature and held for 30 min in order to remove water, the temperature was then raised to 400 °C in 3 hrs 33 min and held there for 30 min before dropping back to room temperature. The heating temperature programme was kept below 400 °C partly to avoid titania from changing phase to rutile and to avoid the loss of MWCNTs by thermal decomposition. The vacuum pump was turned off after the valve was closed during the heating phase between 100 °C and 400 °C (after the first 30 min at 100 °C). The nanocomposite was stored in a desiccator. The apparatus allowed sublimation of the precursor and reactive deposition of titania onto the MWCNTs in the same reactor.

For loading MWCNTs onto TiO_2 by CVD method i.e. high ratios of titania, a predetermined mass of MWCNTs was mixed with 1.3882 g TM with a pestle and mortar. The mixture was transferred into the reactor and the apparatus set-up horizontally with the reactor inserted in a furnace connected to vacuum pump as explained above. The procedures were done in the same way as above.

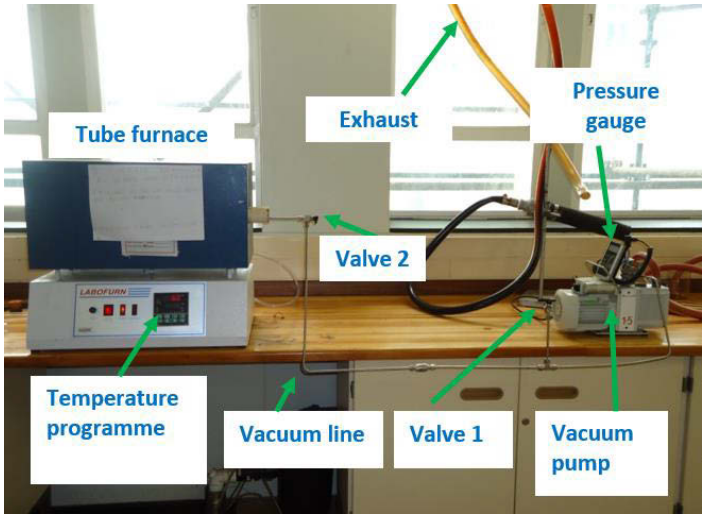

Figure 3.2: Photograph of the CVD experimental set-up used in the synthesis of the MWCNT-titania nanocomposites

3.4 Characterisation instruments

The physicochemical properties of the synthesized nanocomposites were investigated thoroughly by means of the techniques outlined in the subsequent sections.

3.4.1 Scanning electron microscopy

The morphology of the MWCNT-titania nanocomposites was investigated by means of scanning electron microscopy (SEM) using a JEOL JSM 6100. The accelerating voltage was 10 kV. Aluminium stubs were used as sample holders and the required sample size was sprinkled on top of a carbon tape. The optimum working distance was about 7 mm and the aperture size was 30 μm. The software package employed in the data acquisition and analysis from the instrument was Zeiss Smart SEM version 5.03.06.

3.4.2 Electron dispersive X-ray spectroscopy

Electron dispersive X-ray spectroscopy (EDX) was used as a qualitative technique for the detection of titanium, carbon and also as an indication of whether the nanocomposites consisted of titania and MWCNTs. EDX was also used to check for the presence of a metal catalysts contaminant from MWCNT synthesis. The instrument used for EDX was a Bruker X-ray spectrometer attached to the JEOL JSM 6100 SEM instrument. The optimum working distance was 4 mm. The magnification of images was at 2.5 µm and the scans lasted for 5 min. Bruker Espirit 1.8 software was used for data acquisition.

Elemental mapping was done on a separate instrument, a JEOL 2100 attached to the SEM instrument above. Data from this analysis technique was limited to qualitative analysis. This was because of limited fluctuating number of electrons bombarding the sample, noise interferences, and variation in the number of backscattered electrons and number of generated X-rays emitted by the sample on bombardment. These affect repeatability and precision of quantitative analysis.[1]

3.4.3 Transmission electron microscopy

The dimensions and topography of the nanocomposites were investigated by using transmission electron microscopy (TEM). The instrument used was the JEOL JEM 1010 transmission electron microscope using lacey or holey carbon-coated copper grids. The images were taken at different magnifications by using the Megaview 3 camera. Sample preparation for imaging began with ultrasonic water bath treatment of the nanocomposites in 1 mL of ethanol for 3-5 min. The grids were then dipped into the ethanolic dispersion and allowed to dry prior to insertion in the specimen chamber. Image J® software was used to compute the length of the outer diameters of the MWCNTs in the nanocomposites. At least 200 MWCNTs were counted.

3.4.4 High resolution transmission electron microscopy

The as prepared nanocomposites were also investigated by high resolution transmission electron microscopy (HRTEM). An HRTEM (model JEOL JEM 2100 200 KV) instrument was used to further observe the morphology and existence of lattice fringes due to titania on the MWCNT walls in the nanocomposites.

3.4.5 Fourier transform infrared spectroscopy

Fourier transformation infrared spectroscopy (FTIR) analysis were done on a pellet disk by using a Perkin Elmer FTIR spectrometer. 0.1500 g powder was pressed into a pellet under pressure of 10 Tons for about 2 min. The ring press model was 00-25 supplied by Research Industrial Company, England. The pellet consisted of KBr:nanocomposite ratio of 500:1 weighed using a Shimadzu analytical balance. Air scanning was done to remove any CO_2 absorption in the background. Thereafter, the pellet disks were scanned from 350 – 4500 cm^{-1}. The data from the instrument was initially saved as an Ascii file then as an Excel document by using the computer connected to the instrument. The data analysis was done using Origin software.

3.4.6 Inductively coupled plasma-optical emission spectroscopy

Digestion of titanium was difficult since it is a refractory material and therefore not soluble to most acids and/or mixtures such aqua regia. Several sulfuric: nitric acid ratios were tried until a mixing ratio with the best titania solubility was identified. An accurately weighed (50 mg) mass of nanocomposite was digested with a mixture of sulfuric and nitric acids (98 -100 % H_2SO_4: ≥ 37 % HNO_3, ratio 10:1) and heated at 350 °C on a hot plate whilst stirring for 5 min. The digest was diluted into 100 mL volumetric flask. A 1 mL aliquot was diluted in a 100 mL volumetric flask using double distilled water. Double distilled water was used to wash the digestion vessels and as the blank. It was also used in making standard solutions. Standards used were 2 mg/L, 4 mg/L, 6 mg/L, 8 mg/L and 10 mg/L. A standard calibration curve was obtained on every run. The instrumental parameters used are shown in **Table 3.1**.

Table 3.1: ICP-OES instrumental conditions used in the titania concentration determination

Parameter	Condition
Power (W)	1300
Plasma gas flow rate (L min^{-1})	15
Auxiliary gas flow rate (L min^{-1})	0.2
Nebulizer gas flow rate (L min^{-1})	0.8
Pump flow rate (ml min^{-1})	1.5
Wavelength (nm)	336.121

The titania wt.% was calculated as shown below:

$$\text{Dilution factor from digested nanocomposite} = \frac{100}{1} = 100$$

Inductively coupled plasma-optical emission spectroscopy (ICP-OES) reading for sample with a theoretical wt.% of 60, was 2.981 mg L^{-1} and nanocomposite mass digested was 50.5 mg

$$\text{Mass of Ti from the digested nanocomposite} = \frac{2.981\ mg \times 0.1\ L \times 100}{L}$$

$$\text{Ti wt.\%} = \frac{29.81}{50.5} \times 100 = 59.0297\%$$

Activated carbon was spiked with known amounts of titania and the samples were digested in a similar way as the nanocomposites. This procedure was done to validate the results obtained from the nanocomposites since no commercial reference materials were available during the time of the experiments.

3.4.7 Thermogravimetric analysis

Thermal stability analysis was confirmed by using a TA Instrument Q series™ Thermal Analyser TGA (Q600). The measurements were done in oxygen flowing at 50 mL/min from ambient temperature to 1000 °C, the isothermal time was 1 min and the ramp temperature was 10 °C/min. TA instruments Universal Analysis 2000 software package was used for data acquisition and analysis. Origin software was used to re-plot the weight-loss curves for the determination of oxidative stability of MWCNTs, i.e. initiation and oxidation temperatures.

3.4.8 Raman spectroscopy

The measurements were done with a Delta Nu Advantage 532™ Raman spectrometer. The detector used was a 2D CCD detector and grating lines were 1800 per mm. The excitation wavelength of the laser was 532 nm and the power generally used was medium high (as per instruments software). The integration time was 35 s and resolution was 10 cm^{-1}. An average of three spectra was acquired for each nanocomposite. A background smoothening was done by using the Raman instrument. The analysis of data from the instrument was done by using Origin software package.

3.4.9 Powder X-ray diffraction

Powder X-ray diffraction (XRD) analysis were done to deduce crystallinity and the phase of titania in the nanocomposite. XRD instrument used in this work was D8 Advance diffractometer supplied by BRUKER AXS, Germany. Measurements were done with a θ-θ scan in locked coupled mode, with Cu-Kα radiation (λK_1 = 1.5406 Å) and the detectors used were PSD Vantec-1. The measurement parameters are shown in **Table 3.2**. The instrument software used for the analysis of data was EVA software from BRUKER.

Table 3.2: Instrumental parameters employed in the MWCNT-titania XRD measurements

Parameter	Value
Tube voltage	40 kV
Tube current	40 mA
Variable slits	V20 variable slit
2θ Range	10 - 89.94
Increment Δ 2θ	0.028
Measurement time	0.5 s/step

3.4.10 Textural characterisation

Accurately weighed masses of the nanocomposites in an analysis tube were degassed at 90 °C for one hr and then at 160 °C overnight. The nanocomposites were accurately reweighed after degassing. The textural analyses were done by using a Micrometrics TRI STAR 3020V1.03 (V1.03) instrument at 77 K in N_2. The adsorption/desorption isotherms obtained were fitted to the BET equation in order to determine the surface areas of the nanocomposites. The pore volumes were obtained from the BJH model.

3.4.11 Diffuse reflectance

A HR2000$^+$ model High Resolution spectrometer was used with halogen HL-2000-FHSA light source supplied by Narich. The software used for data acquisition was spectra suite. A T300-RT-UV-VIS EOS 1212277 optical fibre was used for data transfer. Ten scans were averaged, box width was five and integration time was 15 ms.

3.4.12 Photoluminescence

Photoluminescence (PL) was done by using a Perkin Elmer LS35 fluorescence spectrometer. A front surface accessory LS55 model solid probe was used since the nanocomposites were in a solid state. Excitation was done at 300 nm, spectrum range from 450 to 700 nm, excitation slit was 5 nm, emission slit was 0 nm and scan speed was 120 nm/min. The software used for data acquisition was FL Winlab version 4.00.03 Perkin Elmer Inc.

3.4.13 Conductivity

A conductivity meter was purchased from Wellhelm, Germany and the model was Cond 7110, WTW 82362 certified to Can/CSA standard C222.

A Perkin Elmer UV Winlab UV-Vis spectrometer was used to obtain the absorption spectrum of Eosin B. The software used was Lambda 35 version 2.85.04.

3.4.14 Solar simulator

Photo-electrochemical measurements were done using a solar simulator supplied by Keithley instruments, USA, (model SS50AAA) with a Xenon short AKC 150 W lamp, light source was steady state (shutter controlled), Air mass (AM) was 1.5 G, voltage was 116-220 V, frequency was 50-60 Hz and maximum power was 750 W. Complete IV measurements for PV were done using PVIV test solution Oriel Instruments.

3.4.15 Thermoevaporator

A thermoevaporator (depositing unit) carbolite type 300 supplied by Barloworld scientific was used to deposit alumium layer on glass. i.e. counter electrode. Multi-film rate/ thickness monitor (Inficon) instruments for intelligent control SQM 160 by Keithley that uses Inficon quartz crystal sensor technology to measure rate and thickness in the film deposition processes.

3.5 Solar cell experiments

This section give details of the experiments carried out in application of the nanocomposites synthesised as explained in the previous section.

3.5.1 Synthesis of gel state electrolyte

The concentration of iodine was optimised prior to synthesis of a liquid electrolyte in terms of conductivity. This was done by dissolving a predetermined mass of iodine in acetonitrile and optimised by a conductivity meter. A liquid electrolyte was synthesized by mixing lithium iodide (0.6695 g), iodine (0.6346 g), 1-methyl-3-propylimidazolium iodide (7.5622 g), 4-tert-butylpyridine (3.38 g) and guanidium thiocyanate (0.5914 g) before dissolving in a 50 mL volumetric flask with acetonitrile and then filled to the mark. Liquid electrolyte (2.4986 g) was mixed with PVAc (1.2044 g). A glass rod was then used to stir until the polymer dissolved completely and thereafter stored in the fridge.

3.5.2 Fabrication of dye-sensitised solar cells

Nanocomposites (100 mg) were added to ethanol (0.3 mL). The mixture was treated for at least 20 minutes in an ultrasonic water bath. Nanocomposite dispersed in ethanol were then deposited onto ITO coated glass using the doctor blade method (See **Figure 3.3**).[2,14] The use of PEG binder in deposition of nanocomposites onto ITO was also investigated. A scotch tape was used to control the film thickness. The thickness of the layers were measured using a micrometer screw gauge. The electrode was then sintered at 300 °C for 30 minutes by means of a hotplate. Eosin B dye (150 μL) was added using a micropipette onto the anode electrode. Plasticine was placed on either side of the deposited nanocomposite to prevent the electrolyte from flowing outside the active area. The electrolytes used were iodine liquid and gel state electrolyte.

Aluminium was then used as the counter electrode and the thickness of aluminium deposited on the glass was 0.608 KÅ. The device was made with aluminium coated glass

side facing the dye stained nanocomposite in a sandwitch like fashion (see **Figure 3.3**). The counter electrode was connected to the cathode terminal and nanocomposite to the anode before illuminated with 1 sun (100 mW cm^{-2}) through the nanocomposite side (see **Figure 3.3**).

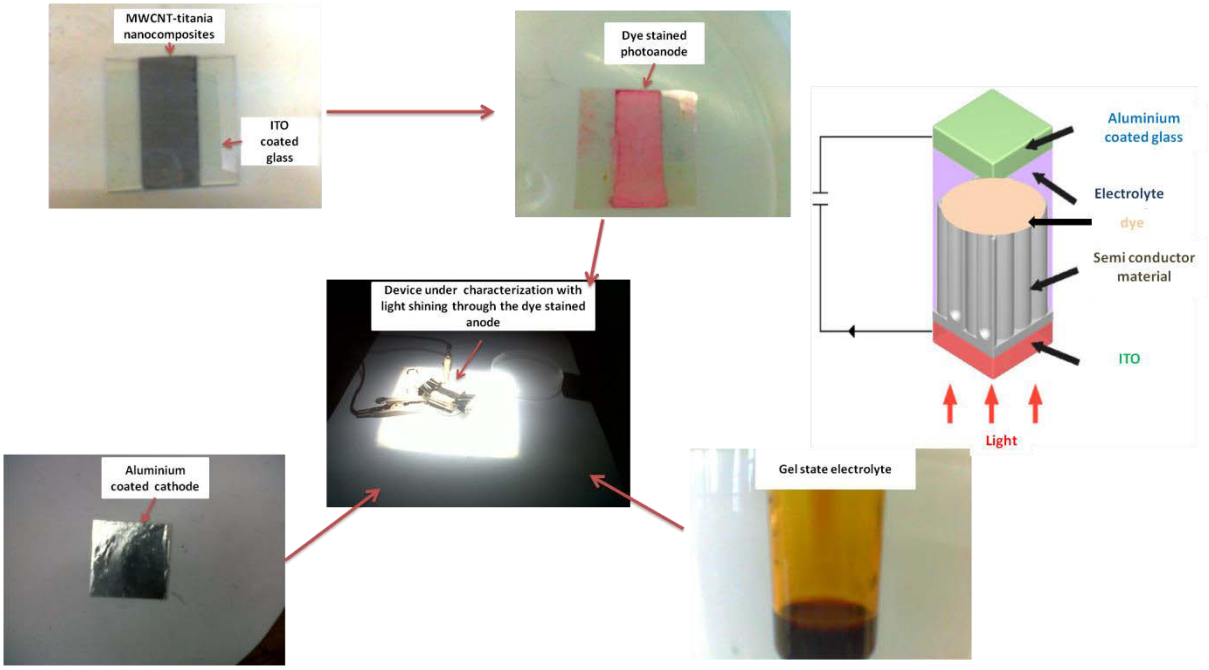

Figure 3.3: The images of DSSC components and complete device under characterisation

Five measurements were taken for each device and the best result recorded. To control and determine the film thickness used as photoanode material a micrometer screw gauge was used to measure the thickness of the scotch tape.

Chapter Four

Physicochemical characterisation of the nanocomposites

In this chapter the results and discussion on the physicochemical properties of multiwalled carbon nanotube-titania (MWCNT-titania) nanocomposites synthesised in this work are presented. The materials were characterised by means of scanning electron microscopy (SEM), electron dispersive X-ray (EDX) spectroscopy, transmission electron microscopy (TEM), high resolution transmission electron microscopy (HRTEM), inductively coupled plasma-optical emission spectroscopy (ICP-OES), Fourier transformation infrared (FTIR), Raman spectroscopy, thermogravimetric analysis (TGA), powder X-ray diffraction spectroscopy (XRD) and textural investigations.

4.1 Morphology

A number of MWCNT-titania nanocomposites were synthesised by varying the wt.% of MWCNTs, i.e. 2, 5, 10, 15, 20, 40, 50, 60, 80, 90 and 95 wt.% by means of the sol-gel and CVD methods. In this work, these nanocomposites are discussed by their targeted wt.% rather than the actual experimental loadings.

The first step in the synthesis of the nanocomposites was to functionalise the commercially purchased MWCNTs. The acid treatment using mild ultrasonic bath was principally chosen because it has been reported to cause both minimal damage to MWCNTs and to open the ends of the MWCNTs to enable the removal of impurities.[1] Common impurities in MWCNTs are metal oxide particles arising from the catalyst used in their synthesis and soot-like amorphous carbon pyrolysis formed as a by-product. Such defects on MWCNTs alter their physicochemical properties such as lowering the thermal decomposition stability.[1] Most importantly, amorphous carbon can interfere with MWCNT/titania interactions in electrochemistry and disperseability in ethanol during the synthetic sol-gel method.[1,2] The acid treatment of MWCNTs was done to improve their dispersion in ethanol and thereby

enhance chemical interactions during MWCNT-titania nanocomposite synthesis. Similar observations have been reported in the literature.[1,3] In these reports the acid treatment of MWCNTs introduces oxygen-containing surface groups. This improve the overall chemical reactivity of the MWCNTs and the dispersion of metal or metal oxides onto the surfaces of the MWCNTs. Ultrasonic treatment detaches loosely attached amorphous carbon *via* acoustic streaming and jet pulses.[1]

SEM was used to check the morphology of the MWCNTs after acid treatment and in the MWCNT-titania nanocomposites. A comparison of the SEM images of the as-received pristine MWCNTs (see **Figure 4.1A**) and the acid-treated MWCNTs (see **Figure 4.1B**) indicates fewer agglomerates in the acid treated-MWCNTs. However, this is not conclusive. The key findings from SEM analysis are that the acid treatment did not drastically alter the surface morphology of the MWCNTs. The lengths and diameters are not significantly affected by acid treatment. Several authors have noted that a mixture of concentrated H_2SO_4 and HNO_3 does not severely damage MWCNTs. Our results using a mixture of HCl and HNO_3 show a similar trend and corroborate those earlier reports.[3-5]

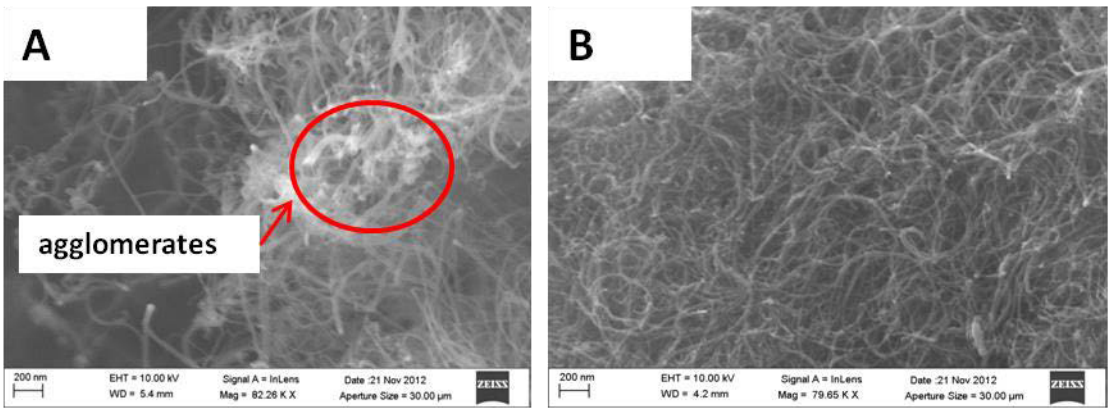

Figure 4.1: Morphology of (**A**) pristine MWCNTs and (**B**) MWCNTs treated with a mixture of nitric and hydrochloric acids in the ratio 3:1 in an ultrasonic water bath

Typical electron microscopy images of the morphology of the MWCNT-titania nanocomposites are shown in **Figures 4.2** and **4.3**. The SEM images generally show that titania coated the MWCNTs. With the sol-gel samples, at low titania loadings (designated 90

wt.% and 80 wt.% MWCNTs) the metal oxide forms isolated particulate-like structures on the walls of the MWCNTs. With increasing amounts of titania, the sol-gel method results in more coating of material along the walls of the MWCNTs. However, the SEM images do show that some tubes are not uniformly coated, and that spherical titania agglomerates form that are not associated with the MWCNTs. The morphology of MWCNT-titania nanocomposites observed was similar to the structures reported by several authors,[6-10] especially at high MWCNT ratios.[11] The use of surfactants to detangle MWCNTs and thereby cause their separation and flexibility has been reported.[13] In this study no surfactants were used, therefore it must be concluded that the ratios of the components in the nanocomposites influenced the distribution of titania on the MWCNTs tube walls. As can be seen in **Figures 4.2** and **4.3** there was a shift from isolated titania particulates to a uniform coating of the MWCNTs with an increase in the titania wt.%.[14] The increase in appearance of titania nanoparticle aggregates in the MWCNTs walls with an increase in the wt.% ratios of titania (see **Figure 4.2C**) shows that MWCNTs are centres of deposition.[15] A comparison of the morphology at 10 and 20 wt.% MWCNTs by the sol-gel and CVD methods (see **Figures 4.2** and **4.3**), shows that the CVD approach gave a more uniform coating of titania on the MWCNTs than the sol-gel.

The observations by SEM of smaller titania particulates on acid-treated MWCNTs (shown in **Figure 4.2B** and **C**) concurred with the observations by Zhao *et al.*[16] in that the MWCNTs were homogenously covered. However, in some instances more than one MWCNT was coated together in a cluster in the CVD method (see additional information in **Appendix G**, **Figure G2**). This was not observed in the sol-gel method because the synthesis procedure involved the use of an ultrasonic water bath and stirring which reduces the chances of agglomeration. MWCNTs were completely coated at 2 and 10 wt.% of MWCNTs (low MWCNTs wt.%) in the nanocomposites synthesised by CVD method (see **Figure 4.3**). At 10 wt.% of MWCNTs most MWCNTs were fully coated although some bare MWCNTs were visible. Furthermore, Fana *et al.*[2] reported that defects such as roughened surfaces on the MWCNT walls are vital nucleation centres for metal oxide deposition. In another report, explanation by Aman *et al.*[12] basis was the mismatch of particle size of Ti^{4+} cations (6.8 nm) and MWCNTs diameter. The MWCNT size promote particle growth on the surface and thus titania is deposited onto the MWCNTs walls since it cannot fit inside the MWCNTs.[12] Also,

the MWCNT interlayer spacing, i.e. 0.34 nm, is similar to the titania d-spacing, i.e. 0.35 nm, and therefore titania particles cannot fit in-between layers.[18,19]

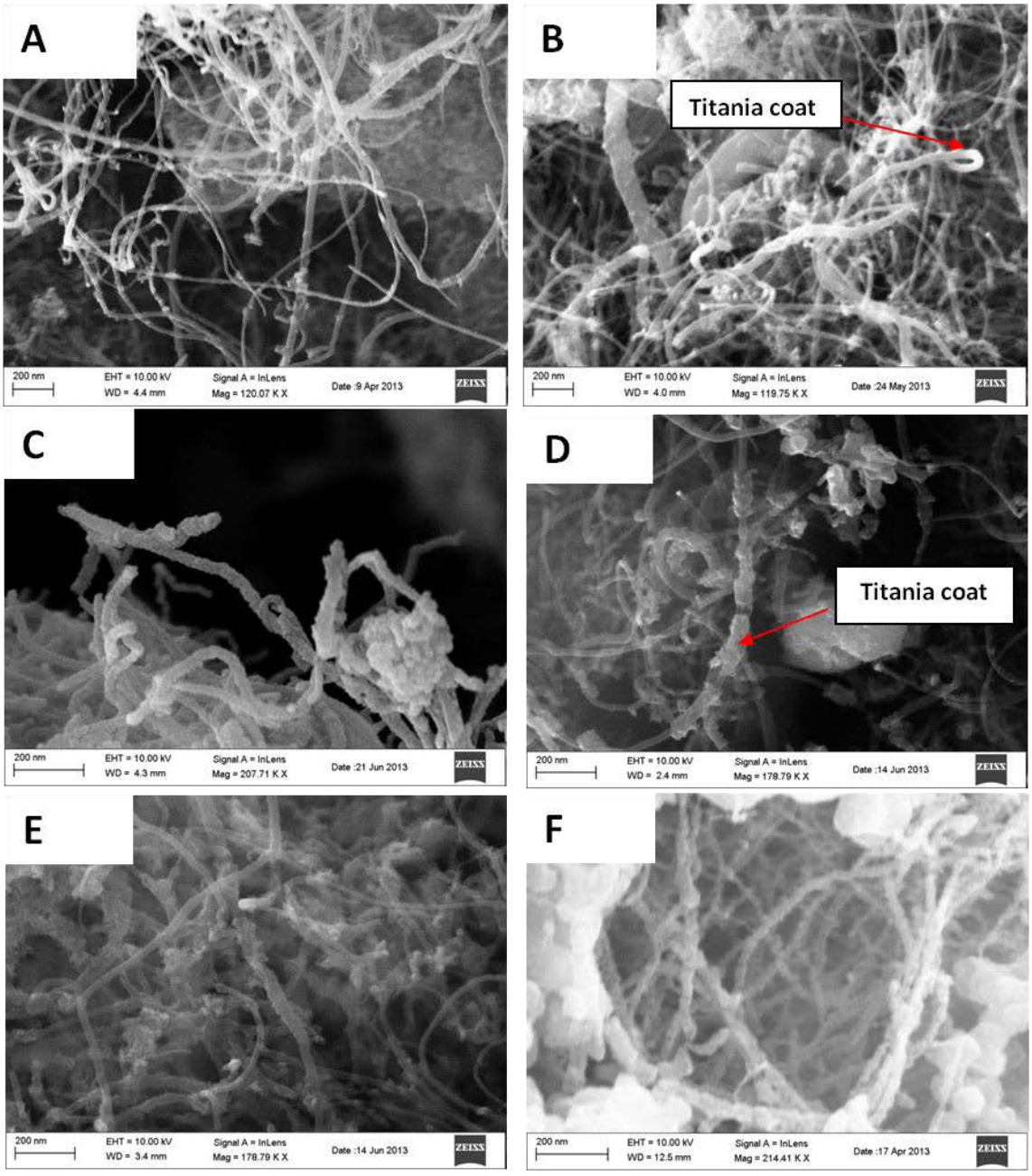

Figure 4.2: Morphology of MWCNT-titania nanocomposites synthesised by the sol-gel method at MWCNT wt.% of: (**A**) 90, (**B**) 80, (**C**) 50, (**D**) 20 (**E**) 10 and (**F**) 2

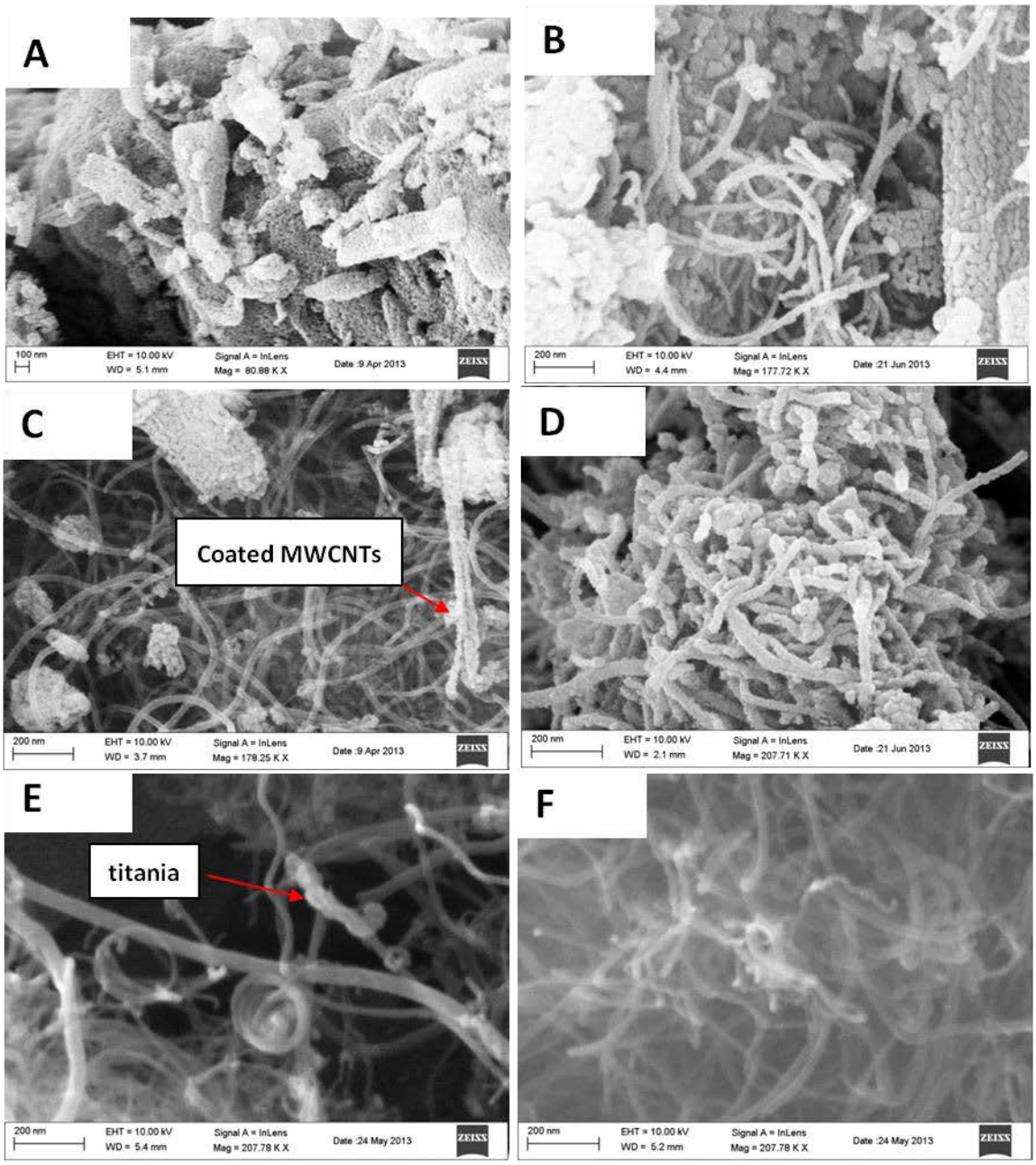

Figure 4.3: Typical morphology of MWCNT-titania nanocomposites synthesised by the CVD method at MWCNT wt.% of: (**A**) 2, (**B**) 10, (**C**) 20, (**D**) 50, (**E**) 80 and (**F**) 90

MWCNTs are covered homogeneously *via* preferential heterogeneous nucleation on hydroxyl, carbonyl and carboxyl groups on the MWCNT surfaces.[16] In the nanocomposites with a 1:1 titania:MWCNT ratio, nanocomposites synthesized by the CVD method had more agglomerated titania than those prepared by the sol-gel method (see **Figure 4.4**) even though the component ratios were the same. Again this suggest the influence of the

synthetic method on the ultimate morphology of the nanocomposites, e.g. the use of an ultrasonic water bath during the sol-gel method. Also, it is noted that at a 1:1 ratio of MWCNT:titania the nanocomposites were more spaghetti-like (see **Figure 4.4**), i.e. more randomly oriented in the sol-gel method than the CVD method.[20]

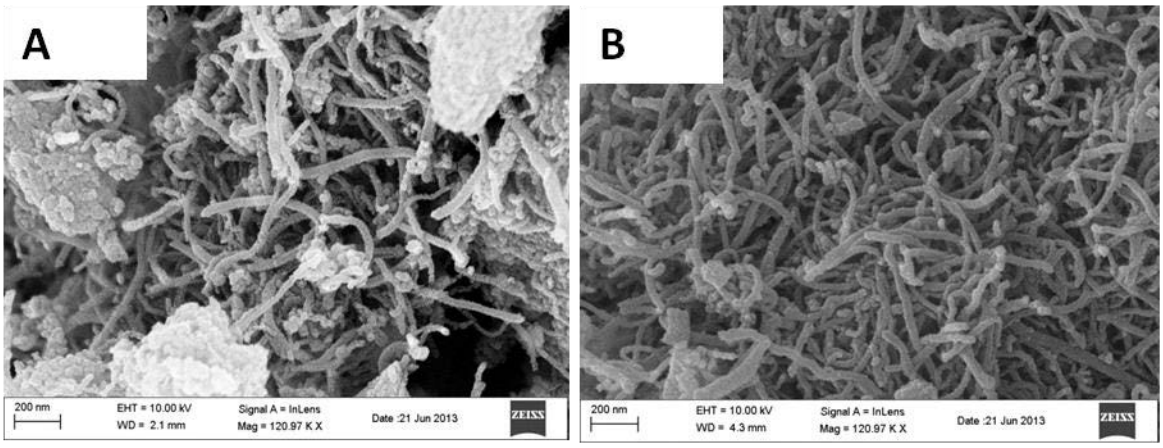

Figure 4.4: A comparison of the morphology at a 1:1 wt.% ratio of MWCNTs:titania for the nanocomposites synthesised by the (**A**) CVD and (**B**) sol-gel methods

4.2 Dimensions of MWCNTs in the nanocomposites and in their pristine state

To further investigate the structure and morphology of the nanostructures in the nanocomposites TEM was carried out. The diameters of the images from both the CVD and sol-gel methods at similar wt.% ratios were compared. In this section, representative images of MWCNTs and MWCNT-titania nanocomposites are displayed. The TEM image shown in **Figure 4.5** shows that pristine MWCNTs had some encapsulated iron particles. By using the Image J® software, the outer diameters of 200 different MWCNTs from several TEM images were measured. Data was then rearranged according to sizes and histograms were plotted.

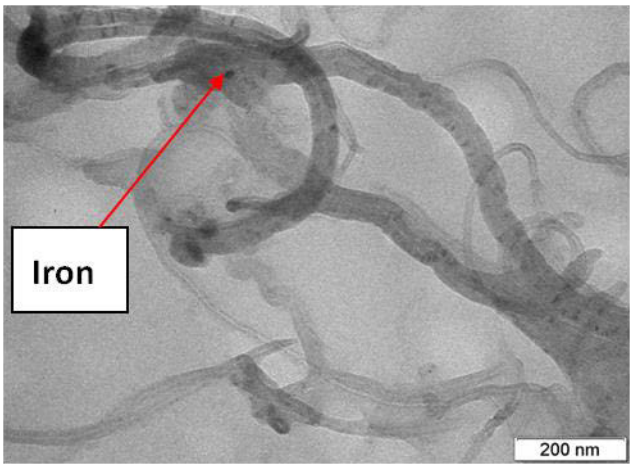

Figure 4.5: Representative TEM image for pristine MWCNTs

The results showed that a large percentage (39%) of the pristine MWCNTs had an outer diameter (OD) between 16-25 nm (see **Figure 4.6**).

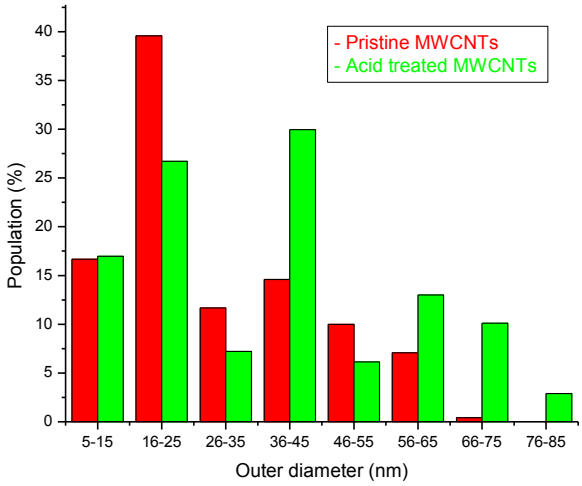

Figure 4.6: A comparison of the outer diameter distribution for pristine and acid-treated MWCNTs

A fairly good uniformity of diameters was observed in the pristine MWCNTs. The average OD of pristine MWCNTs was 30 ± 15 nm. On acid treatment (see **Figure 4.6**), the fraction of MWCNTs with ODs between 36 and 45 nm increased from 15% to 30%, and in general the tubes increased in OD. The average OD after acid treatment was 34 ± 16 nm. This is best

explained by the hydrochloric acid purifying mechanism reported by Fan *et al.*[2] which states that hydrochloric acid attack MWCNT defective sites causing expansion of tube walls followed by peeling off. Therefore, since hydrochloric acid was part of the acid treatment mixture that means the ultrasonic treatment was too mild to cause peeling off after expansion. Furthermore, the nitric acid treatment also debundled the MWCNTs so that a greater variety of MWCNT diameters were obtained causing a decline in homogeneity of the MWCNTs.[22] TEM results correlated well with both the crystalline quality and thermal stability results discussed in the subsequent sections (see **sections 4.4.1** and **4.5**). For example, R ($\frac{I_D}{I_G}$, i.e. the ratio of the Raman D band to G band, see **section 2.7.2**) increases while thermal stability decreases on acid treatment. This may be explained by slight roughening of the tube walls (see **Figure 4.7**). This observation is in agreement with the work of Scalese *et al*.[23] However, not all tube walls were roughened.

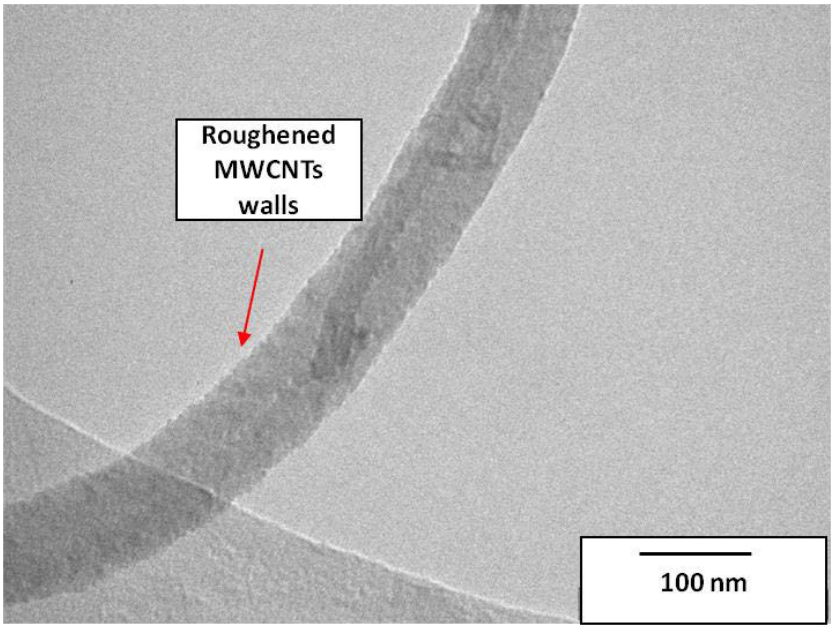

Figure 4.7: Representative TEM image for acid-treated MWCNTs showing the resulting roughening of the tube walls

All the nanocomposites from the sol-gel method (see **Figures 4.8** and **4.10**) showed particulate titania on the tubular MWCNT walls although the degree of coating was strongly influenced by wt.% ratios.[12] With an increase in titania, the coating became more uniform

and the coverage of the MWCNT tube walls more continuous. This observation was in strong agreement with the report by Vincent *et al.*[24] in that the MWCNT surface is a preferred site of titania crystallisation.

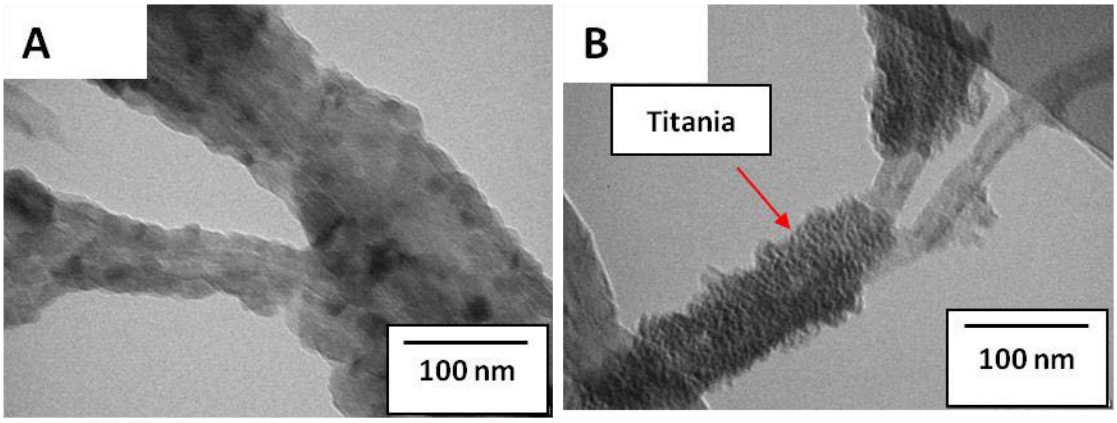

Figure 4.8: Representative TEM images for MWCNT-titania nanocomposites synthesised by the sol-gel method at (**A**) 5 and (**B**) 10 wt.% of MWCNTs

In the nanocomposites with low wt.% of MWCNTs, i.e. high titania wt.% (a representative sample is 10 wt.% MWCNTs) the most frequent OD range shifted to 26-35 nm (see **Figure 4.9**) for both methods. The CVD method seems to be coating smaller diameter MWCNTs pretty well since the OD range of 5-15 nm and that of 16-25 nm decreased in frequency from 17% to 0% and 27% to 5% respectively (see **Figure 4.9C**). A similar trend is seen in the sol-gel method where the 5-15 nm frequency decreased from 17% to 3%, although the most significant drop was in the 36-45 nm range, i.e. from 29% to 12% (see **Figure 4.9C**). CVD nanocomposites were thicker than those by the sol-gel method. However, the CVD method gave some tubes with ODs above 95 nm, i.e. 22%, which was far more than twice the OD of uncoated MWCNTs (see **Figure 4.9**). This was due to more than one tube being clustered together as a bundle, i.e. two MWCNT tubes were coated together with titania in some instances (see additional information in **Figure G2**, **Appendix G**). The changes in population of diameter ranges showed that the CVD method gave better coatings than the sol-gel method although the coating thickness was spread over a wider range (see **Figure 4.9B** and **C**).

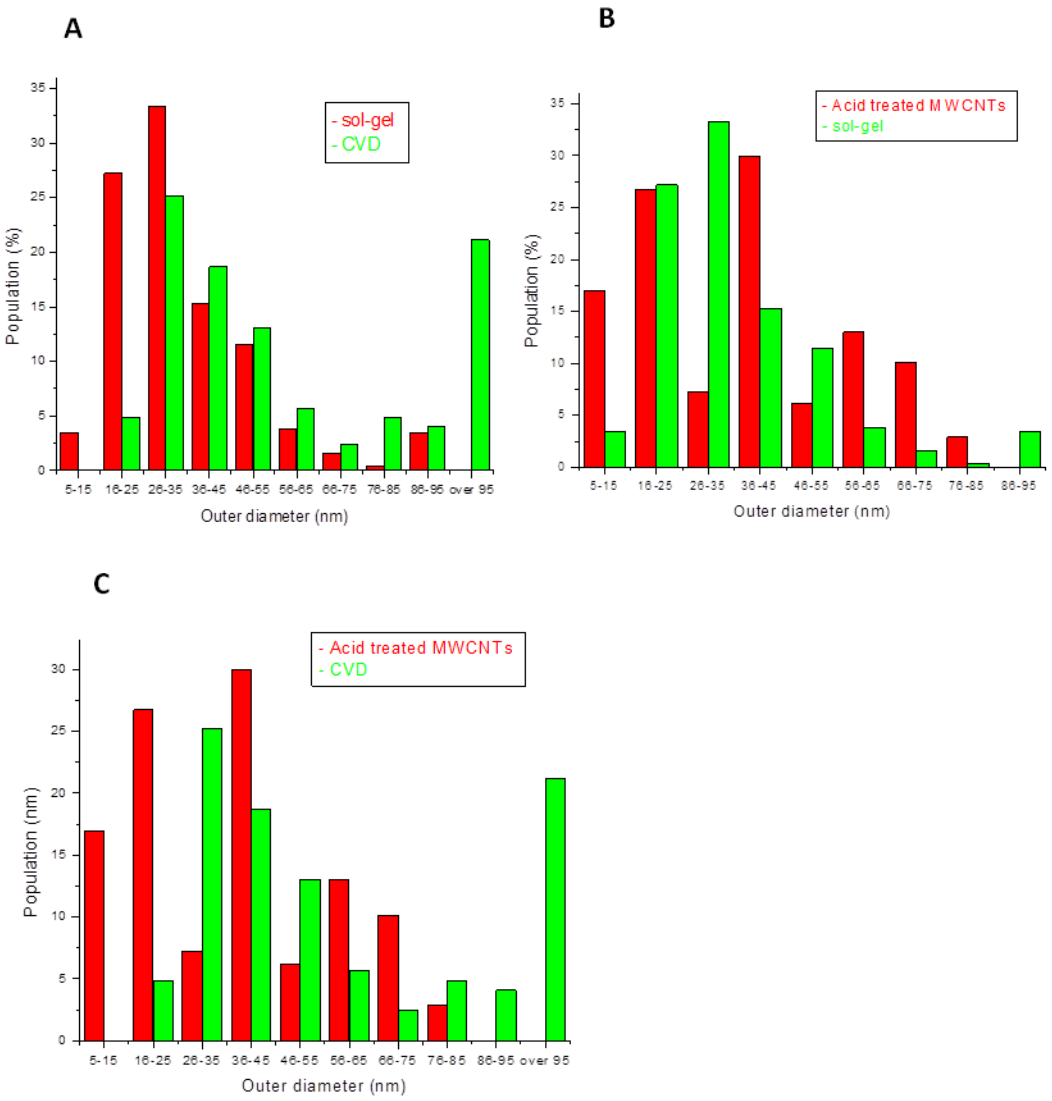

Figure 4.9: Distribution of MWCNT outer diameters in MWCNT-titania nanocomposites containing 10 wt.% of MWCNTs. Comparison of: (**A**) sol-gel and CVD methods, (**B**) before and after sol-gel coating, and (**C**) before and after CVD coating

At high wt.% of MWCNTs, i.e. low titania wt.%, represented by the 90 wt.% MWCNT samples (see **Figures 4.10** and **4.12**) from both methods, the dominant OD ranges were the 26-35 nm (25%) and 36-45 nm (35%) ranges for the CVD method and 16-25 nm range for the sol-gel method (see **Figure 4.11**). According to these observations, it may suggest that the sol-gel method is a better method of loading low wt.% titania onto MWCNTs because it gave a narrower distribution of MWCNT outer diameters.

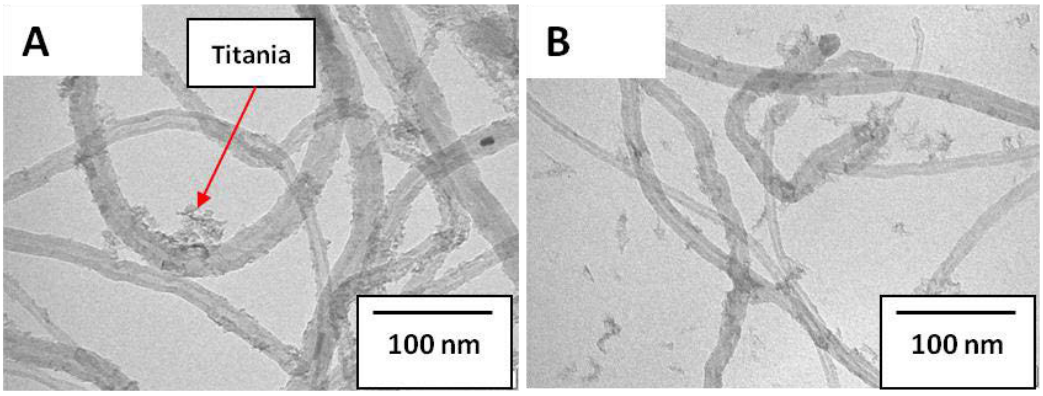

Figure 4.10: Representative TEM images for MWCNT-titania nanocomposites synthesised by the sol-gel method at (**A**) 90 and (**B**) 80 wt.% of MWCNTs

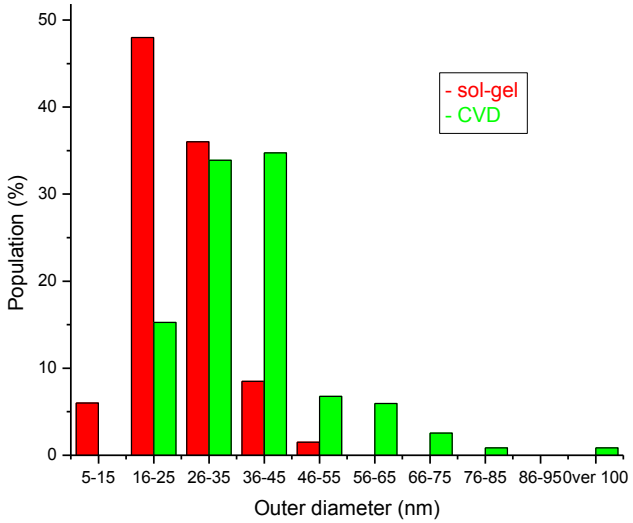

Figure 4.11: A comparison of the MWCNT outer diameter distribution for MWCNT-titania nanocomposites at 90 wt.% of MWCNTs by the sol-gel and CVD synthetic methods

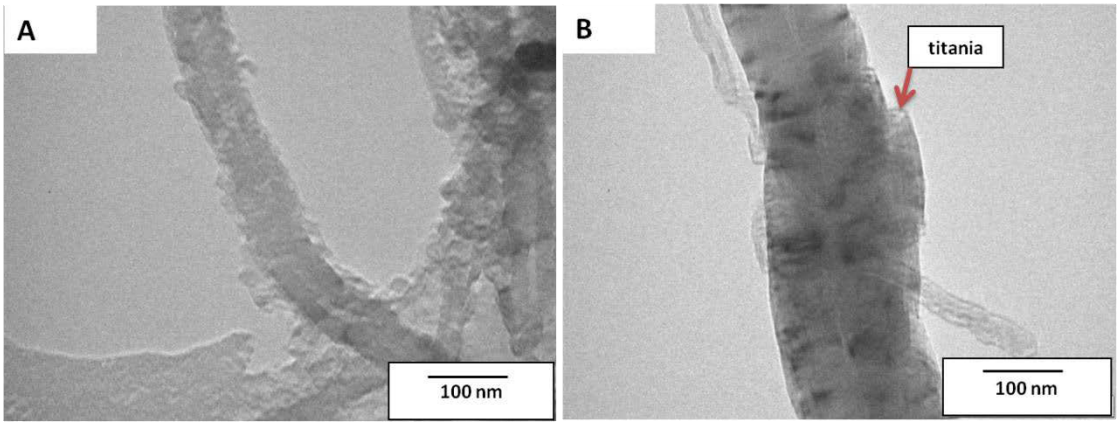

Figure 4.12: Representative TEM images for MWCNT-titania nanocomposites synthesised by the CVD method at (**A**) 90 and (**B**) 80 wt.% of MWCNTs

The coating on the nanocomposites with low wt.% of MWCNTs from the CVD method had more uniform coatings than those from the sol-gel method (see **Figures 4.8** and **4.13**). Furthermore, some tubes from CVD method were completely covered. The nanocomposites from CVD method tend to move towards a honeycomb structure[25] on crossing over from high to low MWCNT wt.% (see **Figures 4.12** and **4.13**).

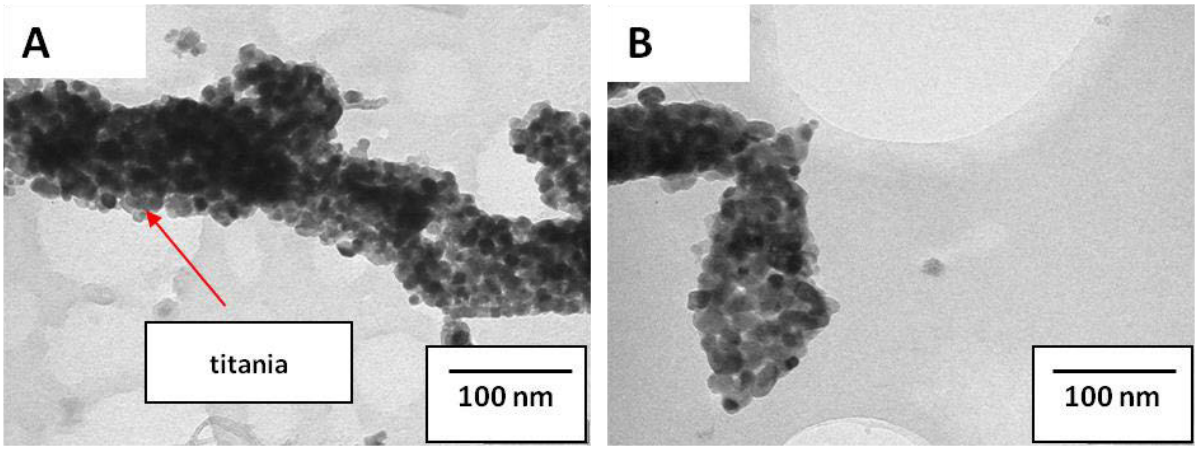

Figure 4.13: Representative TEM images for nanocomposite synthesised by CVD method at (**A**) 5 wt.% and (**B**) 10 wt.% of MWCNTs

While most researchers, such as Gao *et al.*[15] used surfactants, for example sodium dodecylsulfate, to coat MWCNTs, this work shows that a comparable coating can be

achieved without the use of surfactants. TEM images from similar nanocomposites reported in literature (see **Figure 2.8** in **Chapter Two, section 2.7.4**) were comparable to the CVD-loaded nanocomposites reported were especially at high wt.% of MWCNTs. At high wt.% of MWCNTs a thin layer on the tube walls was observed in both methods.[27] HRTEM images for the CVD and sol-gel methods at 5 wt.% MWCNTs are shown in **Figure 4.14A** and **B** respectively at different magnifications to show the topography of the individual MWCNTs in the MWCNT-titania nanocomposites.[22]

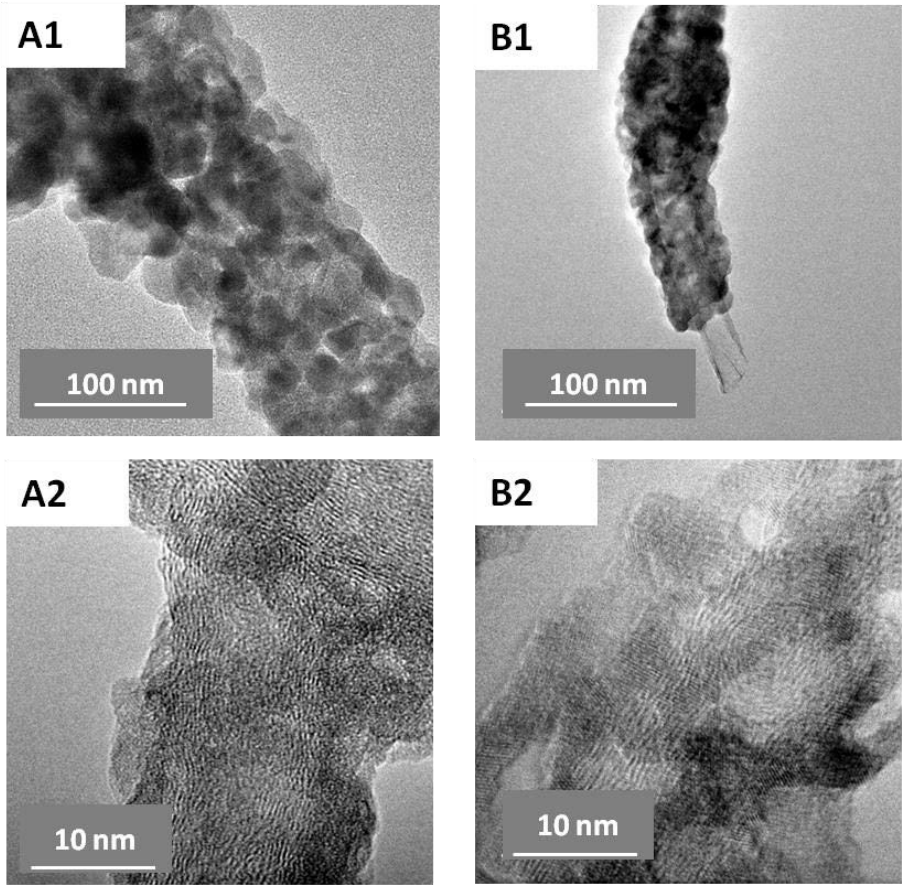

Figure 4.14: Representative HRTEM images at different magnifications for MWCNT-titania nanocomposites containing 5 wt.% of MWCNTs synthesised by the CVD (**A1** and **A2**) and sol-gel methods (**B1** and **B2**)

The titania lattice fringes (ca. d spacing of 0.35 nm) on the MWCNT walls for both synthetic methods are observed. However, the coating from the CVD method (see **Figures 4.14**, **A1**

and **A2**) was better because it completely covered the MWCNTs. This is in concordance with the TEM observations. In the sol-gel method some parts of the MWCNTs were bare whilst some were thickly covered (see **Figures 4.14**, **B1** and **B2**) and this is in agreement with observations by Korbély *et al.*[17] This further suggests that the CVD method is better than the sol-gel method. These results can be attributed to the vacuum effect on titania deposition in the CVD method. Furthermore, it can be seen that the MWCNTs exhibit a curved texture due to defective graphene sheets[1] in the nanocomposites from both methods (see **Figures 4.14A2** and **G1** in **appendix G**).[22] From the TEM analysis it can be seen that titania caused changes in the morphology and diameters of the MWCNTs.[14] Also, the mass ratio influenced the ultimate morphology of the nanocomposite, i.e. a change from isolated titania particulates to a uniform coating of titania on the MWCNTs with an increase in the titania wt.% (see SEM, TEM and HRTEM in **Figures 4.2**, **4.3**, **4.8**, **4.10**, **4.13** and **4.14**). This is in agreement with work reported by authors such as Aman *et al.*[12]

4.3 Functional groups and bonding within nanocomposites

This FTIR spectroscopy was used to investigate the functional groups and bonding between components in the nanocomposites. **Figure 4.15** shows a representative spectrum of the nanocomposites.

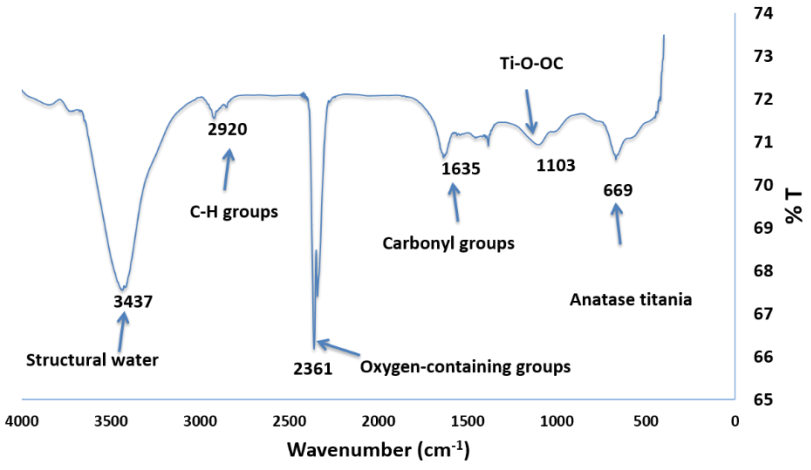

Figure 4.15: Typical FTIR spectrum for the MWCNT-titania nanocomposites synthesised either by the sol-gel or CVD methods

The peak at ca. 1635 cm^{-1} was observed in all the nanocomposites from both methods and was assigned to carbonyl groups in the MWCNT framework.[28,29] The FTIR peaks at 2738.31 cm^{-1} and 2839.25 cm^{-1} in the pristine and acid-treated MWCNTs respectively is assigned to C-H bond.[30,31] This peak correlates with the in-plane C-H deformation peak observed in the Raman analysis (see **section 4.4.1**). The new peaks at 2327.62 cm^{-1} and 2329.14 cm^{-1} that appeared after acid treatment of the MWCNTs (see additional information in **Figure H1** in **Appendix H**) can be assigned to oxygen-containing functionalities introduced onto the tube walls during the acid treatment, i.e. C-O , C=O and COO groups.[24]

In nanocomposites with high wt.% of MWCNTs by the sol-gel method, one of the peaks at circa (ca.) 2330 cm^{-1} disappears first (see additional information in **Figure H1** in **Appendix H**) and this agrees with the views by Stobinski *et al.*[21] in that surface groups on MWCNT walls are active sites for further functionalization. However, these peaks were present at high titania wt.% nanocomposites synthesised by the sol-gel method. In the CVD, the peak at 2342 cm^{-1} disappears in the same way as the peak at 2330 cm^{-1} in the sol-gel method. On the other hand, both peaks at ca. 2342 cm^{-1} and 2361 cm^{-1} disappear in nanocomposites with high wt.% MWCNTs produced by the CVD method. The preferred site for titania coating (see **section 4.1**) can be explained with the aid of observations above especially at low wt.% of titania. The hydrogen bonds due to the oxygen-containing functionalities on the walls of the MWCNTs are disrupted when the titania wt.% increases. This is in agreement with the views of Korbély *et al.*[17] in that oxygenated groups stimulate coverage and therefore enhance the degree of coating.

Furthermore, the peak due to C-H stretching is also absent in the nanocomposites containing more than 10 wt.% of MWCNTs. The peak at 3427.40 cm^{-1} is assigned to OH groups from the water molecules and/or carbonyl groups.[21,29] It was observed in all nanocomposites and increases with an increasing amount of TiO_2. This is in agreement with the TG analysis which showed a slight water loss at ca. 100 ^{o}C. This is explained further in **section 4.5**. **Table 4.1** summarises the important chemical moieties identified within the nanocomposites.

Table 4.1: FTIR absorption peaks exhibited by the nanocomposites obtained from both synthetic methods

Peak /cm^{-1}	Assignment
3437	OH groups from structural water
2920	C-H stretching
2361	Oxygen-containing groups
2342	hydrogen bond between OH groups
1635	MWCNT carbon groups
1110	Ti-O-O-C
669	Anatase Ti
577	Anatase Ti
411	Anatase Ti

In all nanocomposites, as the titania wt.% increased a new peak appeared at ca. 600 cm^{-1}. This peak was assigned to the anatase phase of titania.[14] The Ti-O-C covalent bond[14] was observed at ca. 1110 cm^{-1} and this correlated with the phase observed in the Raman results presented in the **section 4.4.1**. This observation is similar to the key views presented by Li *et al.*[14] In their work they suggested that titania was covalently linked to the MWCNTs. Therefore, in this work titania was covalently linked to the MWCNT in the nanocomposites synthesised by the two methods. The covalent link between titania and the MWCNTs facilitates stable energy conversions and strong interfacial interactions[2] vital for DSSC applications. Both methods show isolated deposits on the walls of the MWCNTs at high wt.% of MWCNTs (see **Figures 4.2** and **4.3**).

4.4 Crystallinity and phases

The crystallinity and titania phases present in the nanocomposites synthesised in this work were investigated by means of Raman spectroscopy and powder X-ray diffraction.

4.4.1 Vibrational-based characteristics

Generally all Raman spectra (representative spectra in **Appendix D**) had the peaks at ca. 810 and 1030 cm^{-1}. These peaks may be assigned to the lower energy radial breathing mode of MWCNTs[35] and the in-plane CH deformation respectively.[30] The position of the radial breathing mode was outside the range reported by some authors such as Scalese *et al.*[23] (100-500 cm^{-1}). This is because they used a different excitation wavelength of the Raman laser.[23] The in-plane CH peak correlated with FTIR observation of the C-H functional group in the nanocomposite. Peaks at ca. 2300 and 2400 cm^{-1} were present in all nanocomposites. The peaks are assigned to the first overtone of D mode (G') and combination mode of the D and G modes respectively.[22,23,30,36] Pristine MWCNTs had peaks at 632 cm^{-1}, 702 cm^{-1}, 924 cm^{-1} and 1149 cm^{-1} which could have been due to inner most diameter[23] impurities such as iron because they disappeared on acid treatment. It should be noted that the scope of the study was mainly from acid-treated MWCNTs.

Acid treatment slightly up-shift the D band position towards the graphite position (1350 cm^{-1}) and a downshift of about 37 cm^{-1} is observed on the G band (see **Table 4.2**). Li *et al.*[26] suggest this could be due to oxygen-containing functionalities' strain on MWCNT walls. Fan *et al.*[2] reported that such a downshift is due to polygonal and less cylindrical structural defects on the MWCNT surface as well as increasing diameter. TEM and Raman spectroscopy agrees in this regard.

As titania wt.% increased new peaks appeared at around 630 cm^{-1}, 514 cm^{-1} and 396 cm^{-1} (see additional information in **Appendix D**). All these peaks can be assigned to E_g, A_{1g} + $B_{1g(2)}$ and $B_{1g(1)}$ modes respectively for anatase phases of titania.[7,28,34] The decrease in width for both D and G bands peaks agrees with findings by Osswald *et al.*[35] However, the acid treatment tends to introduce more defects since the I_D/I_G (R) value increased from 0.5112 to

0.9028. This result was contrary to the findings by Rinaldi *et al.*[1] in that the R value decreased on ultrasonic treatment due to removal amorphous carbon.

Table 4.2: Comparison of D and G bands for pristine and acid-treated MWCNTs obtained from the Raman spectroscopy

Sample	D band		G band		I_D/I_G
	Position	Width	Position	Width	
Pristine MWCNTs	1347.2	60.996	1595.6	88.865	0.5112
Acid-treated MWCNTs	1350.6	44.741	1558.0	10.740	0.9028

This trend is not expected in the MWCNTs used in this work because the TG thermogram presented in **Figure 4.18** does not show presence of substantial amount of amorphous carbon. The decrease in R value may imply the decline in crystallinity and introduction of defects onto MWCNTs from acid treatment. The main impurity was the Fe catalyst as indicated by the TGA residue in correlation with EDX and TEM (see **Figures 4.21** and **4.5**). The encapsulated catalyst was difficult to remove without compromising the multi-shell sp^2 hybridised carbon structures constituting the walls.

General trend was observed to be upshift of the G band position by about 32 cm^{-1} on loading titania which is almost equal to the initial downshift by the acid treatment of MWCNTs (see additional information in **Table D1** to **D4** in **Appendix D**). This is due to titanium metal strain on C-C bonds.[26] G band shift could also, have been introduced by a wide range of tube sizes, varying defect density, tube bundling and rough sample surface due to the coating process also observed by TEM and HRTEM images (see **Figures 4.5-4.19**).[35] No significant change on width of the D band (see additional information in **Table D1** to **D2**, in **Appendix D**) may be deduced from the Raman data but G band generally tends to increase with an increase in titania wt.% in the sol-gel method. On the contrary, G band width tends to decrease with an increase in MWCNTs ratio in the nanocomposite by the CVD method (see additional information in **Appendix D** and **Table D4**) but no noticeable trend was observed on the D band. No noticeable effects were observed in nanocomposites

with high MWCNTs wt.% by the CVD method, i.e. low titania wt.% ratios (see additional information in **Appendix D**, **Table D3**).

While authors such as Delhaes *et al.*[23] reported that the G band of MWCNT is narrower than the D band, additional data in **Appendix D** shows an opposite trend. Peak broadening in Raman spectroscopy is influenced by temperature, excitation wavelength and crystalline nature of the nanomaterials. Hence, this was the source of the differences of this work and their work. The results from this work concurred with report by Stobonski *et al.*[21] in that peak width of the G and D bands of the MWCNTs depends on their electrochemical environment and experimental parameters.

The spectrum was re-plotted, the bands were fit into Lorenztian curve and no other corrections were done using the Origin software. The I_D/I_G ratio (R) was calculated by using the area under the D- and G-band peaks respectively. The R value decreased from that of acid-treated MWCNTs in the nanocomposites (see **Figure 4.16** and **Table 4.2**). This may imply that titania seats on the MWCNTs defects introduced during the acid treatment. This observation agreed with the work reported by Li *et al.*[14] where reduction in R value was attributed to calcinations. Furthermore, R value (see **Figure 4.16**) for most nanocomposites was comparative to the range reported by Osswald *et al.*[35] In **Figure 4.16**, low wt.% MWCNTs (5-20 wt.% of MWCNTs) by the sol-gel and CVD methods, R values increased with an increase in wt.% of MWCNTs. A similar trend in R was also observed in nanocomposites with high MWCNTs wt.% (5-20 wt.% of MWCNTs). It is also seen in **Figure 4.16** that nanocomposites by the CVD synthetic method had smaller R value than those by sol-gel except at 95 wt.% of MWCNTs. According to this observation it may be suggested that CVD method gave less defective and more crystalline nanocomposites than sol-gel method. This is in agreement with powder XRD results in **section 4.4.2**.

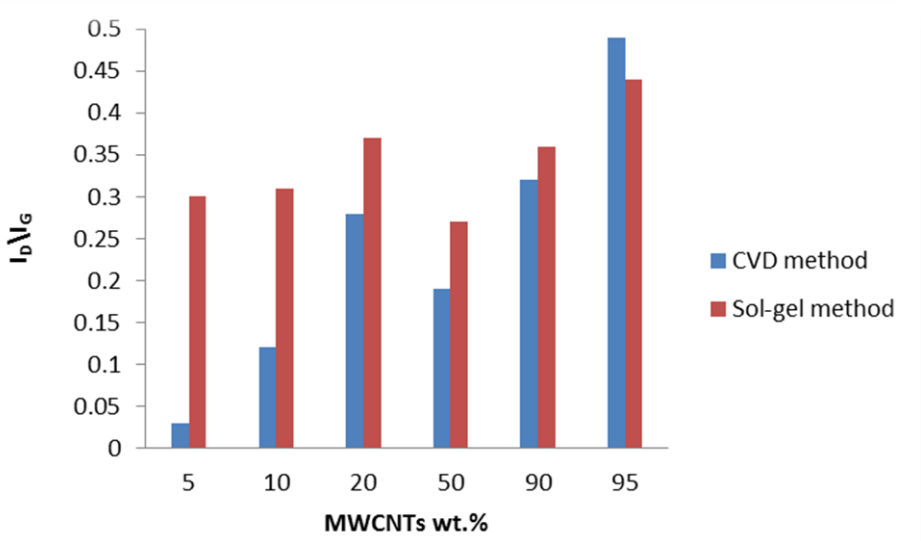

Figure 4.16: Comparison of the I_D/I_G ratio of the nanocomposites by the sol-gel and CVD synthetic methods

4.4.2 Crystal structures and phases

The XRD results are presented in **Figure 4.17** and **Table 4.3** gives representative spectra. The XRD analysis shows that intensity of the main peaks of the MWCNTs increased by the acid treatment (see additional information in **Appendix B**). This may imply that acid treatment increased crystallinity degree of the MWCNTs.[37] This is in agreement with a number of characterisation techniques, i.e. SEM, TEM and HRTEM results, TGA residual mass decrease and shape of the residual TG curve, Raman spectroscopy peaks that disappeared at 630, 702, 924 and 1149 cm^{-1} on acid treatment. The peaks observed from powder XRD analysis for pristine MWCNTs and after acid treatment include Miller indices (h k l) assigned to 002, 100 and 004 for 2 θ of 25.9°, 42.5° and 53° respectively. MWCNT peaks were not observed in nanocomposites with high titania wt.% ratios (see **Figure 4.17**). The XRD results corroborate the views of many researchers such as Cong *et al.*[37] in that anatase phase (with h k l index of 101) overlapped with the MWCNTs plane characteristic peak (with h k l index of 002). This has been explained due to similar crystal inter-planer spacing, d spacing reported to be 0.35 nm for the anatase phase titania and 0.34 nm for the MWCNTs.[37,38] **Table 4.3** gives the assignment of peaks at 2θ angles to various Miller indices. According to the peaks in the diffractogram, the only phase of titania in the nanocomposites was anatase.[17] It should be noted that both methods gave similar XRD spectra.

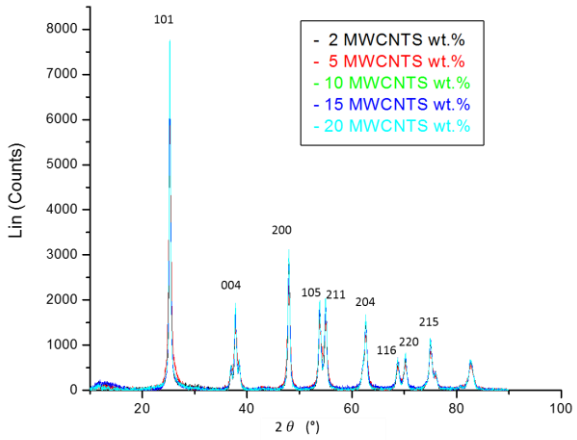

Figure 4.17: XRD spectra for MWCNT-titania nanocomposites with high titania wt.% synthesised by CVD method

Table 4.3: The assigned 2θ angles for anatase titania and MWCNTs in MWCNT-titania nanocomposites synthesised by the sol-gel and CVD synthetic methods

2θ/°	(h k l)
26.2	(101) titania and MWCNTs overlap
42.1	(100) MWCNTs
44.1	(101) MWCNTs
54.1	(105) MWCNTs
38	(004) Anatase Titania
48.1	(200) Anatase Titania
55	(211) Anatase Titania
63	(204) Anatase Titania
68.8	(116) Anatase Titania
70.3	(220) Anatase Titania
75	(215) Anatase Titania

The nanocomposites by the CVD synthetic method at low wt.% of MWCNTs were observed to have sharper peaks than at high wt.%. This may imply that crystallinity of titania decreased with an increase in wt.% of MWCNTs in the CVD synthetic method.

The diffractogram at high wt.% of MWCNT shows that nanocomposites from sol-gel method had less symmetrical peaks and broader peaks. Furthermore, the nanocomposites with high titania wt.% by the sol-gel synthetic method had less intensity values, broader and less symmetrical peaks than CVD. In addition, if TEM images from **Figure 4.13** and **4.8** from similar MWCNT:titania ratios are compared, it is seen that titania aggregates on MWCNT wall are bigger in nanocomposites by the CVD than sol-gel method. According to the diffractogram obtained, it can be suggested that nanocomposites synthesised by the sol-gel synthetic method are less crystalline than those by the CVD (see additional information in **Appendix B**, **Figures B2**-**B3**).[37] This observation concurred with the deductions from the smaller values of R in CVD method nanocomposites except at 95 wt.% MWCNTs relative to sol-gel method (see **Figure 4.16**). This is due to the heat treatment[17,22,23] involved in the CVD synthetic method even though nanocomposites from sol-gel also involved calcining, the period was shorter. Li *et al.*[14] reported intensity of anatase diffraction to increase with an increase in titania coating ratio and this was in agreement with the observations in this work from both synthetic methods.

4.5 Thermal stability

The thermal stability behaviour of the nanocomposites was deduced from TGA and analysing the first derivative curves of the change in wt.% against temperature (see **Figures 4.18-4.21** and **Table 4.4)**. TGA was also used as a quality control technique, i.e. checking the presence of other forms of carbon from the titania precursors in the final MWCNT-titania nanocomposite and checking for catalyst remnants from MWCNTs. From the TG data obtained, the MWCNTs showed no loss below 200 °C indicating that minimal if any water and amorphous carbon were present.[26] The pristine MWCNTs were 95% pure as indicated by the supplier (see **Figure 4.18**). The thermogram obtained indicated that acid treatment reduced the iron content to almost zero (see **Figure 4.18**). This, is also, shown by the difference in the shapes of the thermograms in the residual region for pristine and acid-treated MWCNTs. The thermogram for pristine MWCNTs shows an increase in mass (inclined TG curve, see **Figure 4.18**) indicating an increase in mass due to a substantial formation of iron oxide but that effect was absent in the thermogram of the acid-treated

MWCNTs. This correlated with the results presented on TEM images, i.e. encapsulated iron in MWCNTs (see **Figure 4.5**) and the qualitative analysis (see **section 4.7.1**).

A decrease in the thermal stability of pristine MWCNTs was observed after acid treatment (see **Figure 4.18**). The slight decrease in thermal stability was due to compromise of the MWCNT walls from the introduction of oxygen containing functional groups and slight defects observed in typical TEM images (see **Figure 4.7**) which decrease oxidative stability.[32] This observation is in agreement with the report by Lehman *et al.*[33] that states that carboxylic acid functional groups on MWCNTs reduce their thermal stability.

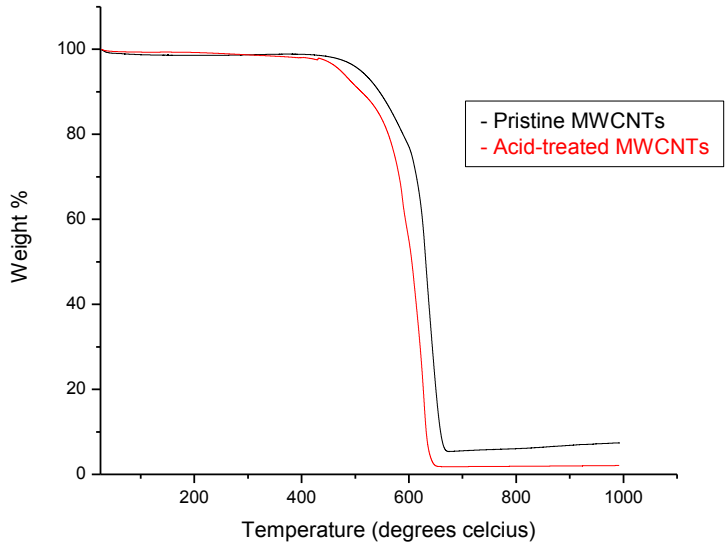

Figure 4.18: Comparison of the TG thermograms for pristine and acid-treated MWCNTs

Generally, in this work the decomposition temperature range for MWCNTs was between 450 and 620 °C. This range was within the range reported by Li *et al.*[26] Nanocomposites with low wt.% of MWCNTs, i.e. high titania wt.% ratio, showed a weight loss below 200 °C even though the nanocomposites were dried overnight in an oven prior to the analysis and weight loss increased with increase in titania wt.% (see **Figure 4.19**). This correlated with the structural water[27] peak observed in FTIR spectroscopy. The residual amount in **Figure 4.19** was fairly close to the wt.% of titanium obtained by ICP-OES analysis of the composite.

The slight variation could possibly arise from the residual iron introduced as a catalyst in the MWCNT synthesis.

Thermogram at high wt.% of MWCNTs ratio were steeper than at lower ratios and this may indicate a higher purity level of MWCNTs in the nanocomposites at high MWCNTs ratios (see **Figure 4.19** and **Table 4.4**). Furthermore, at low wt.% of MWCNTs, i.e. higher wt.% of titania, thermal stability of MWCNTs decreased (see **Table 4.4**). Titania may act as a catalyst aiding thermal destruction of MWCNTs.[34]

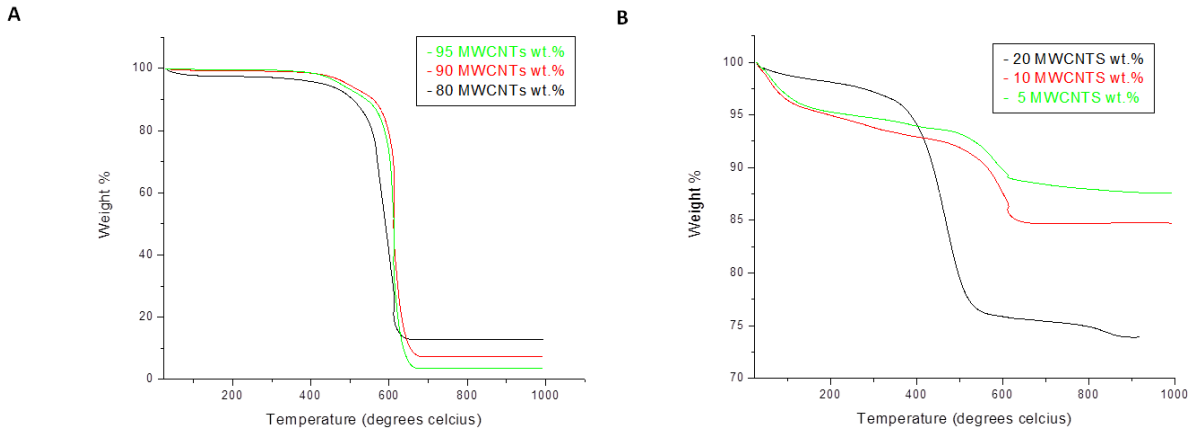

Figure 4.19: Comparison of thermogram for MWCNT-titania nanocomposites synthesised by sol-gel method at (**A**) high and (**B**) low MWCNTs wt.%

No clear trend in thermal stability was observed (see **Table 4.4**) even though a decrease was expected since Raman spectroscopy showed that MWCNTs defects decreased with increase in titania wt.% (see **section 4.4.1**). MWCNTs in the nanocomposites with high titania wt.% ratios synthesised by CVD method were more thermally stable than sol-gel method (see **Table 4.4**). This implies a higher graphitic nature of MWCNTs in the nanocomposites. However, thermal stability was seen to decrease with increase in wt.% of MWCNTs ratio. On the contrary, MWCNTs thermal stability was seen to decline from that of acid-treated MWCNTs (see **Table 4.4**) on increasing titania wt.% in the nanocomposites with high MWCNTs ratio.

Table 4.4: Thermal stability temperatures for nanocomposites by the sol-gel and CVD methods

MWCNTs wt.%	Maximum decomposition temperature /°C	
	Sol-gel	CVD
5	607.5	683.7
10	558.5	635.5
20	596.9	630.6
80	610.0	597.7
90	608.7	599.0
95	604.4	624.2

Similar thermogram was obtained for nanocomposite synthesised by CVD method (see **Figure 4.20**). However, no weight loss was observed below 200 °C. This can be attributed to synthetic method which eliminated water using the vacuum system and high temperatures involved.

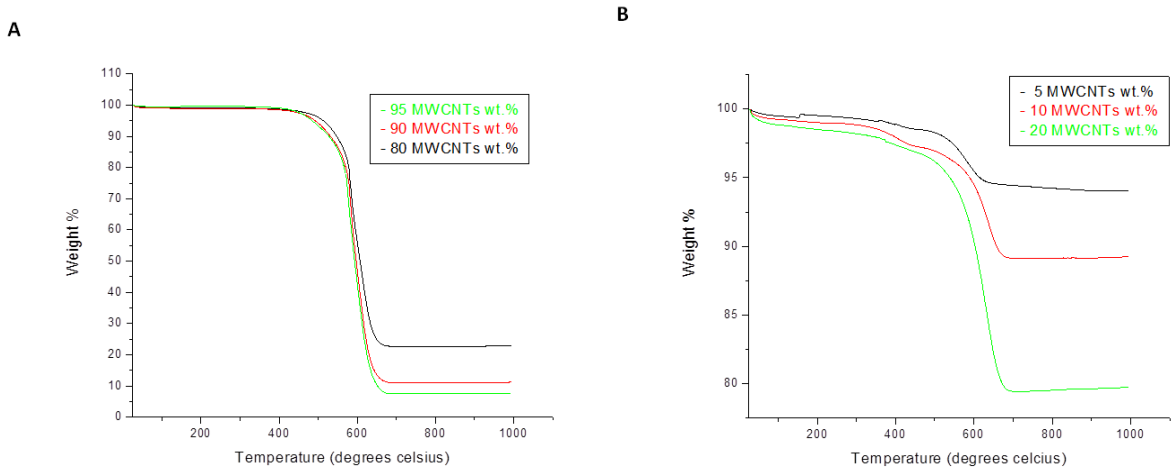

Figure 4.20: Comparison of thermogram for MWCNT-titania nanocomposites by the CVD synthetic method at (**A**) high (**B**) low MWCNTs wt.%

A comparison of nanocomposites from the sol-gel and CVD methods at 20 wt.% of titania (see **Figure 4.21)** shows that nanocomposite by the CVD method is more thermally stable and had no loss of water below 200 °C. A similar comparison at 20 wt.% of MWCNTs (see **Figure 4.21**), also shows that nanocomposites by the sol-gel synthetic method are less thermally stable but the difference was largely pronounced. According to these results, it is seen that the method of synthesis and ratios of components of the nanocomposites has an effect on overall thermal stability of the MWCNTs in nanocomposites. It is also seen in this work that the nanocomposites from CVD method were more thermally stable than those from sol-gel method despite the wt.% ratios of components. The results on thermal stability are explained well with reference to **Figures 4.2**, **4.3**, **4.8** and **4.13**. In these Figures, it is seen that the titania coat was less uniform with more bare MWCNTs in nanocomposites by the sol-gel than by CVD method. The titania coat on MWCNTs could have limited movement of oxygen to the surface of the MWCNT and thus slow down the MWCNT decomposition. From the thermograms, a correlation with ICP-OES titanium values is seen on the overall titania wt.% ratios in the nanocomposites. According to the thermogram (see **Figure 4.21A** and **B**), titania wt.% in nanocomposites by the CVD synthetic method were closer to the targeted wt.% than those by sol-gel.

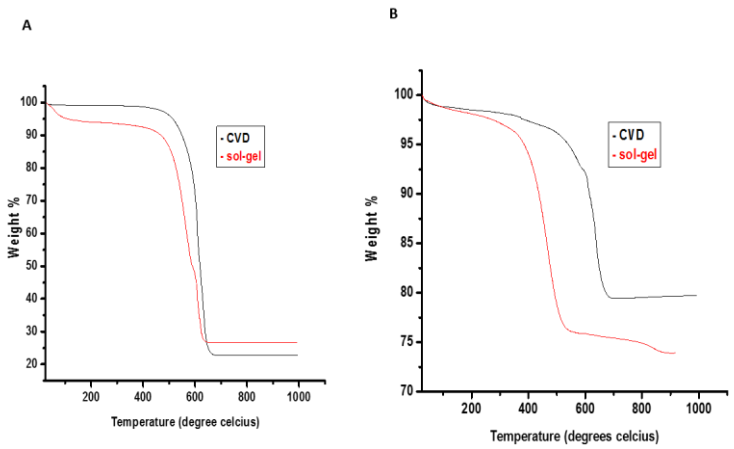

Figure 4.21: Comparison of the TG thermograms for MWCNT-titania nanocomposites by the CVD and sol-gel synthetic methods at MWCNTs wt.% of (**A**) 80 and (**B**) 20

4.6 Surface area and porosity

Textural characteristics of MWCNT-titania nanocomposites determined by means of fitting isotherms into the BET equation from sol-gel and CVD prepared samples are shown in **Table 4.5**. The highest surface area (328 m^2g^{-1}) was observed at 90 wt.% and 95 wt.% of MWCNTs (134 m^2g^{-1}) produced by sol-gel and CVD respectively.

Table 4.5: Comparison of textural characteristics of MWCNT-titania nanocomposites by the sol-gel and CVD synthetic methods

Titania wt.%	BET surface (m^2/g)		Pore volume (cm^3/g)		Pore size (nm)	
	Sol-gel	CVD	Sol-gel	CVD	Sol-gel	CVD
0 (MWCNTs)	143.15	143.15	0.50	0.50	13.98	13.98
5	149.80	134.82	0.52	0.46	13.93	13.67
10	128.56	100.53	0.54	0.49	16.72	19.87
40	284.44	105.03	0.39	0.48	5.44	18.44
50	188.79	26.82	0.22	0.11	4.73	15.99
60	185.70	76.85	0.37	0.38	7.95	19.80
80	108.11	71.27	0.19	0.34	6.88	19.32
90	328.21	62.59	0.21	0.29	2.57	18.32
95	135.36	38.08	0.10	0.21	2.93	21.80
100 (titania)	7.16		0.03		16.12	

The MWCNTs seems to increase the surface area of titania in both synthetic methods. Similar results were previously reported by Li *et al*.[14]

However, nanocomposites prepared by the CVD have smaller surface areas than those produced by the sol-gel method. From the TEM images (see **section 4.2**) the titania coat was seen to be thicker in nanocomposites by the CVD method than those by the sol-gel. This observation bears the key views of Scalese *et al.*[23] In their work they reported that interfacial surface area is inversely proportional to MWCNT thickness. Since fitting of isotherms into the BET equation gives total surface area and cannot discriminate between components,[17] a decrease in surface area in one component affect the total surface area. In addition to that, an agreement is seen on nanoparticle size, i.e. nanocomposites by the CVD had larger nanoparticle sizes (see **section 4.2**) and smaller surface areas than those by sol-gel method.

MWCNTs reduced size of titania nanoparticles in both synthetic methods. Zhang *et al.*[39] also suggested that post heat treatment reduces surface area of nanomaterials and therefore heat treatments involved in CVD method could have played a similar role. Even though the sol-gel method involved heat treatment, the period was shorter than the CVD. Nanocomposites by the sol-gel method had increased surface area, i.e. mostly greater than that of pristine MWCNTs and titania whereas nanocomposites by the CVD was far less than that of pristine MWCNTs (see **Table 4.5**). The sol-gel had the advantage of sonication during synthesis, this will help to debundle the tubes throughout, and will help increase the surface area. The two acids used, i.e. nitric and hydrochloric acid has opposing effects on surface area. Nitric acid opens capped MWCNTs thereby increasing surface area whilst the contrary is true for hydrochloric acid.[2,22]

The MWCNTs improved titania pore volume from 0.03 $cm^3 g^{-1}$ to a maximum of 0.54 $cm^3 g^{-1}$ at 10 wt.% of MWCNTs in the nanocomposites by the sol-gel synthetic method (see **Table 4.5**) and in general pore volume increased with an increase in wt.% of MWCNTs. The CVD nanocomposites followed a similar trend and the highest pore volume was 0.49 $cm^3 g^{-1}$ at 10 wt.% of titania. Addition of MWCNTs to titania by the sol-gel method generally decreased pore size but it tends to increase in nanocomposites by CVD (see **Table 4.5**). Both methods yielded porous nanocomposites (see additional information in **Appendix A**).

4.7 Elemental composition

Elemental composition analysis was done qualitatively and quantitatively by means of the EDX and ICP-OES respectively.

4.7.1 Qualitative analysis

EDX analysis was performed to confirm the presence of the expected elements; namely, titanium and carbon (see **Figure 4.22C**). The quantity of low atomic mass elements, i.e. carbon and oxygen, is often overestimated by this technique and it is therefore not suitable for actual quantification of wt.% ratios in the MWCNT-titania nanocomposites. [21]

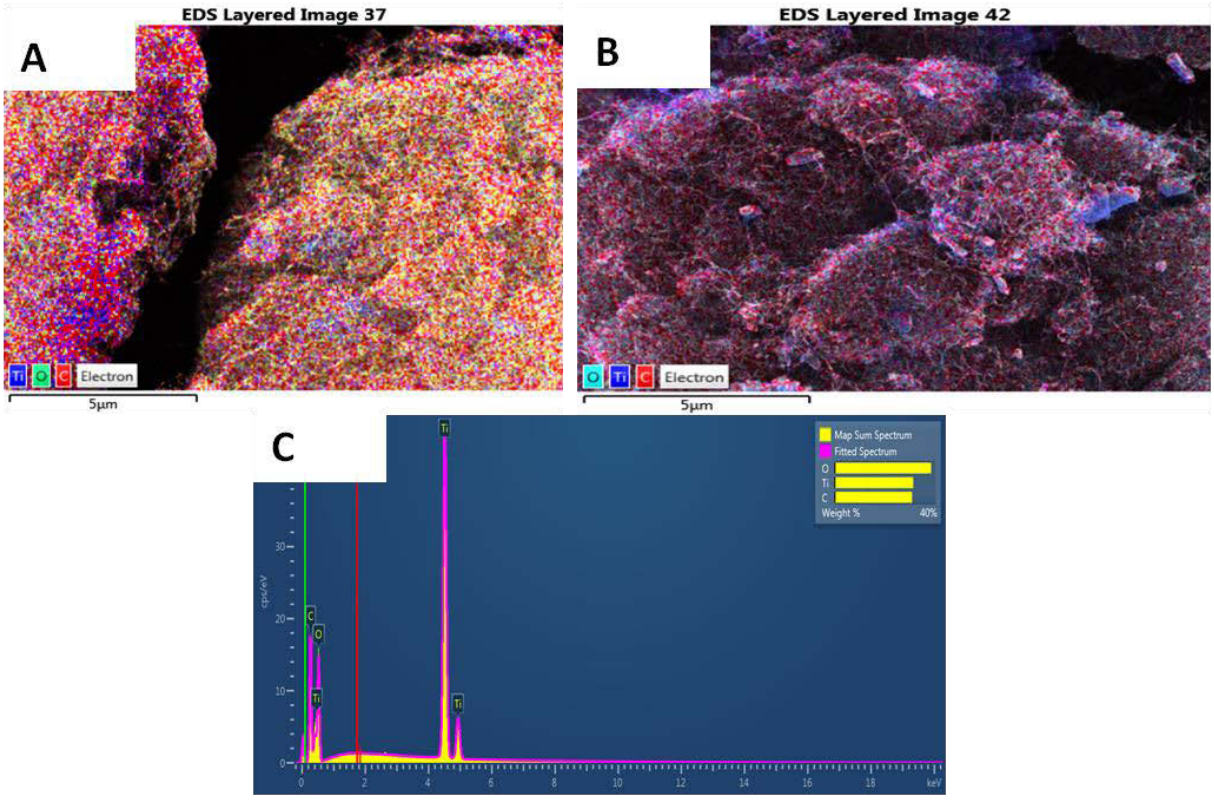

Figure 4.22: Representative mapping from the (**A**) sol-gel method and (**B**) CVD method, and (**C**) a representative EDX spectrum

Through EDX, some traces of iron were detected in some nanocomposites. This arises from the catalyst used in the synthesis of the MWCNTs. Also, the residue obtained from TGA was faint reddish and white in colour, indicating the presence of titania and iron. According to

the mapping from this technique, titanium, carbon and oxygen were present in a comparable distribution in the nanocomposites synthesised from both methods (see **Figures 4.22A** and **B**). The difference in the false colour image is an artefact of the system.

4.7.2 Quantitative analysis

Inductively coupled plasma-optical emission spectroscopy (ICP-OES) was used to quantitatively confirm the targeted titania wt.% for each nanocomposite prepared. The **Figure 4.23** shows the calibration curve of titanium standards used in the determination of titanium concentration in the MWCNT-titania nanocomposites. As can be seen, good linearity was achieved over the 2-10 mg L^{-1} concentration range. The titanium concentrations determined were then used to calculate the wt.% loadings on the MWCNTs.

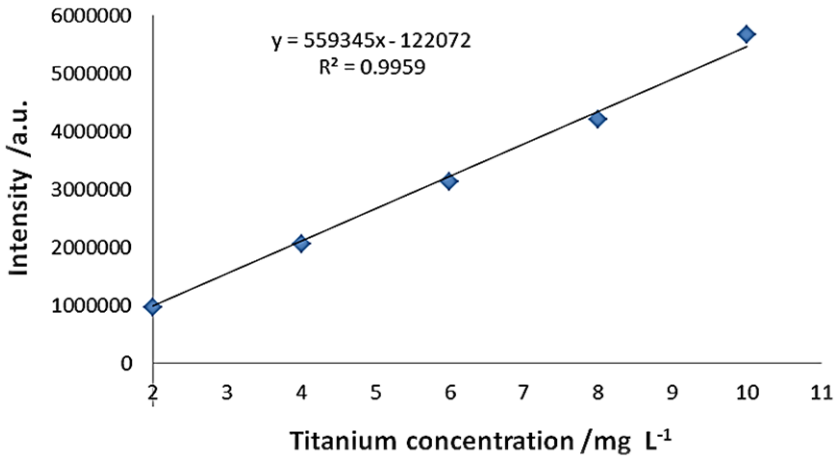

Figure 4.23: A typical calibration curve for the determination of the titanium concentration in the MWCNT-titania nanocomposites

The development of a suitable digestion method for the MWCNT-titania nanocomposites and deducing the titania wt.% was difficult as reported by Li *et al.*[14] This is because titanium is a refractory metal, i.e. cannot be solubilised by some acids or solvents. In this work, nitric/sulfuric acid mixture coupled with heating on a hot plate in the fume hood was used

to digest the MWCNT-titania nanocomposites. The digestion method gave good recovery of titania from the spiked activated carbon, i.e. 2.32, 5.21, and 9.66 wt.% for 2, 5 and 10 wt.% spiked titania respectively. The loaded titania was within the expected ranges (see **Table 4.6**) for both methods. For example, for a targeted 50 wt.% titania loaded onto MWCNTs, the experimental values were 49.67 wt.% and 51.78 wt.% for the CVD and sol-gel methods respectively. Two replicates were measured starting from digestion and the averaged values are recorded in **Table 4.6**.

Table 4.6: Titania wt.% loadings for MWCNT-titania nanocomposites synthesised by the sol-gel and CVD methods

targeted titania wt.%	Experimental wt.% (standards deviation, n=2)	
	sol-gel	CVD
98.00	98.15 (0.28)	98.60 (0.64)
95.00	94.21 (0.15)	94.28 (1.08)
90.00	89.50 (0.04)	92.84 (0.77)
85.00	85.95 (1.20)	86.94 (0.27)
60.00	59.03 (0.37)	60.64 (0.35)
50.00	51.78 (1.42)	49.67 (0.23)
40.00	40.28 (1.01)	37.51 (1.35)
20.00	19.85 (1.44)	21.32 (0.36)
10.00	12.17 (1.06)	9.63 (0.57)
5.00	5.68 (0.71)	6.51 (0.13)

Overall, both methods produce composites with a composition close to the desired loadings.

4.8 Conclusion

Physicochemical properties MWCNT-titania nanocomposites were investigated thoroughly by a number of techniques such as Raman, TGA, FTIR and X-ray. Acid treatment appears to lower the thermal stability of pristine MWCNTs. The structural integrity of the MWCNTs was retained after acid treatment. Synthesis of titania below 400 °C yield only anatase phase of titania. Anatase titania was successfully coated onto MWCNTs to form porous nanomaterials and there exist a covalent link between titania and MWCNTs in the nanocomposites. This bond improves intimacy between MWCNT and titania.

The morphology and dimensions were greatly influenced by the wt.% ratios of MWCNTs to titania. The general trend was increase in diameter ranges with an increase in titania ratio and the lower the MWCNTs ratio the more they were completely coated. In nanocomposites by the sol-gel synthetic method, low wt.% of titania gave isolated particulates whilst higher wt.% gave larger coatings along walls. In the nanocomposites by the CVD synthetic method, nanocomposites became honeycomb-like with an increase in titania wt.%. Both methods coated small diameter MWCNTs well. CVD synthetic method gave better precision of titania loadings with the targeted load than sol-gel.

The techniques correlated well and it was observed that the physicochemical properties of the nanocomposites can be influenced by the synthetic method and ratios of components. CVD method is a better method than sol-gel because it had more attributes as discussed in previous sections in this chapter. For example, nanocomposites by the CVD method were more crystalline than those by sol-gel, had MWCNTs with less defects and more thermally stable. MWCNTs improved surface area and pore volume of titania in both synthetic methods. The increased pore size in nanomaterials by the CVD synthetic method is amongst other positive attributes for dye adsorption in DSSC applications. The larger the pores the larger the number of dye molecules adsorbed and this can ultimately enhance photon reception. In conclusion, physicochemical properties were successfully investigated.

References

1. A. Rinaldi, B. Frank, D. S. Su, S. B. A. Hamid, R. Schloglv, *Chemical Materials,* 2011, **23**, 926-928.

2. Q. Q. Fana, Z. Y. Qinab, X. Lianga, L. Lia, W. H. Wub, M. F. Zhu, *Experimental Nanoscience*, 2010, **5**, 337-347.

3. K. A. Wepasnick, B. A. Smith, K. E. Schrote, H. K. Wilson, S. R. Diegelmann, D. H. Fairbrother, *Carbon*, 2011, **49**, 24-36.

4. V. Datsyuk, M. Kalyva, K. Papagelis, J. Parthenios, D. Tasis, A. Siokou, I. Kallitsis, C. Galiotis, *Carbon*, 2008, **46**, 833-840.

5. F. Aviles, J. V. Cauich-Rodrıguez, L. Moo-Tah, A. May-Pat, R. Vargas-Coronado, *Carbon,* 2009, **47**, 2970-2975.

6. H. Yu, X. Quan, S. Chen, H. Zhao, *The Journal of Physical Chemistry C*, 2007, **111**, 12987-12991.

7. T. Sawatsuk, A. Chindaduang, C. Sae-Kung, S. Pratontep, G. Tumcharern, *Diamond and Related Materials,* 2009, **18**, 524-527.

8. S. Muduli, W. Lee, V. Dhas, S. Mujawar, M. Dubey, K. Vijayamohanan, S. H. Han, S. Ogale, *Applied Materials and Interfaces*, 2009, **1**, 2030-2035.

9. T. Y. Lee, P. S. Alegaonkar, J. B. Yoo, *Thin Solid Films*, 2007, **515**, 5131-5135.

10. S. Kim, S. R. Jang, R. Vittal, J. Lee, K. J. Kim, *Applied Electrochemistry,* 2006, **36**, 1433-1439.

11. G. Khan, Y. K. Kim, S. K. Choi, D. S. Han, A. Abdel-Wahab, H. Park, *Bulletin of the Korean Chemical Society,* 2013, **34**, 1137-1145.

12. N. Aman, P. K. Satapathy, T. Mishra, M. Mahato, N. N. Das, *Materials Research Bulletin,* 2012, **47**, 179-183.

13. W. R. Jung, J. H. Choi, N. Lee, K. Shin, J. H. Moon, Y. S. Seo, *Carbon*, 2012, **50**, 633-636.

14. Y. Li, L. Li, C. Li, W. Chen, M. Zeng, *Applied Catalysis A: General,* 2012, **427-428**, 1-7.

15. B. Gao, G. Z. Chen, P. G. Li, *Applied Catalysis B: Environmental*, 2009, **89**, 503-509.

16. D. Zhao, X. Yang, C. Chen, X. Wang, *Colloid and Interface Science,* 2013, **398**, 234-239.

17. J. E. Swain, M. V. Juskelis, J. P. Slanga, J. G. Miller, M. Uberoi, N. D. Spencer, *Applied Catalysis A: General*, 1996, **139**, 175-187.

18. J. P. Salvetat-Delmotte, A. Rubio, *Carbon,* 2002, **40**, 1729-1734.

19. V. N. Popov, *Materials Science and Engineering: R: Reports*, 2004, **43**, 61-102.

20. Y. M. Wong, S. Wei, W. P. Kang, J. L. Davidson, W. Hofmeister, J. H. Huang, Y. Cui, *Diamond and Related Materials*, 2004, **13**, 2105-2112.

21. M. R. Golobostanfard, H. Abdizadeh, *Microporous and Mesoporous Materials,* 2014, **183**, 74-80.

22. J. Marugán, M. J. López-Muñoz, J. Aguado, R. van Grieken, *Catalysis Today*, 2007, **124**, 103-109.

23. P. Delhaes, M. Couzi, M. Trinquecoste, J. Dentzer, H. Hamidou, C. Vix-Guterl, *Carbon,* 2006, **44**, 3005-3013.

24. P. Vincent, A. Brioude, C. Journet, S. Rabaste, S. T. Purcell, J. Le Brusq, J. C. Plenet, *Non-Crystalline Solids,* 2002, **311**, 130-137.

25. D. Y. Kim, J. J. Park, J. G.Lee, M. F. A. M. van Hest, S. S. Yoon, *Ceramics International* 2013, **39**, 9737-9742.

26. Z. Li, B. Gao, G. Z. Chen, R. Mokaya, S. Sotiropoulos, G. Li Puma, *Applied Catalysis B: Environmental,* 2011, **110**, 50-57.

27. A. Jitianu, T. Cacciaguerra, R. Benoit, S. Delpeux, F. Béguin, S. Bonnamy, *Carbon,* 2004, **42**, 1147-1151.

28. M. Radoičić, Z. Šaponjić, J. Nedeljković, G. Ćirić-Marjanović, J. Stejskal, *Synthetic Metals,* 2010, **160**, 1325-1334.

29. S. A. Kosa, G. Al-Zhrani, M. A. Salam, *Chemical Engineering,* 2012, **181**-**182**, 159-168.

30. D. M. Chipara, J. Macossay, A. V. R. Ybarra, A. C. Chipara, T. M. Eubanks, M. Chipara, *Applied Surface Science*, 2103, **275**, 23-27.

31. G. Fang, W. Gao, Q. Deng, K. Qian, H. Han, S. Wang, *Analytical Biochemistry,* 2012**,** **423**, 210-217.

32. J. J. Niu, J. N. Wang, Y. Jiang, L. F. Su, J. Ma, *Microporous and Mesoporous Materials*, 2007, **100**, 1-5.

33. J. H. Lehman, M. Terrones, E. Mansfield, K. E. Hurst, V. Meunier, *Carbon,* 2011, **49**, 2581-2602.

34. http://antoine.frostburg.edu/chem/senese/101/inorganic/faq/discovery-of-carbon.shtml, accessed on 13 October, 2013.

35. S. Osswald, M. Havel, Y. Gogotsi, *Raman Spectroscopy,* 2007, **38**, 728-736.

36. T. Belin, F. Epron, *Materials Science and Engineering: B,* 2005, **119**, 105-118.

37. Y. Cong, X. Li, Y. Qin, Z. Dong, G. Yuan, Z. Cui, X. Lai, *Applied Catalysis B: Environmental,* 2011, **107**, 128-134.

38. G. Jiang, Z. Lin, L. Zhu, Y. Ding, H. Tang, *Carbon,* 2010, **48**, 3369-3375.

39. Y. Sun, A. Li, M. Qi, L. Zhang, *Materials Science and Engineering*, 2001, **B86**, 185-188.

Chapter Five

Light-harvesting experiments

The main focus of this chapter is application of nanocomposites in light-harvesting (synthesised and characterised as explained in **Chapter Three**). Photoluminescence (PL) and diffuse reflectance results and discussion are also presented in this chapter. Also note that parameters such as wind velocity, humidity (since Durban is very humid) and cell operating temperature which may affect cell performance in light-harvesting[1,2] were not monitored in this study but the effects were minimised in an enclosed room condition. The ideal condition would have been the use of a glove box. However, the devices will perform better in a more controlled environment for better analysis and the focus of the study was to investigate trends due to varying MWCNTs for devices measured under the same conditions.

5.1 Introduction

Harnessing energy efficiently and cheaply is the focus of this work. In doing so, one cannot avoid the term photovoltaic (PV) cell. Photovoltaic (defined and explained in the literature review, **Chapter Two**) is a latin term born in the nineteenth century into the English language. In the current literature, the term is used interchangeably with solar devices. The terms can generally be used to refer to energy from the sun although they are sometimes employed in a wider scope such as photo detectors. The PV technology has been realised as a green energy approach to counteract increasing world energy demands.[3] This technology largely consists of silicon-based solar cells (first generation); semiconductor thin films (second generation); organic solar cells and DSSCs (third generation).[4] Nowadays, attention is shifting largely towards DSSCs from silicon-based solar cells, especially in the last two decades, due to reasons discussed in the literature review such as low fabrication costs.[6]

This chapter focuses on DSSCs discovered by Grätzel in 1991.[4,5] A typical DSSC is a photo-electrochemical system made up of a mesoporous n-type semi-conducting photoanode nanomaterial film coated on top of a conducting metal oxide on a transparent glass substrate. This is coupled with a thin film photocathode material coated on a glass substrate and redox couple electrolyte solution between the two photoelectrodes to make energy generation a continuous process.[4,7,8] A good electrolyte enables reduction of excited dye molecules thereby eliminating the possibility of recombination with their neighbours.[9] The background of photo-electrochemical systems originated in the 1950s with common applications being group four and five elements due to their narrow band gaps.[4] However, these narrow band gap semiconductors unlike titania are corroded by electrolytes. The efficiency of a DSSC is influenced by electron injection, optical absoption, internal resistance, light scattering, surface area and rate of electron transport.[8,10] Various morphologies of titania such as nanorods[11] and rice-grain[12] have found much attention in the field of DSSCs. Nanoparticles have some interesting capabilities based on dimensional alterations. Nanoparticles enhances surface area of the photoanode thereby enhancing absorption *via* light scattering.[4,5]

5.2 Properties of an ideal dye for solar cell sensitisation

The key role of dye molecules in DSSCs is to capture photons from the sun. To achieve this, a dye must have certain favourable characteristics such as:

- Broad absorption spectrum.
- High extinction coefficient.
- Ability to form chemisorption bonds with oxide.
- Suitable excited state energy level relative to conduction band of the oxide.
- Good lifetime.
- Long term stability.
- Higher enough redox potential for it to be regenerated by the electrolyte.[13]

The chemical reactions involved in the electrolyte systems where S is a dye molecule are represented in **equations 5.1**-**5.4**.

1. Photoanode

Photon capture: $TiO_2 + S \rightarrow TiO_2/S^*$ (**equation 5.1**)

Electron injection: $TiO_2/S^* \rightarrow TiO_2/S^+ + e^-$ (**equation 5.2**)

2. Photocathode

Regeneration: $S^+ + 3I \rightarrow I_3^- + S$ (**equation 5.3**)

Redox reaction: $I_3^- + 3e^- \rightarrow 3I^-$ (**equation 5.4**)

This work briefly focuses on application of titania nanoparticles coated onto the MWCNT walls by the CVD and sol-gel synthetic methods in DSSCs. MWCNT-titania nanocomposites were the semi-conducting photoanode material, ITO glass was the transparent substrate that allows light to pass through, the redox couple was gel state electrolyte and a thin film of aluminium on an ordinary glass substrate was the photocathode.

5.3 Results and discussion

This section outlines diffuse reflectance, photoluminescence results and the light-harvesting results of the devices fabricated by the use of nanocomposites.

5.3.1 Diffuse reflectance

Although diffuse reflectance is a standard technique for measuring and providing some insight into the band gap of photoactive materials.[15] It is preferred to simple UV-Vis because it can distinguish between dispersed light and absorbed light unlike the UV-Vis which also introduces spectra complexity from solvents.[44] The technique uses the fact that semiconductors produce charge carriers at wavelengths below band gap wavelength.[15] Absorption or band gap edge is the transition between strong short wavelength and weak long wavelength absorption in spectrum of solid.[45] Diffuse reflectance depends on thickness, refractive index and surface roughness of the sample.[15] Spectra position of band gap edge is determined by energy separation between valence band and conduction

band.[45,44] Variations in band gap were particularly expected in this work since these parameters changed due to different ratios and different synthetic methods used. Different positions of the absorption edges with various materials, i.e. the point on the spectrum at which reflectance decreases sharply implies different band gap energies.

Nanomaterials were prepared for measurements by pilling about 3 mm nanocomposites on a black surface. $BaSO_4$ was used as a standard because it is a brilliant white compound with total reflectance.[15] The $BaSO_4$ was initially spread on a black surface to allow for background correction. It must be noted that all the nanocomposites, including a commercial titania sample, were measured under the same conditions and that the focus of the study was to deduce the trend observed with the change in wt.% of MWCNTs in the nanocomposites.

The following equation was used to compute the band gap energy from the cut off wavelength (λ);

$$\text{Energy (eV)} = \frac{hc}{\lambda} = \frac{1.24\times10^{-6}}{\lambda\,(m)} \qquad \textbf{(equation 5.5)}$$

Where *h* is Plank's constant and *c* is the speed of light.

The formula given by **equation 5.5** assumes that the experiment was done in a vacuum but the experiments were done at room temperature. The variations associated were insignificant because the work was more concerned on band gap trends at various wt.% ratios of MWCNTs:titania. The 2-20 wt.% of MWCNTs (see **Table 5.1**) represent samples with small MWCNT ratios. Samples synthesized using the sol-gel method showed an increase in band gap with an increase in wt.% of the MWCNTs in the range 2 to 20 wt.%. For the CVD synthetic method, the band gap decreased from 2 to 10 wt.% of MWCNTs then increased between 10 and 20 wt.%. The lowest band gap was observed at 50 wt.% of MWCNTs by both methods. Decreasing the band gap of titania *via* doping has been reported in the literature[16-18] (see **literature review**) but this creates e^-/h^+ recombination

centres.[11] Furthermore, at 50 wt.% MWCNTs the band gap of the titania-MWCNTs is comparable to N-doping of titania (ca. 2.9 eV) reported by Aman *et al*.[19] Therefore, from the results of this work and other similar reports using MWCNTs to reduce band gap might be preferable to doping because MWCNTs inhibit e^-/h^+ recombination as observed from photoluminescence results (see **section 5.4.2**). This is because MWCNTs readily conducts the e^- from the titania CB. In nanocomposites with high wt.% of MWCNTs (e.g. at 95 wt.% of MWCNTs), the band gap was greater than that of anatase, 3.2 eV (see **Table 5.1**) implying higher e^-/h^+ recombination than anatase. The band gap shifted towards that of MWCNTs which is reported to be 4.5 eV.[12] This observation concurred with the key findings of Murphy in that the thinnest coating will have the largest band gap.[15] This means that nanocomposites of higher MWCNTs ratios were not ideal for light-harvesting and this agreed with the observations of this work. According to the results in **Table 5.1** it is noted that the band gap of the nanocomposites is lower than the band gap of MWCNTs. In some cases for nanocomposites produced by the sol-gel and/or CVD synthetic methods (i.e. 95 and/or 90 wt.% of MWCNTs) the band gaps are higher than that of titania.

Table 5.1: The band gap determination using diffuse reflectance spectroscopy

Wt.% MWCNTs	Band gap energy (eV)	
	Sol-gel method	CVD method
2	3.062	3.179
10	3.100	3.024
20	3.139	3.062
50	2.918	2.988
90	3.163	3.333
95	3.351	3.605
titania	3.2	
MWCNTs	4.5	

5.3.2 Photoluminescence

PL is a form of luminescence i.e. light emission-based technique and is triggered when a substance is photo-excited from a ground state usually at shorter wavelength than the emitted light. Since energy is inversely proportional to wavelength, the emitted light is of

lower energy implying longer wavelength. The technique focuses on electronic and vibrational states. In this work, PL is used to investigate e^-/h^+ recombination dynamics since MWCNTs in MWCNT-titania nanocomposites offered large surface-area-to volume ratio (see **Chapter Four**, **section 4.6**). The titania surface area was enhanced by incorporation of MWCNTs in nanocomposites (see **Table 4.5**). High surface area plays a role in interfacial e^- transfer in the MWCNTs/titania interface of nanocomposite as well as in nanocomposite/electrolyte interface.[40] Also, intra-band-gap, which is related to local defects, can act as traps for free carriers and this influences recombination and e^- transport. Hence, it was necessary to investigate e^-/h^+ recombination dynamics.

Defects that act as e^- traps are located on the nano-crystalline particle surface. Defects on the titania surface are associated with oxygen vacancies and sintering can remove these defects.[30] Therefore, since MWCNT-titania nanocomposites were analysed as samples rather than as sintered photoanode materials on the DSSC device, the actual defects and e^-/h^+ recombination in the devices are less than that projected in the nanocomposites analysis. However, since the analysis was done under the same conditions, the trends based on different nanocomposite ratios were elucidated. In **section 4.4.1** (see **Figure 4.16**), MWCNT-titania nanocomposites with more defects (by the sol-gel method) had higher e^-/h^+ recombination as expected (see **Figure 5.1 A** and **B**).[30]

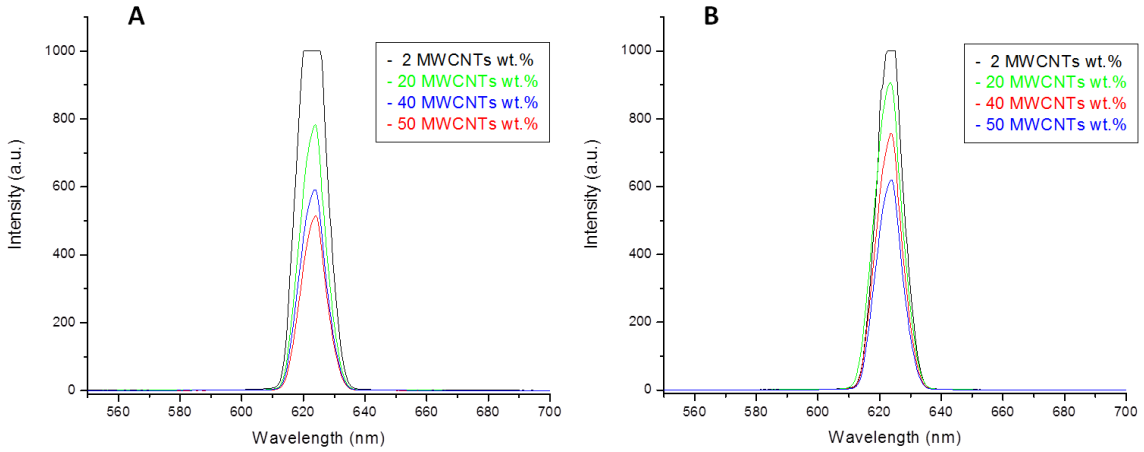

Figure 5.1: A comparison of PL spectra for 2, 20, 40 and 50 wt.% of MWCNTs in MWCNT-titania nanocomposites by the (**A**) CVD and (**B**) sol-gel synthetic methods

This is due to a drastic reduction of e^-/h^+ recombination in the MWCNT-titania nanocomposites.[24,30] This means e^-/h^+ recombination was less in nanocomposites by the CVD than sol-gel synthetic method. According to **Figure 5.1A** and **B**, coating titania onto MWCNTs and increasing MWCNTs ratios in nanocomposites reduced strong recombination in titania. This observation concurred with the report by Bing-shun *et al.*[24] TiO_2 exhibit PL emission spectra at ca. 650 nm due to radiative recombination of self-trapped excitons due to oxygen vacancies at an uncoordinated surface defect, i.e. green light emission and that at ca. 420 nm is due to shallow trap emission which is a bulk phenomenon.[20-23] It is observed from the PL spectra (see **Figure 5.1A** and **B**) that the peak intensity at ca. 625 nm decreased with an increase in wt.% of MWCNTs. This observation agreed with the views by Zhao *et al*.[25] This is attributed to a decrease in e^-/h^+ recombination and the observed peak position suggest that recombination in the nanocomposite was due to radiative recombination of self-trapped excitons. There are two possible traps in this work. The h^+ traps due to oxygen vacancies as stated above. The h^+ traps are more likely to be present since titania in MWCNT-titania nanocomposites had 101 as the main surface orientation (see **section 4.4.2** and additional information in **Appendix B**).[22] Removal of bridging oxygen atoms leaves two electrons which reduces neighbouring Ti^{4+} to Ti^{3+}. The Ti^{3+} species and e^-s at oxygen vacant centres trap holes.[31] Oxygen vacancies are favourable as carrier transport but reported elsewhere to be detrimental in DSSCs performances.[31]

Candy *et al.*[31] suggested that surface shallow traps facilitate carrier diffusion whereas deep traps seem to conflict with the intrinsic n-type semiconductor titania. According to the spectra obtained it is seen that MWCNTs achieved the goal of readily accepting the excited electron from titania thereby quenching the PL. The absence of NIR emission peak at ca. 835 nm correlated with absence of rutile in the nanocomposites.[32] The lack of peaks at 143 cm^{-1}, 235 cm^{-1}, 447 cm^{-1} and 612 cm^{-1} in the Raman spectra [21] and XRD peaks at the value of $2\theta = 27.3^o$, 35.9^o, 41.2^o and 54.4^o (see **section 4.4.1** and **4.4.2**) also implies absence of rutile phase titania.[26,27]

5.3.3 Gel state electrolyte

An electrolyte is also an important part of a DSSC device because recombination of photo-injected electrons with the oxidised form of the electrolyte redox couple can be detrimental.[28] The most suitable way of enhancing DSSCs efficiency is the addition of appropriate chemical species in the electrolyte in order to tune electrolyte/semiconductor interface.[29] 1-Methyl-3-propylimidazolium iodide is a charge transfer intermediate [30] and its involvement in the synthesized gel state electrolyte as an ionic liquid requires higher iodine concentration. This is because high viscosity of ionic liquids retards I^-_3 diffusion. Hence, reduces charge-transport efficiency under irradiation.

Conductivity of iodine was seen to increase with its concentration (see **Table 5.2**) but the higher the concentration of iodine, the darker the solution. Dark iodine solutions are strong light absorbers at ca. 430 nm.[28,31] Stergiopoulus *et al.*[29] reported that short circuit current density (J_{sc}) decrease systematically with increase in iodine concentration and this implies that there exist a specific critical iodine concentration for an optimum DSSC functioning. Higher iodine concentration cause unwanted recombination of photo-injected electrons with I^-_3.[28] Hence, at higher concentration of iodine, the performance of the device can greatly deteriorate. For these reasons 0.5 M was selected to avoid competition for light absorption with the photoanode material and detrimental effects in the DSSCs devices. Iodine (0.5 M) was also used in the synthesis of liquid electrolyte in this work.

Table 5.2: The optimisation of iodine concentration for gel state electrolyte synthesis used in DSSCs

Iodine concentration /M	Conductivity / μ S cm^{-1}	Temperature /°C
0.1	1.0	18.5
0.2	8.1	18.9
0.5	16.3	19.0
0.8	33.3	19.3
1.0	36.4	19.2

According to the results in **Table 5.3**, addition of lithium iodide, 1-methyl-3-propylimidazolium iodide, 4-Tert-butylpyridine and guanidium thiocyanate improved conductivity of iodine. This concurred with findings reported earlier, for example, addition of 4-Tert-butylpyridine improve open circuit voltage (V_{OC}) whilst guanidium thiocyanate addition was found to increase both V_{OC} and J_{SC}.[29] 4-Tert-butylpyridine deprotonate the titania surface and hence shift conduction band (CB) towards negative potentials and passivates the surface active recombination centres. On the contrary, guanidium thiocyanate accumulates positive charge on titania surface thereby causing a positive shift of the CB and hence increase e^- injection efficiency.[29] This slows down e^-/h^+ recombination. From this view, synergistic effects of these additives in a single identical system affect direct recombination reaction with iodine.

PVAc act as gelator in the electroltye.[30] Conductivity of the liquid electrolyte was observed to decrease with mass of PVAc from 0-0.4 g (see **Table 5.3**). On addition of about 0.6 g PVAc an abrupt increase in conductivity was observed. However, on addition of about 0.8 g PVAc, the conductivity was observed to decreased due to poor solubility of the polymer. Hence, the mass used in gel state electrolyte synthesis was 0.6 g. The effect of high solvent volatility which limits long run applicability was elliminated by the use of PVAc (see **section 5.3.5.2**). These results are similar to literature reports.[9] This means a working electrolyte with reasonable conductivity was synthesised for light-harvesting.

Table 5.3: The optimisation of PVAc mass in gel state electrolyte synthesis used in DSSCs

PVAc mass /g	Conductivity /μ S/cm	Temperature /°C
0.0000	30.4	18.0
0.1963	20.7	19.1
0.3914	13.8	19.2
0.5670	84.0	19.7
0.7828	61.6	19.2

5.3.4 Absorption spectra of dye

Eosin B has two absorption peaks (see **Figure 5.2**) at 400 nm and 525 nm. The latter is the absorption maxima. Therefore, according to the spectra, eosin B absorbs in the visible region making it a suitable sensitizer in DSSCs.[32] The spectra show that at lower concentrations the absorption peak at 400 nm is very weak and the absorption maxima are sharper. Therefore, to increase the absorption region, a higher concentration (600 mg L^{-1}) was used in this work.

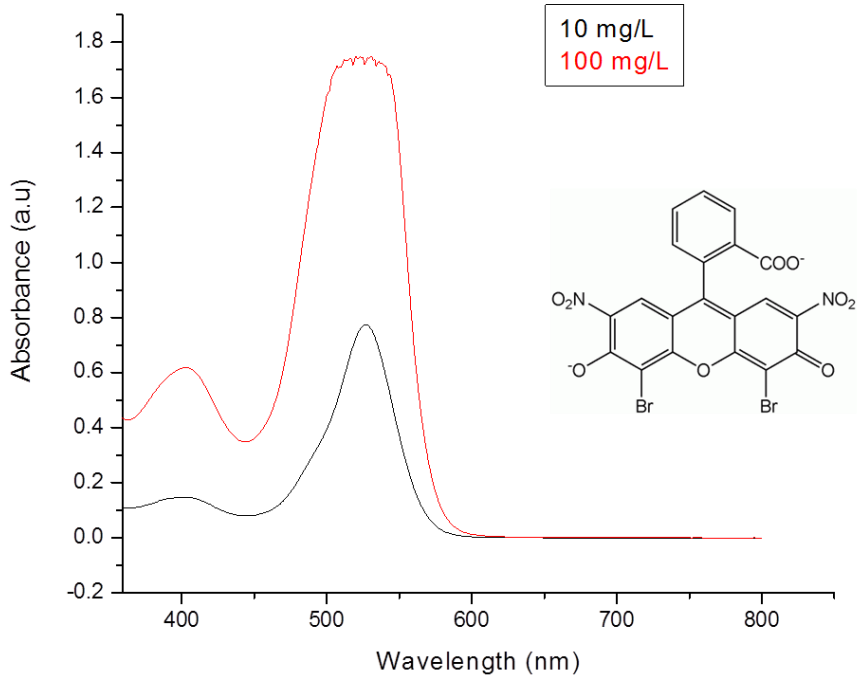

Figure 5.2: The absorbance spectra for eosin B used in DSSCs

5.3.5 Set up of DSSCs

In this section the effects of MWCNTs as photo-electrochemical materials in light-harvesting experiments were presented. Eosin B dye was able to facilitate removal of h^+ from photon e^-/h^+ pairs from the TiO_2 phase. This event was also aided by MWCNTs strong conductivity of electrons due to their lower Fermi level relative to titania[33] since an e^- has a shorter diffusion length.[11] The general film thickness unless stated otherwise was 70 µm and the concentration of eosin B dye was 600 mg L^{-1}.

5.3.5.1 Polyethylene glycol binder effect on DSSC performance

The effect of polyethylene glycol (PEG) as a binder in DSSCs was investigated using sol-gel synthesised titania. The values obtained were 0.35 m A cm^{-2}, 0.41 V, 17.11 and 0.02 for J_{SC}, V_{OC}, fill factor (FF as explained in **Chapter One**) and efficiency (n) respectively. The values were compared to sol-gel synthesised titania with no binder i.e. J_{SC} of 2.26 m A cm^{-2}, V_{OC} of 0.83 V, FF of 27.76 and n of 0.50. PEG reduced the device performance drastically in a similar manner as reported elsewhere.[32] Hence, the study was done with no binder even though binders are reported to reduce cracks in nanocomposites thereby improving contact.[34] A decrease in performance could have been due to the thickness of the photoanode material involved in this work which was above 1 µm introducing adverse effect to the electron movement.[34] Therefore, since the anode film thickness involved in this work was 70 and 160 µm, it was ideal not to use the PEG binder.

5.3.5.2 Liquid iodine electrolyte application in DSSCs

Initially, the electrolyte used was liquid iodine. **Table 5.4** results show poor DSSCs performance obtained from the use of iodine liquid as an electrolyte. The J_{SC} values obtained indicates that there was e^- movement in the DSSCs devices fabricated but the potential to transfer these electrons was very low. The poor results were due to the drying effect of the electrolyte since acetonitrile is highly volatile. A gel state electrolyte was synthesised to overcome this effect (see **section 3.6.1** in **Chapter Three** and light-harvesting results in **section 5.3.5.3**).

Table 5.4: The Light-harvesting performance for the titania synthesised by the sol-gel method at 70 µm using iodine liquid electrolyte

J_{SC} /m A cm^{-2}	V_{OC} /V	FF	n
0.187	0.584	22.594	N/A
0.130	0.002	N/A	N/A
0.139	0.003	N/A	N/A
0.533	0.043	N/A	N/A
0.465	0.027	N/A	N/A

∗ N/A means devices gave negligible values

The redox electrolyte was drying out before transferring the e^-s from the photoanode *via* the external circuit to the eosin B dye molecules. This means the circuit was broken and there was no regeneration of the ground state eosin B dye. Hence, no substantial efficiency values were obtained (see **Table 5.4**). However, it may be noted that some high efficient DSSCs have been reported using similar organic solvents.[28] The design of the DSSC devices matters in this regard i.e. devices involving drilled and sealed holes containing the liquid electrolyte will not have drying effects unlike the system used in this work.

5.3.5.3 Application of nanocomposites in DSSCs

In this section results presented and discussed are for light-harvesting experiments carried out without using PEG binder and using a gel state electrolyte.

For sol-gel synthetic method, FF generally increased with an increase in MWCNTs wt.%. The highest FF was at 15 wt.% of MWCNTs (see **Table 5.5**). However, the highest efficiency and open circuit voltage was at 10 wt.% of MWCNTs (see **Table 5.5)**. In the nanocomposite from the sol-gel method only V_{OC} (ca. 0.63 V) was comparative with the values regarded as standard in the report by Lee *et al*.[35] It must be noted that the devices in this work were fabricated differently. In this work MWCNTs were part of the photoanode material whilst in their work, the MWCNTs were part of the electrolyte system and counter electrode. From the V_{OC} values, it can be seen that nanocomposites from the CVD method have potential to do more work than those from sol-gel except at 10 MWCNTs wt.%. Generally, V_{OC} values presented in **Table 5.5** predicts high efficient devices. However, the low device efficiencies in the DSSCs fabricated could have been due to the charge carriers' recombination or loss during the various transfer and redox processes along the DSSC functional chain i.e. eosin B dye to MWCNT-titania, aluminium counter electrode to iodide and iodide back to eosin B dye.

In this work, above 15 wt.% of MWCNTs the performance of the fabricated DSSC devices deteriorated (see 40 and 50 MWCNTs wt.% in **Table 5.5**). The most likely possibility is the interference of MWCNTs in electron transport, i.e. high MWCNTs e^- conductivity disrupts e^- transfer to the counter electrode in MWCNT-titania nanocomposites with high MWCNTs

wt.%. Also high MWCNTs wt.% means reduced titania wt.% ratio in the nanocomposites which is required for the initial electron-hole pair separation.

Table 5.5: Light-harvesting performance for the nanocomposites synthesised by the sol-gel and CVD methods at 70 µm using gel state electrolyte

Wt.% MWCNTs	J_{SC} (m A cm^{-2})		V_{OC} (V)		FF		n	
	Sol-gel	CVD	Sol-gel	CVD	Sol-gel	CVD	Sol-gel	CVD
2	1.54	29.51	0.54	0.64	11.71	1.82	0.10	0.34
5	1.76	76.11	0.66	0.71	11.66	1.40	0.14	0.76
10	0.03	0.56	0.83	0.65	16.91	63.76	0.17	1.07
15	0.20	13.00	0.58	0.68	43.20	19.25	0.13	1.71
40	1.22	18.77	0.23	0.62	16.91	2.86	0.05	0.33
50	0.01	1.42	0.68	0.95	33.99	7.02	0.03	0.09

According to the results obtained from nanocomposites by the sol-gel synthetic method, performance was poorer compared to titania with no MWCNTs loaded (see **Table 5.5)**. The best sol-gel nanocomposite was 66% reduced in efficiency from that of titania.

The **Table 5.6** displays the performance of the best performing wt.% of MWCNTs from both methods at 130 µm thickness (thicker than 70 µm used for data in **Table 5.5**).

Table 5.6: The MWCNT-titania nanocomposites synthesised by the CVD and sol-gel methods at 130 µm

wt.% MWCNTs (method)	J_{SC} (m A cm^{-2})	V_{OC} (v)	FF	n
0	2.26	0.83	26.76	0.50
10 (Sol-gel)	3.87	0.53	33.12	0.68
10 (CVD)	11.95	0.69	3.36	0.28
15 (Sol-gel)	4.09	0.76	9.34	0.29
15 (CVD)	0.21	0.47	25.17	0.02

There was not much change observed in terms of V_{OC} in the nanocomposites by the CVD synthetic method. However, 50 wt.% of MWCNTs had the highest V_{OC} yet the efficiency was very low. The increase in V_{OC} means a decrease in e^-/h^+ recombination.[32] This agreed with the observed lowest band gap and lowest PL peak intensity at 50 wt.%. This means poor performances can be due to current loss (or electrons) *via* parasitic processes such as slow redox processes with the iodide system, slow redox between the dye and the iodide couple.[28] Furthermore, MWCNTs might be interfering with electron movement i.e. their high e^- conductivity causing more electrons to be trapped in the MWCNTs interface without being transferred to the counter electrode. Since MWCNTs wt.% has an effect on band gap energy (see **section 5.3.1**), the change in band gap at 50 wt.% might have been misaligned with energy levels of the eosin B dye. This compromised the injection of excited electrons into the LUMO of titania above 20 wt.% of MWCNTs.

The best FF was observed at 10 wt.% of MWCNTs and best performance was observed at 15 wt.% of MWCNTs with a 242% enhancement of efficiency from that of titania with no MWCNTs. Short circuit current density was seen to decrease with wt.% of MWCNTs (see **Figure 5.3**).

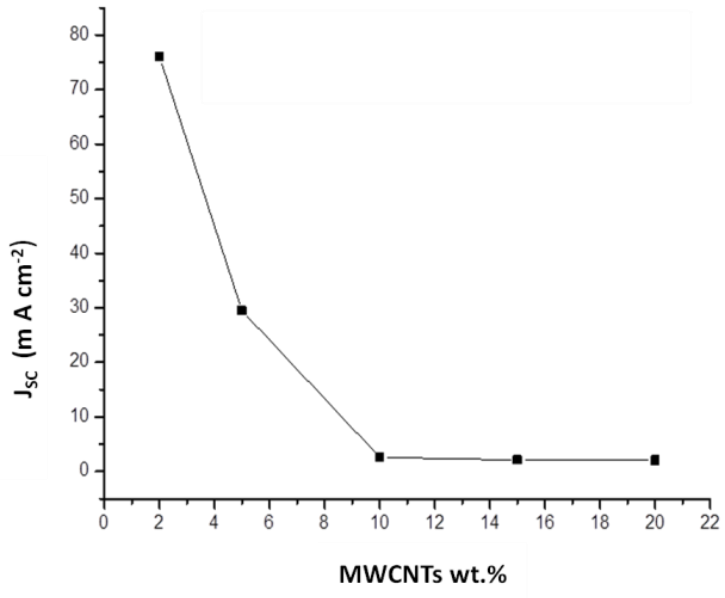

Figure 5.3: The short circuit current density for nanocomposites synthesised by CVD method

The lower band gap (see **Table 5.1**) and decrease in defects (see **Chapter Four**, **section 4.4.1**, **Figure 4.16**) for MWCNT-titania nanocomposites from CVD method is an indication of inter-particle connectivity differences. Lower band gap energy enhances e^- transport in the titania nano-crystalline and reduced defects decreases recombination.[30] According to data presented in **Table 5.5** the range 5 to 15 wt.% of MWCNTs, nanocomposites from the CVD synthetic method had better efficiencies than titania.

Even though nanocomposites with 50 wt.% MWCNTs had the lowest band gap from both methods, it may be noted that at such high MWCNTs loadings the strong background MWCNTs absorption between 400 nm and 800 nm arises.[36] Also, a decrease in optical transparency and shifting of band gap towards that of MWCNTs above 50 wt.% of MWCNTs may have been the main reasons why such nanocomposites did not work in light-harvesting experiments.[12] The low J_{SC} at 50 wt.% of MWCNTs implies poor electron transport yet high MWCNTs wt.% provides excellent electron pathway. The most likely possibility is failure of e^- re-injection into the iodide redox couple.[37]

High V_{OC} values shows that there was no recombination of photo-generated electrons with the electrolyte.[38] It can also imply decrease in charge recombination as discussed above.[28] Furthermore, V_{OC} is weakly influenced by counter electrode,[7,11] hence, high V_{OC} may suggest that aluminium is a good counter electrode material. This is a positive attribute because aluminium is cheaper than platinum which is commonly used in PV.[39] Despite the fact that high electric potential values (V_{OC}) were observed from both methods, efficiencies were generally lower than expected (see **Table 5.5**). This could have been due to parasitic resistive losses such as slow interface e^- transfer and slow redox processes with the iodide system leading to recombination as mentioned earlier.[40] The high electric potential can be attributed to addition of guanidium thiocynate as discussed above.[13]

In general, nanocomposites by the CVD synthetic method performed better than those produced by sol-gel in terms of J_{SC} and n. Furthermore, the V_{OC} from CVD nanocomposites was generally higher than those by sol-gel method except at 10 wt.% of MWCNTs. This observation is seen to correlate with the higher defects in sol-gel nanocomposites which increase recombination with oxidised species of iodine in the contacting gel state electrolyte decreasing photovoltage and photocurrent. Therefore, since V_{OC} is inversely proportional to

FF, FF from nanocomposites by the sol-gel method was higher than those from CVD method.

Synthetic method affect the physicochemical properties such as uniformity of oxide coat on MWCNTs walls and surface area [41] which ultimately affects device performance. The thickness of the titania oxide layer on MWCNTs alters the diffusion path length in the titania interface before being conducted by the MWCNTs. This could play a big role in performance, when electrons are transported by the MWCNTs the electrons can be taken to the wrong way, i.e. back recombination with the dye, this may account for low FF generally presented in **Table 5.5**. The synthetic method will have an effect on surface morphology, surface defects, nanostructure, electronic properties and ultimately on efficiency of DSSCs. This plays a role in electron transport *via* creation or reduction of recombination centres. For example, nanocomposites by the CVD method were highly crystalline and the particle sizes were larger than sol-gel method. This could have reduced the number of boundaries for potential e^-/h^+ recombination even though it reduced the surface area of the nanocomposites compared to those by the sol-gel method.[32]

Shi *et al.*[32] reported that more crystalline structures have low PL intensity. This agrees with the observations in this work since low PL intensity suggests low e^-/h^+ recombination. The enhanced surface area from both methods relative to that of titania, in turn enhanced electrochemical properties such as improved electron transport of titania.[12,35] The possibility of Schottky barrier creation between titania/MWCNTs interface lowers chances of recombination in the titania interface.[37] Furthermore, the observed covalent link between anatase titania and MWCNTs *via* oxygen-containing groups (see **Table 4.1** and **Figure 4.15**, **Chapter Four** in **section 4.3**) improved intimacy between titania and MWCNTs which may be absent in the physical mixture reported by some authors.[25,42] This C-O-Ti bond extends light absorption to longer wavelength.[25]

It was interesting to observe that increasing the thickness of the photoanode layer improved the performance of the sol-gel nanocomposite at 10 wt.% of MWCNTs, it performed better than both pure titania and CVD nanocomposites. A 36% improvement and a 62% decrease in efficiency were observed for sol-gel and CVD methods respectively.

The improvement of efficiency of sol-gel method nanocomposite with thickness of photoanode in the device agreed with the observation by Fan *et al.*[43]

5.4 Conclusion

The band gap of titania decreased with increase in wt.% of MWCNTs up to 50 wt.% i.e. lower MWCNTs wt.% reduced titania band gap and above 50 wt.% it shifted towards the band gap of MWCNTs in both methods. Radiative recombination of self trapped excitons was more dominant in MWCNT-titania nanocomposites synthesised from both methods. The e^-/h^+ recombination in titania decreased with an increase in MWCNTs. The sol-gel nanocomposites have higher e^-/h^+ recombination than those by the CVD synthetic method. MWCNTs are good electron acceptors at the MWCNT/titania interface in MWCNT-titania nanocomposites.

The gel state electrolyte synthesised was less volatile than liquid iodine on its own. Eosin B absorbed in the UV region of light and therefore was a suitable sensitizer in this work. The DSSC devices fabricated had positive rectification (see additional information in **Figures F1** and **F2** in **Appendix F**). Aluminium coated on ordinary glass can be used as a counter electrode in DSSCs. Nanocomposites by the CVD synthetic method were better photoanode nanomaterials than those by sol-gel. Use of PEG as a binder was detrimental to the performance of DSSC devices fabricated in this work. Crystal structure of nanocomposites influences light-harvesting capabilities, i.e. the more crystalline the nanocomposites the better were the light-harvesting abilities. Surface defects and larger band gap reduced DSSCs performances.

References

1. D. Mukherjee, S. Chakrabarti, *New age International publishers: India*, 2007, pp 86.
2. M. Fitra, I. Daut, M. Irwanto, N. Gomesh, Y. M. Irwan, *Energy Procedia*, 2013, **36**, 333-340.
3. H. C. Weerasinghe, F. Huang, Y. B. Cheng, *Nano Energy*, 2013, **2**, 174-189.
4. Q. Zhang, G. Cao, *Nano Today*, 2011, **6**, 91-109.
5. W. J. Lin, C. T. Hsu, Y. C. Tsai, *Colloid and Interface Science*, 2011, **358**, 562-566.
6. P. Du, L. Song, J. Xiong, N. Li, L. Wang, Z. Xi, N. Wang, L. Gao, H. Zhu, *Electrochimica Acta*, 2013, **87**, 651-656.
7. S. S. Mali, C. A. Betty, P. N. Bhosale, P. S. Patil, *Electrochimica Acta*, 2012, **59**, 113-120.
8. J. Spivack, O. Siclovan, S. Gasaway, E. Williams, A. Yakimov, J. Gui, *Solar Energy Materials and Solar Cells*, 2006, **90**, 1296-1307.
9. W. Tang, M. H. Santare, S. G. Advani, *Carbon,* 2003, **41**, 2779-2785.
10. A. M. Bakhshayesh, M. Mohammadi, H. Dadar, D. J. Fray, *Electrochimica Acta*, 2013, **90**, 302-308.
11. M. Wright, A. Uddin, *Solar Energy Materials and Solar Cells*, 2012, **107**, 87-111.
12. Z. Peining, A. S. Nair, Y. Shengyuan, P. Shengjie, N. K. Elumalai, S. Ramakrishna, *Photochemistry and Photobiology A: Chemistry*, 2012, **231**, 9-18.
13. M. Grätzel, *Photochemistry and Photobiology C: Photochemistry Reviews*, 2003, **4**, 145-153.
14. K. I. Ding, J. Melas-Kyriazi, N. L. Cevey-Ha, K. G. Chittibabu, S. M. Zakeeruddin, M. Grätzel, M. D. McGehee, *Organic Electronics*, 2010, **11**, 1217-1222.
15. A. B. Murphy, *Solar Energy Materials and Solar Cells*, 2007, **91**, 1326–1337.
16. L. T. Anh, A. K. Rai, T. V. Thi, J. Gim, S. Kim, E. C. Shin, J. S. Lee, J. Kim, *Power Sources,* 2013, **243**, 891-898.

17. Q. Liu, Y. Zhou, Y. Duan, M. Wang, X. Zhao, Y. Lin, *Alloys and Compounds,* 2013, **548**, 161-165.

18. M. L. Kääriäinen, D. C. Cameron, *Thin Solid Films*, 2012, **526**, 212-217.

19. N. Aman, P. K. Satapathy, T. Mishra, M. Mahato, N. N. Das, *Materials Research Bulletin*, 2012, **47**, 179-183.

20. A. Stevanovic, M. Büttner, Z. Zhang, J. T. Yates, *American Chemical Society,* 2012, **134**, 324-332.

21. J. Shi, J. C. Z. Feng, T. Chen, Y. Lian, X. Wang, C. Li, *Physical Chemistry,* 2007, **111**, 693-699.

22. C. C. Mercado, F. J. Knorr, J. L. McHale, S. M. Usmani, A. S. Ichimura, L. V. Saraf, *Physical Chemistry*, 2012, **116**, 10796−10804.

23. F. Knorr, D. Zhang, J. L. McHale, *Langmuir*, 2007, **23**, 8686-8690.

24. H. Bing-shun, C. Feng-yim, M. Y. Wey , *International Journal of Hydrogen Energy*, 2010, **12**, 2503-2510.

25. D. Zhao, X. Yang, C. Chen, X. Wang, *Colloid and Interface Science*, 2013, **398**, 234-239.

26. J. Orlikowski, B. Tryba, J. Ziebro, A. W. Morawski, J. Przepiórski, *Catalysis Communications,* 2012, **24**, 5-10.

27. M. Krivec, R. A. Segundo, J. L. Faria, A. M. T. Silva, G. Dražić, *Applied Catalysis B: Environmental,* 2013, **140-141**, 9-15.

28. Z. Yu, M. Gorlov, J. Nissfolk, G. Boschloo, L. Kloo, *Physical Chemistry C*, 2010, **114**, 10612-10620.

29. T. Stergiopoulos, E. Rozi, C. S. Karagianni, P. Falaras, *Nanoscale Research Letters*, 2011, **6**, 307.

30. Y. Rong, X. Li, G. Liu, H. Wang, Z. Ku, M. Xu, L. Liu, M. Hu, Y. Yang, M. Zhang, T. Liu, H. Han, *Power Sources*, 2013, **235**, 243-250.

31. Q. J. Yu , Y. H. Zhang , Y. Yi , N. N. Zu , J. Zhang, P. Wang, *American Chemical Society nano*, 2010, **4**, 6032-6038.

32. H. A. Hsiao, C. C. Leu, C. H. Yang, T. L. Wang, Y. T. Shieh, *Electrochimica Acta*, 2013, **111**, 784-790.

33. Y. Cong, X. Li, Y. Qin, Z. Dong, G. Yuan, Z. Cui, X. Lai, *Applied Catalysis B: Environmental*, 2011, **107**, 128-134.

34. W. Wu, G. Zhao, G. Han, B. Song, *Materials Letters*, 2007, **61**, 1922-1925.

35. S. U. Lee, W. S. Choi, B. Hong, *Solar Energy Materials and Solar Cells*, 2010, **94**, 680-685.

36. E. Piperopoulos, S. Santangelo, M. Lanza, G. Faggio, G. Messina, S. Galvagno, A. Pistone, C. Milone, *Diamond and Related Materials*, 2011, **20**, 532-537.

37. G. Khan, Y. K. Kim, S. K. Choi, D. S. Han, A. Abdel-Wahab, H. Park, *Bulletin Korean Chemical Society*, 2013, **34**, 1137-1145.

38. S. R. Jang, M. J. Choi, R. Vittal, K. J. Kim, *Solar Energy Materials and Solar Cells*, 2007, **91**, 1209-1214.

39. S. Yang, H. Kou, S. Song, H. Wang, W. Fu, *Colloids and Surfaces A: Physicochemical and Engineering Aspects*, 2009, **340**, 182-186.

40. M. A. Green, *Solar cell fill factors: General graph and empirical expression solid state electronics*, 1981, **24**, 788-789.

41. Y. Li, L. Li, C. Li, W. Chen, M. Zeng, *Applied Catalysis A: General*, 2012, **427-428**, 1-7.

42. A. de Morais, L. M. D. Loiola, J. E. Benedetti, A. S. Gonçalves, C. A. O. Avellaneda, J. H. Clerici, M. A. Cotta, A. F. Nogueira, *Photochemistry and Photobiology A: Chemistry*, 2013, **251**, 78-84.

43. K. Fan, M. Liu, T. Peng, L. Ma, K. Dai, *Renewable Energy*, 2010, **35**, 555-561.

44. A. E. Morales, E. S. Mora, U. Pal, *Revista Mexicana De Fisica*, 2007, **53**, 18-22.

45. S. Ebraheem, A. El-Saied, *Material Science and Applications*, 2013, **4**, 324-329.

Chapter Six

Thesis conclusions and future work

In this chapter, summaries of each previous chapter, overall conclusions from the study and future work suggestions based on the findings from this work are presented.

6.1 Summary

Chapter One links the significance of studying physicochemical properties of MWCNT-titania nanocomposites for DSSC applications with the reported work in literature. This was done by means of a brief background of the importance of energy in the global village and problems associated with growing demand. This culminates in the need to look for alternatives to current energy sources. The aim and objectives of the study, and motivation behind the study are stated. This chapter justified certain choices that were made in this study such as nanomaterials used in the work, research approach, i.e. CVD and sol-gel methods and properties to be investigated. The systematic approach to the study, based on the stated hypotheses and research questions, is also presented and justified. This chapter generally gave the direction taken based on the reviewed materials in Chapter Two when the work was started. Finally, this chapter stated the overview of the thesis. Therefore, in brief, this chapter gives an insight of the ideas from literature involved in solving a real world problem, i.e. energy crisis and directs the reader to the various chapters mushrooming from the review.

Chapter Two describes the realization of the importance of energy by the earliest man on the planet and also reviews the energy resources in modern societies. Current energy demands against resources are further explained; thereafter the chapter discusses the possible alternative energy resources to fossil fuels. Disadvantage of each possible renewable energy and attributes of solar energy as a good green energy resource are also stated. The world energy production levels are reviewed in this chapter. Also, various

policies are discussed within this chapter pointing out how both developing and developed countries aims to face a potential energy crisis through various roadmaps.

Chapter Two further explains how nanotechnology has the potential to solve the real world's problem, "energy crisis" *via* generation of nanomaterials with higher efficiencies and band gap engineering of current nanomaterials on the market. Nanoscience and nanotechnology which are terms often confused were defined and differentiated. Carbon was recognized as the key player and thus carbon allotropes, including CNTs and their chemistry are described within this chapter. Properties and applications of MWCNTs are also presented in greater detail within this chapter. MWCNTs require modifications in order to manipulate them as functional moieties and therefore possible modifications of MWCNTs were identified. Chapter Two further narrowed down to MWCNTs in MWCNT-titania nanocomposites.

Background information on titania in terms of properties, forms, band gap modifications and exciton generation mechanism was also explained in this chapter. The survey showed that MWCNTs had a potential to tune physicochemical properties of tinania nanoparticles towards higher light-harvesting capabilities. MWCNT-titania nanocomposites synthesis methods were identified. In addition, analytical techniques used for characterization of nanomaterials are discussed in terms of how they are crucial to the study presented in the subsequent chapters. The theory behind DSSC as a photo-electrochemistry system was explained within the chapter. The background on some important parameters involved in PV systems are also stated and explained. Chapter Two also gives some reported work done in the field of DSSCs which is relevant to our approach in order to have a rough idea of what was on the ground when the work was started.

Chapter Three is an experimental section. Chapter Three presents the details of; reagents, solvents, materials and experimental procedures involved in the acid treatment of MWCNTs, synthesis of nanocomposites as well as in fabrication of DSSCs. The details of; reagents, solvents and procedures involved in electrolyte synthesis were also given within this chapter. This chapter also outlines details of the two synthetic methods used in this study, i.e. sol-gel and CVD. Details of the experimental procedures such as use of an ultrasonic water bath, stirrer, solvents and how the precursors were mixed by the sol-gel

method are also given in greater detail. The information of the parts used in constructing the CVD reactor, temperature program involved and how precursors were mixed together were also presented within this chapter. Range of MWCNTs ratio to titania in the MWCNT-titania nanocomposites was from 2 to 98 wt.%. Instrumental and software details for the physicochemical characterisation, i.e. SEM, TEM, HR-TEM, TGA, Raman spectroscopy, powder XRD, FTIR spectroscopy and textural characteristics, and light-harvesting characterization techniques, i.e. diffuse reflectance, PL, UV-Vis and solar simulator, engaged in this work are given within the chapter. The diagram showing components and the design of DSSC devices used in this work, and a brief view of how measurements were carried out in this work is given. In short, this chapter gives all experimental steps involved, i.e. from acid treatment of MWCNTs *via* MWCNT-titania nanocomposite synthesis, physicochemical characterization to application of nanocomposites in DSSCs.

Chapter Four is the core of the study. It discusses each method and the results obtained in this work. Morphology and dimensional studies were done by SEM, TEM and HRTEM. The three dimensional images from SEM shows that uniformity of titania coating on MWCNTs varied with differences in wt.% of MWCNTs. The TEM gave good two dimensional images showing that titania coated MWCNTs. EDS was used as a qualitative technique in identifying the elements present as titanium and carbon. This technique also gave a rough view of how the two elements identified were distributed within the nanocomposites. ICP-OES quantified the amount of titanium in each nanocomposites culminating in the calculation of the wt.% ratios of MWCNTs to titania. The FTIR spectroscopy was the method used to investigate the relationship of titania and MWCNTs in the nanocomposites and other chemical bonds present. This technique also identified the phase present in the nanocomposites as anatase. Thermal stability of MWCNTs in the synthesized nanocomposites was investigated by TGA and according to the results from this technique, high titania wt.% reduced MWCNTs resistance to oxidation and it also showed that experimental wt.% ratios of MWCNTs:titania correlated with those obtained by means of ICP-OES. The graphitic quality trend of MWCNTs in the nanocomposites was investigated using Raman spectroscopy which also agreed with FTIR spectroscopy on anatase being the only phase present. This was further confirmed by powder XRD which also gave the surface crystal arrangements in addition to its ability to reveal the high degree of crystalinity in the

nanocomposites. According to the textural characteristics obtained, the MWCNTs improved surface area by reducing titania agglomeration, pore volume of titania and showed that the nanocomposites were mesoporous. In short, Chapter Four presents and compares a thorough characterization approach to MWCNT-titania nanocomposites synthesized from the sol-gel and CVD methods.

Chapter Five gave a presentation of some electrical characterizations of the MWCNT-titania nanocomposites, i.e. band gap and e^-/h^+ recombination dynamics using diffuse reflectance and photoluminescence respectively. A brief explanation of the DSSCs and the properties of an ideal dye were also presented. UV-Vis was used to investigate absorption maxima of the eosin B dye. From this technique it was observed that eosin B was potentially suitable for DSSCs applications because it absorbed in the visible region. The light-harvesting experiments results and discussion are presented in greater detail within this chapter. The main aim of this chapter is to apply the MWCNT-titania nanocomposites in light-harvesting. The nanocomposites synthetic method influences physicochemical properties such as defects, surface area and interfacial contact on the MWCNT/titania interface and hence affects e^- transport. The nanocomposites prepared by the CVD method performed better in DSSCs than those made by sol-gel techniques and band gap engineering is not the only factor than can enhance light harvesting capabilities.

A summary of the work or conclusions are given in *Chapter Six*. A possible description of possible future is also given.

6.2 Overall conclusion

According to the experimental data obtained from the current work, various conclusions can be made. The acid treatment reduced agglomeration of MWCNTs during the sol-gel synthesis. Nitric acid opened MWCNTs and created defects on the tube walls for both sol-gel and CVD methods thereby reducing MWCNTs thermal stability. The oxygen containing functional groups aided titania coating onto MWCNTs by improving chemical interactions in the sol-gel method. The procedures in both sol-gel and CVD methods were able to coat titania onto MWCNTs. In this study, it was also seen that MWCNTs to titania ratios and

synthetic method influenced physicochemical properties such as nanostructure, ultimate morphology and surface area. According to EDX mapping, CVD approach gave a better distribution of titania dispersion on MWCNTs than sol-gel method. From Raman spectroscopy results, CVD nanocomposites were less defective i.e. had smaller $\frac{I_D}{I_G}$ ratio. Titania sat on the defects thereby reducing defect intensity on the MWCNT walls.

Thermal stability of the MWCNTs improved in MWCNT-titania nanocomposites from both sol-gel and CVD method relative to that of acid-treated MWCNTs. In addition to this, coating MWCNTs caused tube bending which created weak points for thermal oxidation at elevated temperatures. TGA and ICP-OES suggested that CVD approach was a better titania loading method since the actual loaded titania wt.% had better precision with the theoretically expected values than sol-gel. According to the FTIR spectrum obtained, titania was covalently linked to MWCNTs *via* the oxygen-containing groups on the tube walls. The FTIR and other techniques such as Raman spectroscopy, photoluminescence and powder XRD suggested that the only phase present in the MWCNT-titania nanocomposites from both CVD and sol-gel methods was anatase. According to XRD diffractogram, CVD nanocomposites were more crystalline. Also, from the textural characterization done, the sol-gel method gave large surface area of nanocomposites than those from CVD method. CVD was found to be a better synthetic method than sol-gel. The vacuum effect involved in the CVD method is critical for better quality of MWCNT-titania nanocomposites than sol-gel. The MWCNT-titania nanocomposites produced by the CVD method have more uniform coating, higher thermal stability, and larger pore volume and size, less defects and were more crystalline compared to those made by sol-gel process.

Some interesting conclusions were made from observed electronic properties and light-harvesting experiments. To begin with, MWCNTs reduced e^-/h^+ recombination and band gap when loaded to titania. The e^-/h^+ recombination was more in sol-gel MWCNT-titania nanocomposites than CVD. Band gap shifted towards that of MWCNTs above 50 wt.% of MWCNTs ratio whereas below 50 wt.%, MWCNTs reduced band gap of titania. The conclusion from the redox system synthesized was that the gel state electrolyte was more stable and less volatile than iodine electrolyte alone. Hence, the gel state electrolyte was more ideal for the DSSC design used than liquid iodine. The gel state electrolyte unlike

iodine was able to regenerate dye molecules in the DSSC design used in this work. Eosin B absorbed in the UV-Vis region and hence, is a suitable metal-free sensitizer for DSSC light-harvesting.

From the physicochemical characteristics and light-harvesting experiments the conclusions deduced are elucidated below. The nanostructures synthesized were working photo-anode materials with a positive rectification and therefore MWCNT-titania nanocomposites can be applied in DSSCs. The devices have high potential to do work. Also, low wt.% ratios of MWCNTs to titania in MWCNT-titania nanocomposites from both sol-gel and CVD methods performed better in DSSCs than high ratios. From the experiments carried out, the optimum MWCNTs wt.% in DSSCs applications from CVD method was 15 and 10 wt.% for sol-gel method. CVD method nanocomposites performed better in DSSCs than sol-gel nanocomposites. This is because of number reasons such that CVD nanocomposites had larger pore size and pore volume which is available for dye to fill in. Also, CVD nanocomposites were more crystalline and therefore had less number of nanoparticle boundaries. Crystalinity improve electrical conductivity. Therefore, CVD nanocomposites had minimal chances of e^-/h^+ recombination at nanoparticle boundaries. An intimate contact between TiO_2 and MWCNTs caused relative positions of MWCNTs CB edge to allow e^- transfer from TiO_2 to MWCNTs at the titania/MWCNTs interface. In addition to that, the CO-Ti link improved intimacy of titania and MWCNTs more in CVD. The deductions are made from the more intense CO-Ti peak from FTIR spectroscopy observed in CVD approach than sol-gel method. This also improved light-harvesting capabilities in DSSC devices fabricated using nanocomposites by the CVD method.

In short, titanium optical properties were tailored to enhance its light harvesting capabilities and the ideal properties for better light-harvesting performance deduced from this work include crystalinity, large pore size and volume, uniform morphology, existence of chemical bonds between components of nanocomposites and a defect-free nature. V_{OC} is influenced by CB of MWCNT-titania nanocomposite. Band gap engineering is not the only factor vital for enhancement of light harvesting capabilities. Absorption properties of DSSC components rather than nanocomposites also affect device performances. The high e^- conductivity nature of MWCNTs interferes with e^- transfer from the MWCNT/titania

interface to the counter electrode in nanocomposites with high MWCNTs wt.% thereby causing DSSCs deterioration.

6.3 Future work

Many possible avenues for future research exist and of particular interest include the following. Firstly, an investigation of the effects of incorporating silver and gold nanoparticles into MWCNT-titania nanocomposites-based hybrid solar cells has the potential to enhance efficiencies because the two metals are reported in literature to enhance light harnessing. Secondly, an investigation of the effect of various nanocomposite deposition techniques onto ITO coated glass such as spin coating can improve understanding of the ideal morphology on the device. The morphology of the photoanode nanomaterials plays a key role in e^- transport since surface defects can act as e^- or h^+ traps influencing the e^-/h^+ recombination dynamics. In addition, determination of the diffusion path length of the exciton and optimization of the film thickness of a DSSC active layer such that it is shorter is equally vital in enhancing efficiencies of a DSSC device. Also, although high MWCNTs wt.% provide an excellent e^- pathway it affect reinjection into the redox couple, it will be interesting to investigate the performances of a DSSC device using thin films. A comparison of nanocomposites synthesized by sol-gel and CVD methods with a physical mixture of laboratory synthesized titania and acid-treated MWCNTs in DSSC applications can bring a better understanding of the effects of the covalent link between titania and MWCNTs. In addition, comparison of physicochemical properties of nanocomposites from different precursors but by the same synthetic method can contribute immensely in understanding the effects. Even though iron levels were reduced to almost zero use of iron free MWCNTs will be a good control experiment of this work.

Other possible areas of investigation include the effect of dye soaking time of a DSSC device on the performance and the use of two dyes that compliment each other in light-harvesting as well as the effect of dye concentrations in DSSCs. The use of common natural dyes such as flower dyes as sensitizers in DSSCs leaves a lot to be desired against the metal-based laboratory synthesized dyes. The redox system in a DSSC device is equally crucial to the electrode nanomaterials and therefore an investigation of the effects of pH on the

performance of an electrolyte is worth a focus. A more challenging approach will be to characterize the PV cells electrochemically. This involve designing a way of quantifying absorption efficiency, exciton dissociation efficiency, charge transfer efficiency and charge carrier collection efficiency at interfaces separately since they constitute the overall efficiency of a DSSC device. Whilst there exist some speculations that ITO coat on glass disintegrate above 200 °C FTO does not, the DSSCs devices of this work were sintered above that temperature. Therefore, a comparison of FTO and ITO in DSSCs using MWCNT-titania nanocomposites can be a good avenue to explore. Finally, the use of a glove box eliminates the possibility of environmental effects during light-harvesting experiments.

Appendix A
Isotherms

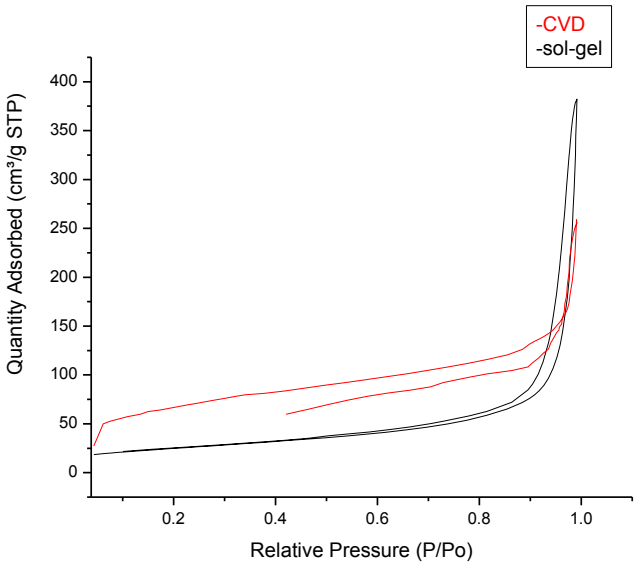

Figure A1: The representative isotherms for sol-gel and CVD nanocomposites

Appendix B
Powder XRD spectra

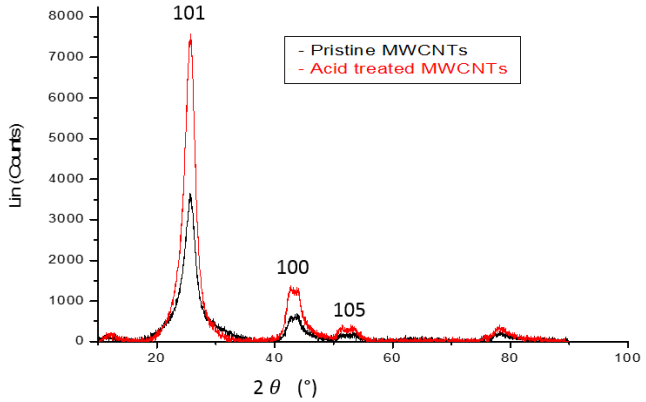

Figure B1: XRD spectra for pristine and acid-treated MWCNTs

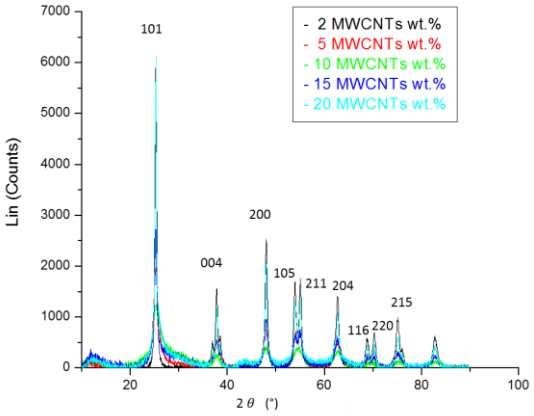

Figure B2: XRD spectra for nanocomposites with high titania wt.% ratios synthesised by sol-gel method

Appendix C
TGA derivative curves

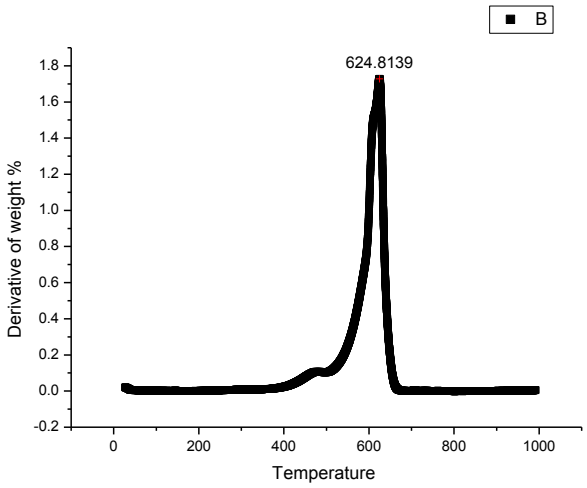

Figure C1: The temperature derivative curve in air for acid-treated MWCNTs

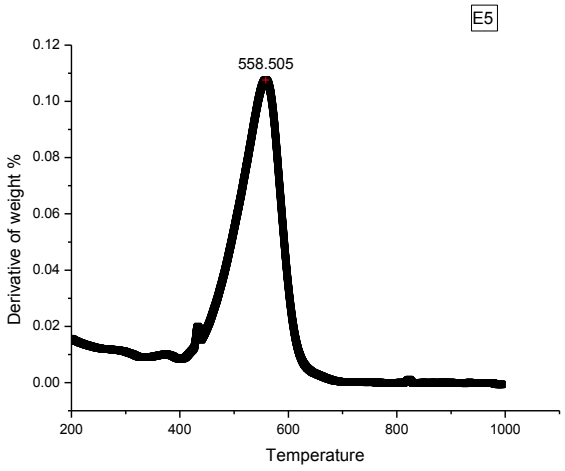

Figure C2: The representative temperature derivative curve in air for sol-gel nanocomposites at 10 wt.% of MWCNTs

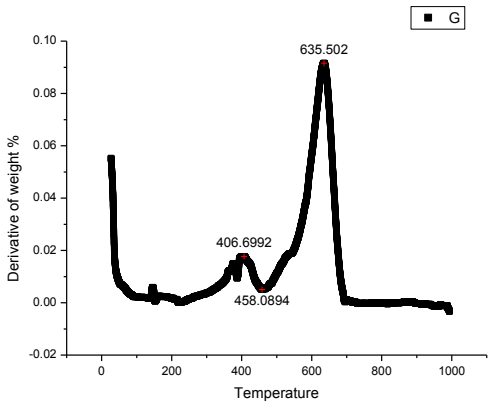

Figure C3: The representative temperature derivative curve in air for CVD nanocomposites at 10 wt.% MWCNTs

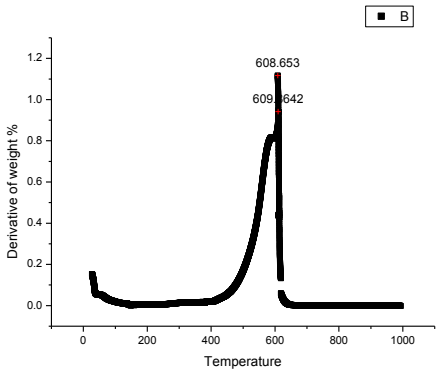

Figure C4: The representative temperature derivative curve in air for sol-gel nanocomposites at 90 wt.% MWCNTs

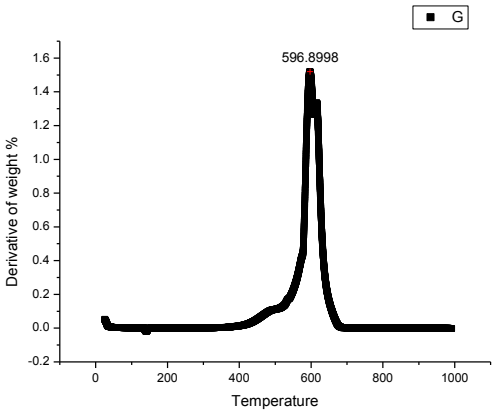

Figure C5: The representative temperature derivative curve in air for CVD nanocomposites 90 wt.% MWCNTs

Appendix D
Raman results

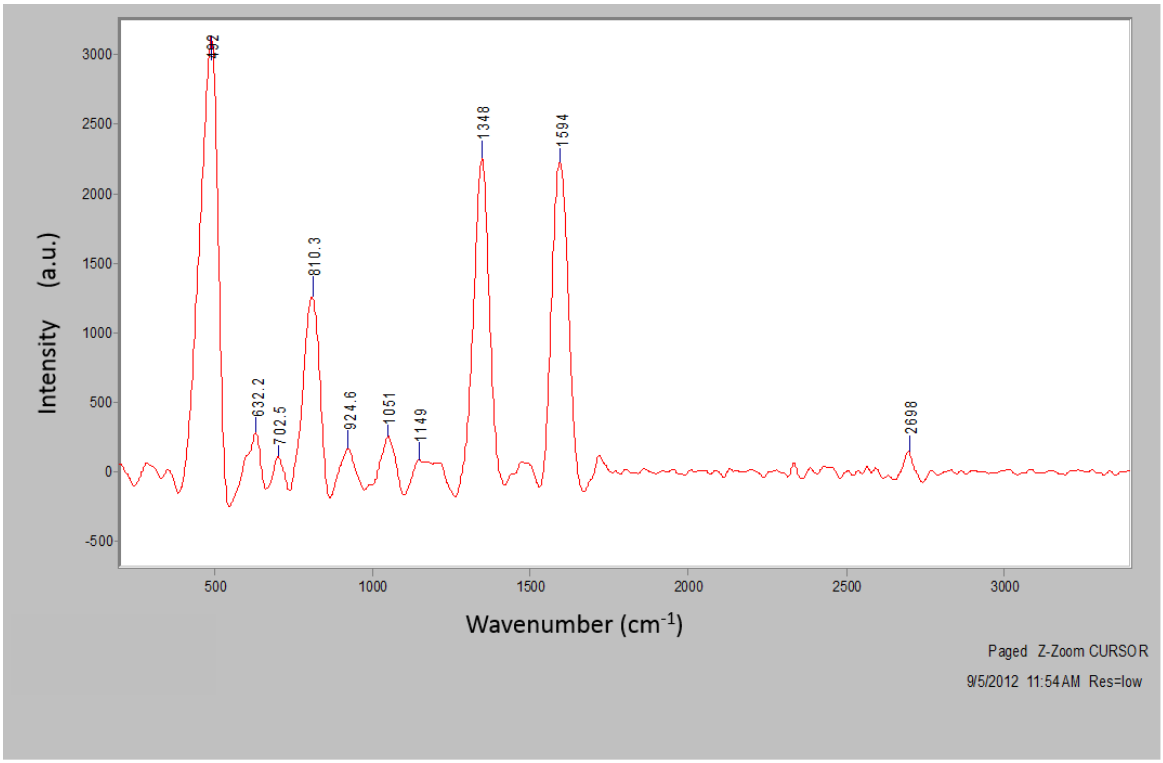

Figure D1: The representative Raman spectrum for pristine MWCNTs

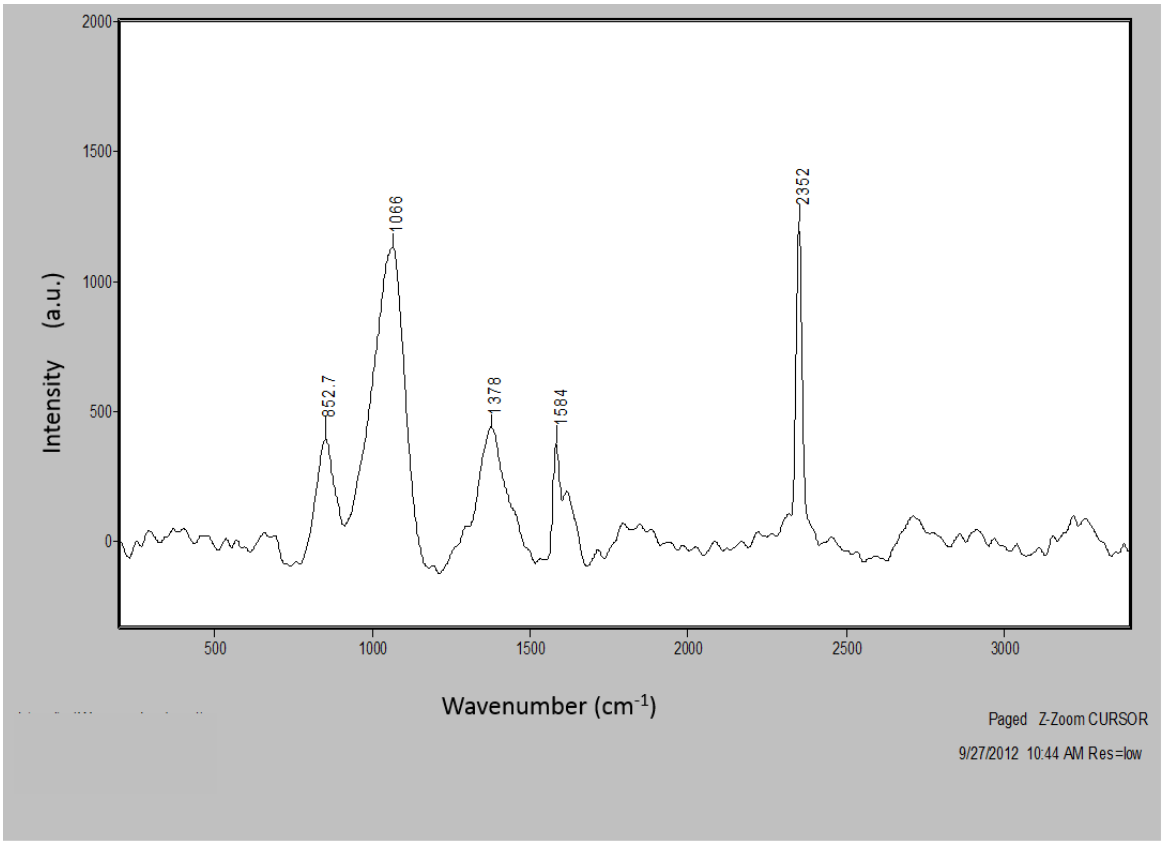

Figure D2: The representative Raman spectrum for the acid-treated MWCNTs

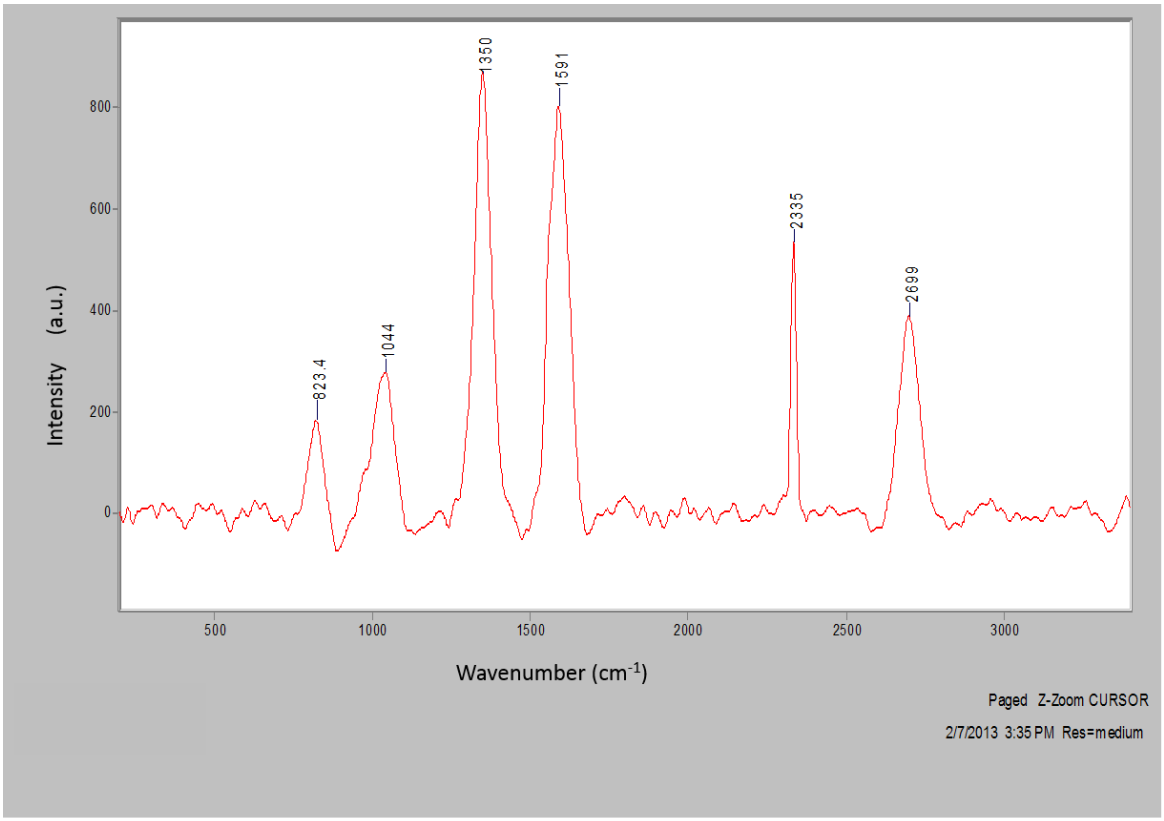

Figure D3: The representative Raman spectrum for the 10 wt.% of titania synthesised by sol-gel method

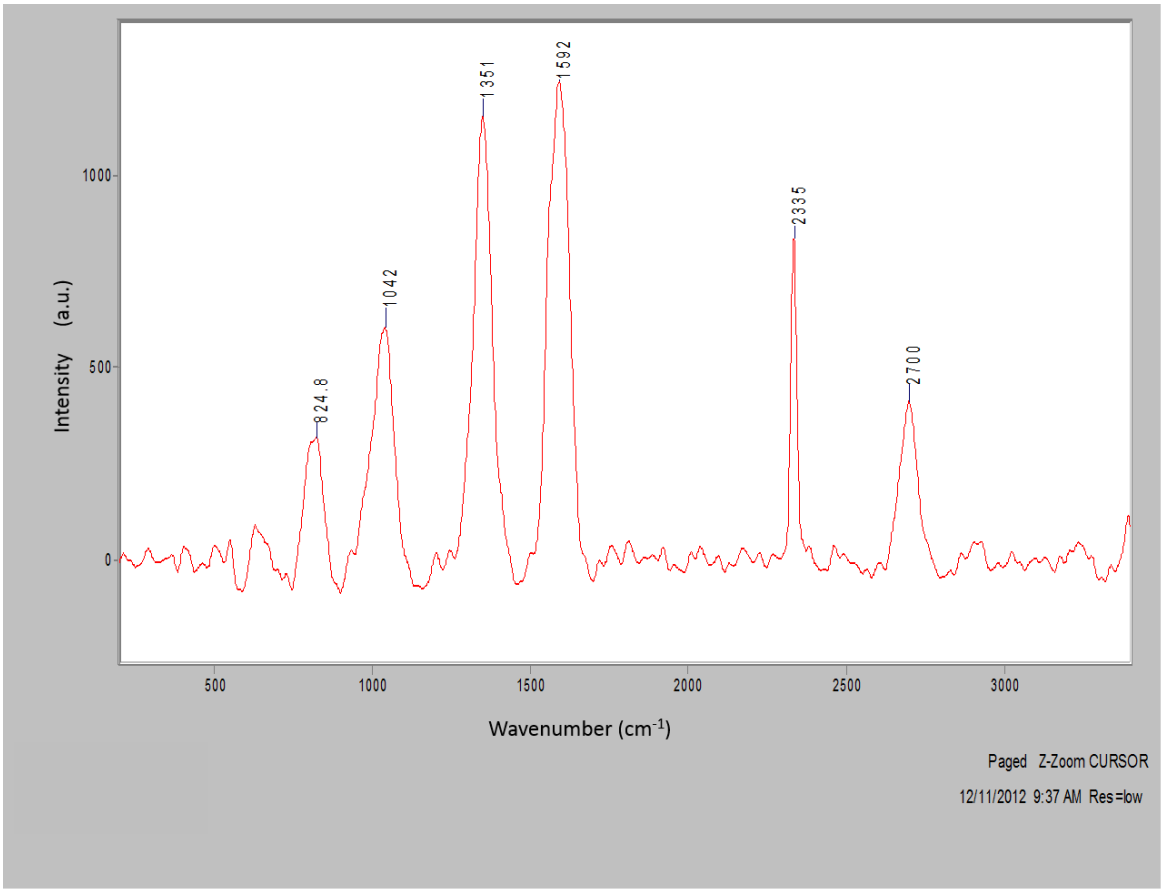

Figure D4: The representative Raman spectrum for the 15 wt.% of titania synthesised by CVD method

Table D1: The G and D band for nanocomposite synthesized by sol-gel at varying high MWCNTs wt.%

wt.%	D band		G band		$\frac{I_D}{I_G}$
	Position	Width	Position	Width	
4	1371.9	25.768	1581.5	16.224	0.0950
7	1347.2	56.154	1588.1	105.39	0.4860
8	1376	10.366	1581.9	12.142	0.1716
15	1351	61.662	1591.3	118.38	0.3794
2	1352	67.432	1590.3	123.05	0.4906
5	1351.3	62.642	1590.3	106.17	0.5513
10	1351	60.338	1592	127.84	0.3154
15	1350.2	70.504	1591.8	210.12	0.1243
20	1350.5	55.224	1588.4	133.71	0.2736
40	1351.1	55.319	1558.0	7.176	1.7532

Table D2: The D and G band for nanocomposites synthesized by sol-gel at varying low MWCNTs wt.%

wt.%	D band		G band		$\frac{I_D}{I_G}$
	Position	Width	Position	Width	
2	1350.3	54.763	1557	5.7904	0.0179
10	1349.1	69.432	1586.9	145.97	0.3854
15	1350	61.952	1588.4	184.10	0.1652
5	1372.2	15.385	1802.5	183.03	0.0281
10	1350.7	67.372	1586.9	150.02	0.2762
20	1355.3	182.91	1585.4	118.77	2.1945
2	1353.2	69.673	1583.6	129.44	0.3238
10	1354.3	73.322	1583.6	129.44	0.1176
0.5	1356.1	72.001	1587.4	149.62	0.2322
40	1350.2	64.369	1588.3	122.24	0.4165
50	1352.2	66.911	1588.6	171.06	0.1937

Table D3: The D and G band for CVD synthesized nanocomposites with varying high MWCNTs wt.%

wt.%	D band		G band		$\frac{I_D}{I_G}$
	Position	Width	Position	Width	
5	1351.2	61.911	1590.2	168.46	0.1942
8	1348	63.670	1587	135.89	0.3173
15	1351.0	64.41	1591.3	134.68	0.2589
2	1348.9	59.43	1591.8	149.79	0.1989
5	1352.7	103.95	1592.6	172.07	0.4413
10	1352.2	64.56	1594.0	99.98	0.3605
20	1349.7	63.704	1592.2	119.1	0.3705
40	1350.1	67.65	1589.0	134.61	0.0020
50	1349.5	65.81	1588.6	140.89	0.2654

Table D4: The D and G band for CVD synthesized nanocomposites with varying low MWCNTs wt.%

wt.%	D band		G band		$\frac{I_D}{I_G}$
	Position	Width	Position	Width	
2	1343	112.05	1597.0	66.26	0.7169
5	1334.1	156.09	1593.3	73.40	1.6718
12	1322.6	148.48	1602.2	53.73	1.8199
4	1372.3	8.59	1796.2	226.93	0.0035
2	1344.4	98.97	1582.1	184.52	1.2769
5	1345	73.891	1596	67.474	0.3009
10	1324.4	136.05	1599.8	66.997	1.1365
15	1335.8	110.02	1599.8	66.451	0.3114
20	1348.1	77.828	1600.9	57.418	0.1866
0.5	1326.7	95.44	1603.9	53.579	0.8577
50	1349.5	65.81	1588.6	140.89	0.2654

Appendix E
Diffuse reflectance

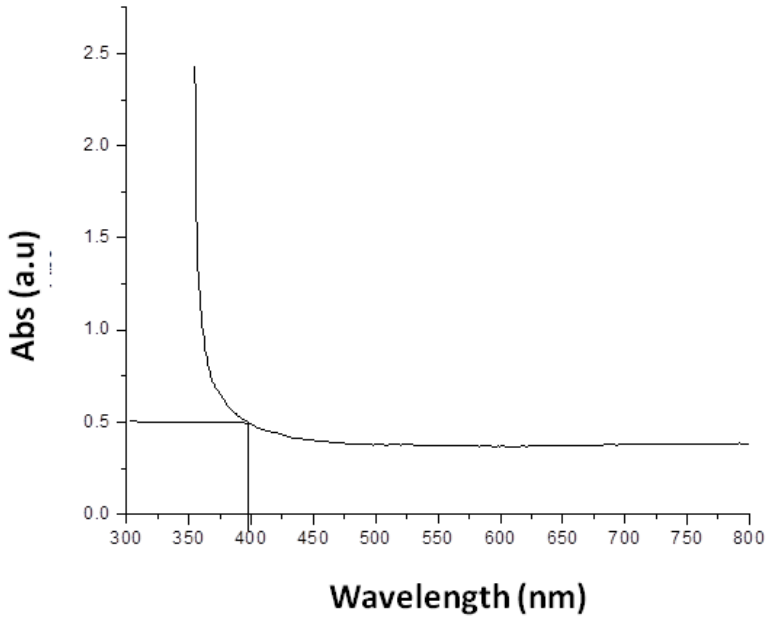

Figure E1: Representative diffuse reflectance for determination of cut off wavelength

Appendix F
Current density-voltage curves

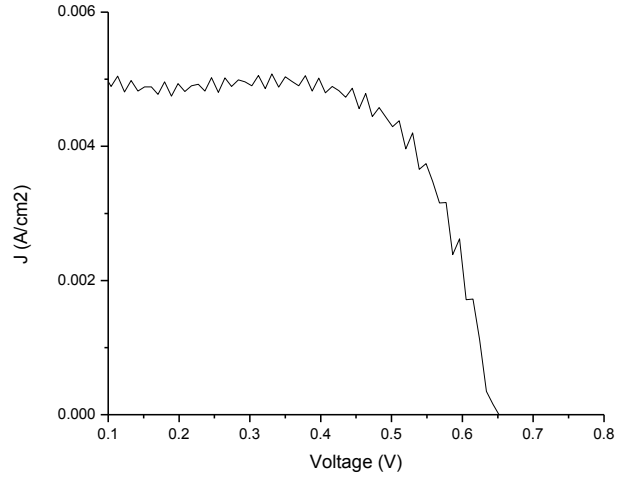

Figure F1: The representative J-V curve for CVD nanocomposite at 10 wt.% of MWCNTs

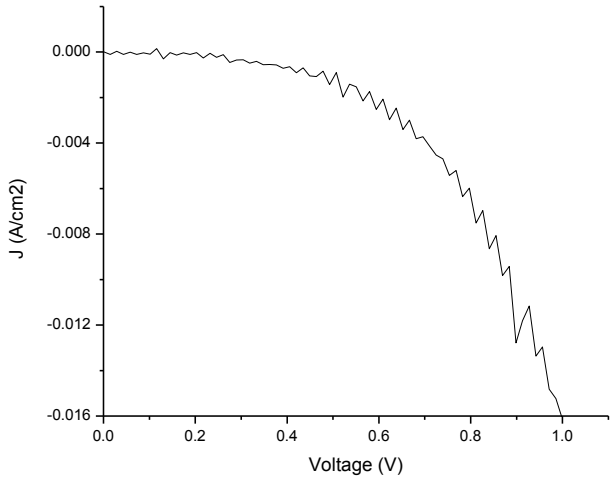

Figure F2: The representative J-V curve for sol-gel nanocomposite at 10 wt.% of MWCNTs

Appendix G
TEM images

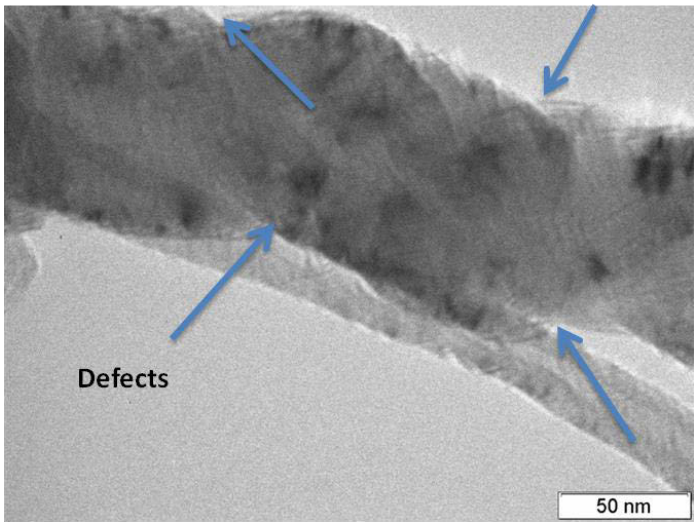

Figure G1: Representative images synthesised by CVD method at 20 wt.% of MWCNTs showing defects

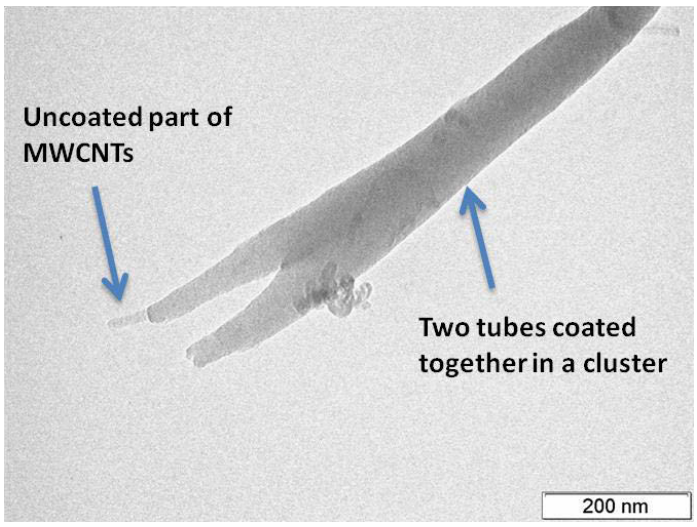

Figure G2: Representative images synthesised by CVD method at 20 wt.% of MWCNTs showing two MWCNTs coated together to form a cluster

Appendix H
FTIR spectra

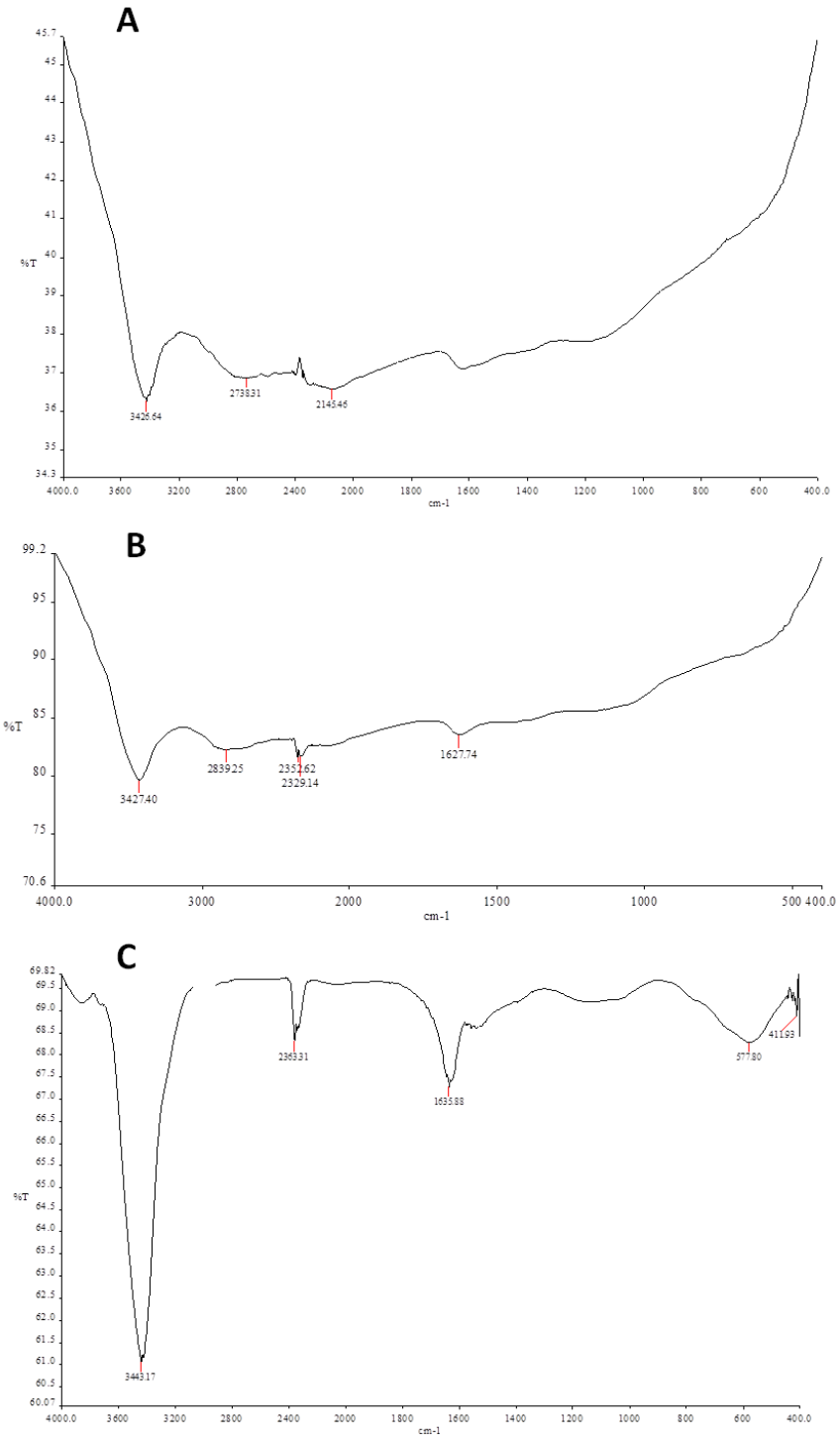

Figure H1: Comparison of functional groups for (**A**) pristine MWCNTs, (**B**) acid-treated MWCNTs and (**C**) representative nanocomposites at high wt.% of MWCNT